

**INVESTIGATING MICROCHANNEL REACTORS FOR FISCHER-TROPSCH
SYNTHESIS**

by

Fabiana Arias Pinto

BS Chemical Engineering, Universidad Simon Bolivar, 2013

Submitted to the Graduate Faculty of
Swanson School of Engineering in partial fulfillment
of the requirements for the degree of
Master of Science in Petroleum Engineering

University of Pittsburgh

2016

UNIVERSITY OF PITTSBURGH
SWANSON SCHOOL OF ENGINEERING

This thesis was presented

by

Fabiana Arias Pinto

It was defended on

August 2, 2016

and approved by

George E. Klinzing, Ph.D., Professor, Department of Chemical and Petroleum Engineering

Robert M. Enick, Ph.D., Professor, Department of Chemical and Petroleum Engineering

Thesis Advisor: Badie I. Morsi, Ph.D., Professor, Department of Chemical and Petroleum
Engineering

Copyright © by Fabiana Arias Pinto

2016

INVESTIGATING MICROCHANNEL REACTORS FOR FISCHER-TROPSCH SYNTHESIS

Fabiana Arias Pinto, M.S

University of Pittsburgh, 2016

Microchannel reactors (MCRs) exemplify significant miniaturization of the physical dimensions and process intensification when compared with conventional industrial reactors, allowing for linear scaleup, flexible manipulations, and substantial capital cost reductions. MCRs have promising applications in Gas-to-Liquid (GTL) technologies, such as the Fischer-Tropsch (F-T) synthesis, particularly for monetizing small onshore and offshore gas fields, which is economically unfeasible with other conventional industrial F-T technologies. Even though MCRs were proposed for commercial implementations and demonstration plans have already been built, adequate literature publications on the use of MCRs in F-T synthesis is scanty and to the best of our knowledge many details concerning the hydrodynamics, mass transfer, heat transfer, and reactor performance are not available.

The overall objective of this study is to investigate the performance and the flow distribution of a MCR, using one-dimensional (1-D) and Computational Fluid Dynamics (CFD) models. A MCR consisting of 50 channels, each packed with 100-micron cobalt catalyst, operating under the low temperature F-T synthesis (500 K and 25 bar) was used to study the reactor performance. The inlet flow distribution was investigated using another CFD model with air at

298 K and 1.01325 bar. A 50-channel MCR was used in this investigation. The modeling results led to the following conclusions:

1. The 1-D model systematically predicted steeper hydrocarbon flow rate profiles when compared with those of the CFD model, however, both models converge to the same values at the channel outlet.
2. For one channel of the MCR, both the 1-D and CFD models indicated that increasing the H₂/CO ratio in the feed increased CO conversion, C₅⁺ yield, pressure drop, F-T reaction rate, and the heat transfer requirements. Increasing the inlet syngas velocity decreased CO conversion and increased the pressure drop. Also, increasing temperature, increased the F-T reaction rate, CO conversion and the C₅⁺ yield, and decreased the pressure drop. Furthermore, under the conditions investigated, the F-T process in the MCR used was kinetically-controlled.
3. The CFD model used to investigate the flow distribution in the MCR showed that using a flow distributor resulted in a homogenous flow distribution and eliminated the strong gas recirculation.

TABLE OF CONTENTS

ACKNOWLEDGMENT.....	XIII
NOMENCLATURE	XIV
1.0 INTRODUCTION	1
1.1 PROCESS INTENSIFICATION AND MINIATURIZATION.....	8
1.2 APPLICATION OF MCRS IN FISCHER-TROPSCH SYNTHESIS AND RELATED PROCESSES.....	11
2.0 OBJECTIVE	16
3.0 RESEARCH APPROACH	17
3.1 CONFIGURATION OF THE MCR INVESTIGATED	17
3.2 PRESSURE DROP PREDICTION.....	20
3.3 MASS TRANSFER IN MCR.....	23
3.4 DEVELOPMENT OF A ONE-DIMENSIONAL MODEL FOR THE MCR.....	29
3.5 DEVELOPMENT OF A CFD MODEL FOR THE MCR.....	33
3.5.1 Inlet geometry mesh of the MCR	33
3.5.2 Conservation Equations for Multiphase Flow	35
3.5.2.1 Conservation of Mass.....	36
3.5.2.2 Conservation of Momentum	36
3.5.3 Fischer-Tropsch Reaction Kinetics.....	38
3.5.4 Thermo-physical Properties of the F-T Reactants and Products	39

3.5.5	Pressure Drop Calculations	40
3.5.6	Heat Transfer Calculations	41
3.5.7	Mass Transfer Calculations	42
3.5.8	Boundary Conditions, Solution Method and Meshing	45
4.0	RESULTS AND DISCUSSION	47
4.1	RESULTS OF THE ONE-DIMENSIONAL MCR MODEL	47
4.2	RESULTS OF THE CFD MCR MODEL SIMULATIONS	49
4.2.1	Velocity Profile.....	49
4.2.2	Pressure Drop	51
4.2.3	Conversion, Selectivity and Yield.....	53
4.2.4	Products Distribution.....	55
4.2.5	Heat Transfer Calculations	56
4.2.6	Mass Transfer Calculations	57
4.3	EFFECTS OF OPERATING CONDITIONS	59
4.3.1	Effect of H ₂ /CO Feed Ratio on the MCR Performance.....	60
4.3.2	Effect of pressure on the MCR performance.....	64
4.3.3	Effect of temperature on the MCR performance	68
4.3.4	Effect of inlet gas velocity on reactor performance	71
4.4	FLOW DISTRIBUTION SIMULATION	75
4.5	COMPARISON BETWEEN THE 1-D AND CFD MCR MODELS	80
5.0	CONCLUSIONS.....	84
	APPENDIX.....	86
	BIBLIOGRAPHY.....	89

LIST OF TABLES

Table 1-1: F-T plants: catalysts and reactor technologies [8, 9].....	4
Table 1-2: Experimental investigations in F-T synthesis and other related processes using MCRs	12
Table 1-3: Experimental investigations in F-T synthesis and other related processes using MCRs (continued).....	13
Table 1-4: Experimental investigations in F-T synthesis and other related processes using MCRs (continued).....	14
Table 3-1: Microchannel Operating Conditions	18
Table 3-2: Reactions and products list.....	18
Table 3-3: Pressure drop models.....	20
Table 3-4: Data for Pressure Drop Models evaluation	21
Table 3-5: Catalysts used in the 1-D model	30
Table 3-6: Reactants and products properties at T = 500 K (226.85 °C) and 25 bar [81, 82]	39
Table 3-7: Temperature dependent ABC Parameter for properties of n-Paraffins [84]	40
Table 4-1: Molar flows at the channel outlet	54
Table 4-2: CO molar flow requirement and individual heat release per reaction.....	56
Table 4-3: Simulation parameters considered for different operating conditions	60
Table 4-4: Effect of varying H ₂ /CO ratio on MCR performance	63
Table 4-5: Effect of pressure on MCR performance	67
Table 4-6: Effect of temperature on MCR performance.....	71

Table 4-7: Effect of superficial gas velocity on the MCR performance.....	74
Table A-5-1: Other Experimental investigations using MCRs.....	86
Table A-5-2: Other Experimental investigations using MCRs (continued)	87
Table A 5-3: Other Experimental investigations using MCRs (continued).....	88

LIST OF FIGURES

Figure 1-1: Overview of GTL and CTL processes [2]	2
Figure 1-2: Fischer Tropsch Industrial Technologies.....	5
Figure 1-3: General Schematic of an MCR unit [23]	9
Figure 3-1: Dimensions of the MCR unit and the packed channel investigated in this study	17
Figure 3-2: Double chain probability growth model	19
Figure 3-3: Pressure drop prediction using different models.....	22
Figure 3-4: Schematic of a gas-liquid-solid interactions in the MCR	23
Figure 3-5: Henry's law constants for H ₂ and CO	24
Figure 3-6: CO conversions with and without mass transfer.....	28
Figure 3-7: MCR geometry used in the CFD model.....	34
Figure 3-8: Reactors housing with flow distributor	35
Figure 4-1: Effects of catalyst shape and porosity on the CO Conversion.....	48
Figure 4-2: Effects of catalyst shape and porosity on the pressure drop	49
Figure 4-3: Mean velocity along channels length.....	50
Figure 4-4: Velocity profiles along the channel length	51
Figure 4-5: Pressure drop contours along the channel length.....	52
Figure 4-6: Change of CO molar flow with the channel length	53
Figure 4-7: Change of the hydrocarbons molar flow rates with the channel length.....	55

Figure 4-8: Change of the pseudo-first order reaction rate with the channel length	58
Figure 4-9: Change of the pseudo-first order reaction rate coefficient with the channel length ..	58
Figure 4-10: Change of H ₂ concentration with the channel length.....	59
Figure 4-11: Effect of H ₂ /CO ratio on CO conversion	61
Figure 4-12: Effect of H ₂ /CO ratio on C ₅₊ selectivity	61
Figure 4-13: Effect of H ₂ /CO ratio on C ₅₊ Yield.....	62
Figure 4-14: Effect of H ₂ /CO ratio on the (a) pressure drop and (b) maximum kinetic rate.....	63
Figure 4-15: Effect of pressure on CO conversion	65
Figure 4-16: Effect of pressure on C ₅₊ selectivity	65
Figure 4-17: Effect of pressure on C ₅₊ yield.....	66
Figure 4-18: Effect of pressure on (a) the pressure drop and (b) the maximum kinetic rate.....	67
Figure 4-19: Effect of temperature on CO conversion	68
Figure 4-20: Effect of temperature on C ₅₊ selectivity	69
Figure 4-21: Effect of temperature on C ₅₊ yield.....	69
Figure 4-22: Effect of temperature on (a) the pressure drop and (b) the maximum kinetic rate ..	70
Figure 4-23: Effect of superficial inlet gas velocity on CO conversion	72
Figure 4-24: Effect of superficial inlet gas velocity on C ₅₊ selectivity.....	72
Figure 4-25: Effect of superficial inlet gas velocity on C ₅₊ yield	73
Figure 4-26: Effect of superficial inlet gas velocity on (a) the pressure drop and (b) the maximum kinetic rate.....	74
Figure 4-27: Velocity contour and vector profiles of the flow distribution with (V-inlet = 0.1 m/s)	76
Figure 4-28: Velocity contour and vector profiles of the flow distribution with (V-inlet = 0.5 m/s)	77
Figure 4-29: Velocity contours at the micro channel's inlet.....	78

Figure 4-30: Velocity contours with flow distributor ($V_{\text{inlet}}=0.5$ m/s).....	79
Figure 4-31: Velocity contours at the MCR inlet	80
Figure 4-32: Comparison between the flow rates of H_2 , CO and H_2O using the 1-D and CFD MCR models	81
Figure 4-33: Comparison between the C_1 products flow rates using the 1-D and CFD MCR models	82
Figure 4-34: Comparison between the hydrocarbon products flow rates between 1-D and CFD MCR models	82
Figure 4-35: Comparison between the pressure drop using the 1-D and CFD MCR models	83

ACKNOWLEDGMENT

I would like to present my special thanks to my academic and research advisor Dr. Badie Morsi for giving me the opportunity to join RAPEL research group and for encouraging me during the course of my master studies. For all your generous input and the support provided throughout the development of this research, my sincere thanks.

I would also like to express my gratitude to Mr. Omar Basha who did not hesitate to help me any time and who has been a great collaborator in this project. To my lab partners Mr. Yongtai Li, Mr. Gustavo Santos and Mr. Pedro Rosa, thank you for sharing your research experiences with me during this time.

To Gianfranco Rodriguez, for all your love and support during this time, thank you for being here with me every step of the way.

To my family, my main motivation everything that I do and everything that I accomplish in life, no matter the physical distance between us, I deeply appreciate the unlimited support and unconditional love that you have always had for me. In a special way, I am grateful for my parents, for being my role models and for believing in me in the way they do.

Above all, thanks be to God for all your blessings, for giving me the strength and courage to pursue and achieve my goals.

NOMENCLATURE

a	Interfacial area, m^{-1}
A	Channel cross-sectional area, m^2
A_s	Heat transfer area, m^2
PF	Average packing fraction, -
C_2	Pressure drops inertial coefficient, $\text{Pa s}^2 \text{kg}^{-1}$
Cd	Drag coefficient, -
C_i	Molar concentration of the species “i”, kmol m^{-3}
C_p	Specific heat, $\text{J kg}^{-1} \text{K}^{-1}$
d	Diameter, m
$D_{L,i}$	Diffusion coefficient, m s^{-2}
E_{FT}	Activation energy J mol^{-1}
f	Drag function, -
F_i	Molar flow of the species “i”, mol s^{-1} or mmol s^{-1}
F_T	Total molar flow of the species, mol s^{-1} or mmol s^{-1}
g	gravity, m s^{-2}
h_{fg}	Enthalpy of vaporization, kJ kg^{-1}
ΔH	Enthalpy change, J mol^{-1} or kJ mol^{-1}
k	mass transfer coefficient, m s^{-1}

k_{FT}	Fischer Tropsch reaction rate coefficient $\text{kmol kg}_{\text{cat}}^{-1}\text{s}^{-1}\text{Pa}^{-1}$
k_{WGS}	Water gas shift reaction rate coefficient $\text{mol g}_{\text{cat}}^{-1}\text{bar}^{-1}$
K	Permeability, m^2
K_{pq}	Interphase momentum exchange coefficient, $\text{kg m}^{-3}\text{s}^{-1}$
L	Length, m
\dot{m}_{pq}	Mass transfer rate per unit volume from the “p” to the “q” phase, $\text{kg s}^{-1} \text{m}^{-3}$
\dot{m}_w	Water flowrate, ml min^{-1}
M_f	Mass fraction, -
M_{wt}	Molecular weight, kg. kmol^{-1}
p_i	Partial pressure of the species “i”, kPa
P	Pressure, bar or Pa
q	Heat released per reaction, J s^{-1}
Q	Total heat released, J s^{-1}
r_{FT}	Reaction rate, $\text{mol m}^{-3}\text{s}^{-1}$ or $\text{kmol m}^{-3}\text{s}^{-1}$
r_i	Rate of consumption/formation, $\text{mol s}^{-1}\text{m}^{-3}$
R	Gas constant, $\text{J mol}^{-1}\text{K}^{-1}$
Re	Reynolds number, -
R_{pq}	Interaction forces between phases “p” and “q”, $\text{kg m}^{-2}\text{s}^{-2}$
S	User defined source term
Sel	Selectivity of products, %
ΔT_{Lm}	Logarithmic temperature difference, -
T	Temperature, K
u	Velocity, m s^{-1}

U	Heat transfer coefficient, $\text{W m}^{-2} \text{K}^{-1}$
V_L	Liquid molar volume, $\text{cm}^3 \text{gmol}^{-1}$
V_S	Superficial velocity, m s^{-1}
V_{inlet}	Velocity at the inlet of the reactor, m s^{-1}
X_{cat}	catalyst fraction, $\text{kg}_{\text{cat}} \text{m}^{-3}_{\text{reactor}}$
X_{CO}	CO Molar conversion, %
Z	Compressibility factor, -

Greek Symbols

α	Volume fraction of the phase, -
$\alpha_{1,2}$	Chain growth probability according to the double ASF model
α_{ASF}	Chain growth probability according to the ASF distribution
β	Reaction effectiveness factor, -
γ	Reaction Yield, %
δ_L	Liquid film thickness, m
ϵ	Porosity, -
ϵ_L	Liquid holdup, -
μ	Dynamic viscosity, Pa s^{-1}
ρ	Density, kg m^{-3}
σ	Thermal conductivity, $\text{W m}^{-1}\text{K}^{-1}$
σ_p	Particulate relaxation time, s
τ	Shear stress, Pa
ν_i	Stoichiometric coefficient of the species “i”, -

Subscripts

bulk	Referred to the apparent density of the bed
c	Critical
cat	Catalyst
C ₅₊	Carbon products with carbon number ≥ 5
B	Packed bed
GL	Gas-liquid
h	Hydraulic
LS	Liquid-solid
p	Particle
R _{TOTAL}	Of all the reactions
R _i	Of an individual reaction

Acronyms

ASF	Anderson-Schulz-Flory
ATR	Auto thermal reforming
BCC	Based centered cubic
CFD	Computational fluid dynamics
CFBR	Circulating fluidized bed reactor
CTL	Carbon to liquid
EOS	Equation of state
FBR	Fluidized bed reactor
FCC	Face centered cubic

FFBR	Fluidized fixed bed reactor
F-T	Fischer Tropsch
GTL	Gas to liquids
H	Hexagonal
HTFT	High temperature Fischer Tropsch
ICC	Interconnected centered cubic
IFCC	Interconnected face centered cubic
LTFT	Low temperature Fischer Tropsch
MCR	Micro channel reactor
P	Primitive
POX	Partial oxidation
R	Rectangular
SBCR	Slurry bubble column reactor
UDF	User defined function
WGS	Water Gas Shift

1.0 INTRODUCTION

Fischer Tropsch (F-T) synthesis process provides a pathway for converting carbonaceous sources, such as biomass, coal and natural gas, into liquid fuels and high value chemicals. The process was originally developed by Franz Fischer and Hans Tropsch in the 1920's in an effort to produce liquid fuels, based on the 1902 discovery by Sabatier and Sanders [1], that methane can be produced from H_2/CO mixtures over a nickel catalyst. Over the past century, numerous investigators have contributed to the development of this process by studying the reaction kinetics and reactor design, with the aim of developing cleaner process for producing liquid fuels.

The overall F-T process involves three main steps: syngas generation, F-T catalytic reactions and products upgrading, as shown in Figure 1-1. Syngas generation involves converting the carbon containing feedstocks into syngas, which is a mixture of H_2 and CO , via reactions with steam and O_2 or air. Natural gas is converted to syngas in a reformer, using auto-thermal reforming (ATR), partial oxidation (POX) or steam-methane reforming. Solid feedstocks, such as biomass, coal and petroleum residue, on the other hand, are converted in gasifiers, of which numerous types have been in industrial use.

In F-T synthesis, the syngas ($CO + H_2$) react in the presence of a catalyst, conventionally iron catalysts or cobalt supported catalyst, to produce synthetic hydrocarbon products, primarily linear alkanes and alkenes. The main reactions occurring during the F-T synthesis are the formation of paraffins and olefins, in addition to the water-gas-shift (WGS) reaction. Secondary reactions

such as, the formation of oxygenates and the conversion of CO via the Boudouard reaction may also occur [3]. The general form of these reactions is shown in Equations (1-1) to (1-5).

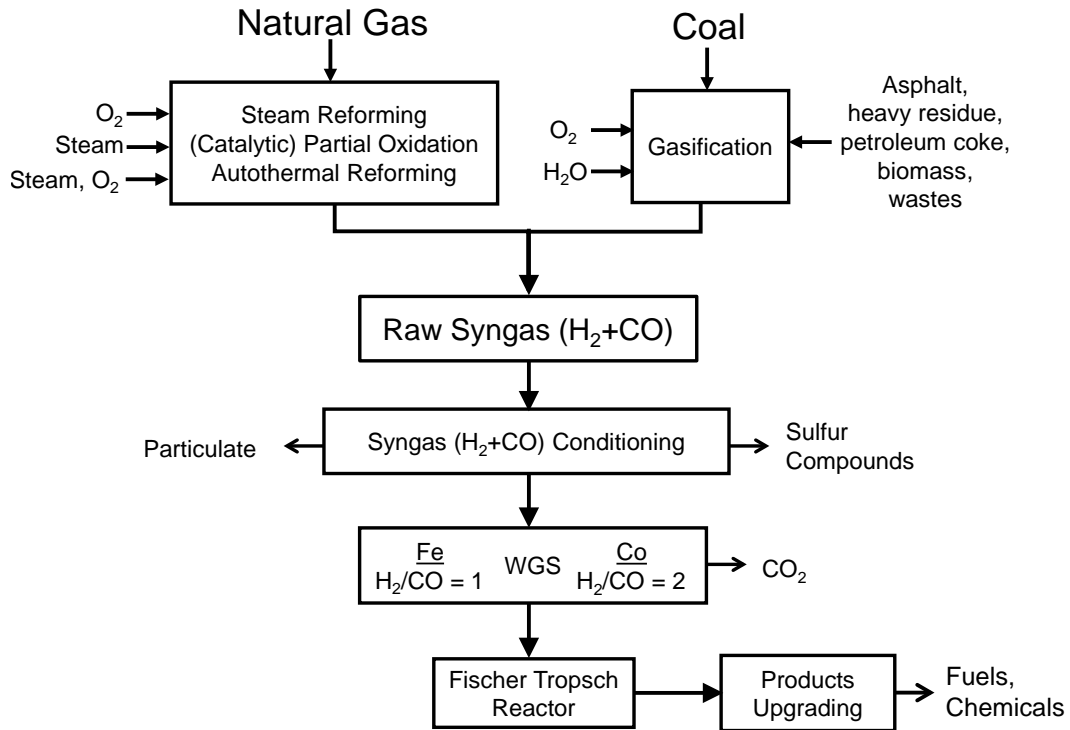
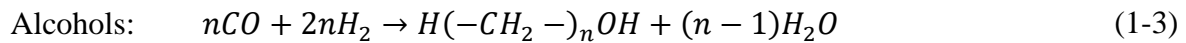
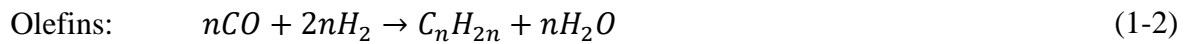
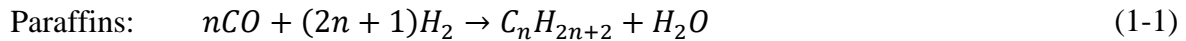


Figure 1-1: Overview of GTL and CTL processes [2]



Although many metals have been identified to catalyze F-T reactions, the only two main catalysts currently used in industrial F-T plants are iron and Cobalt-based catalysts. Iron catalysts are less expensive, present high selectivity to olefins, and are preferred when using CO-rich syngas since they can elevate the H₂ content via the WGS reaction. On the other hand, cobalt-based catalysts are preferred when using H₂-rich syngas, have low selectivity to WGS reactions (low carbon dioxide formation), present higher selectivity to paraffin, but high undesired methane formation when compared with iron catalyst [4]. Additionally, Ruthenium and Nickel catalysts have been used in lab-scale F-T investigations, and were shown to have high activities at low temperatures. However, their high selectivity to methane at high temperature conditions, in addition to their significantly higher costs compared to iron and cobalt-based catalysts, make them unsuitable for industrial use [5].

During cobalt catalyzed F-T reaction, the oxygen from CO dissociation is converted to H₂O, as shown in Equations (1-1) to (1-3). Whereas, iron catalyst has a high affinity for the WGS reaction as shown in Equation (1-5), which promotes H₂ and CO₂ formation. Thus, the extent of the WGS reaction has to be closely considered as it affects the H₂/CO ratio in the F-T process.

F-T process temperature and pressure may vary from 200 to 350 °C and from 15- to 60 bar, respectively, depending on the feedstock and desired products. Low-Temperature F-T (LTFT) operates between 180-260 °C, and typically produces wax consisting of mostly long chain hydrocarbons, whereas High-Temperature F-T (HTFT) operates between 320-360 °C, and the products are mainly short chain hydrocarbons and gaseous compounds [5, 6]. HTFT tends to move the selectivity towards products with low carbon numbers and high hydrogen content, while LTFT favors the formation of longer linear alkanes [5, 6]. The syncrude produced from LTFT can be upgraded to naphtha and middle distillate by a hydroprocessing step and a fractionation step, while

the HTFT syncrude requires more complex refining capacities [7]. The HTFT reactors include fixed fluidized-bed reactors (FFBRs) and circulating fluidized-bed reactors (CFBRs), whereas multi-tubular fixed-bed reactors (FBRs) and slurry bubble column reactors (SBCRs) are used for the LTFT process. A schematic of the different F-T reactors is shown in Figure 1-2. Table 1-1 summarizes F-T plants and reactor technologies.

Table 1-1: F-T plants: catalysts and reactor technologies [8, 9]

F-T Plant	Date of Operation	Reactor Technology	Catalysts
German CTL	1935-1962	LTFT FB	Co/ThO ₂ /kieselguhr (100:18:100) before 1938 Co/ThO ₂ /MgO/kieselguhr (100:5:8:200) after 1938
Hydrocol GTL	1951-1957	HTFT FFB	Fused Fe ₃ O ₄ /Al ₂ O ₃ /K ₂ O (97:2.5:0.5) Later replaced by natural magnetite with 0.5% K ₂ O
Sasol I CTL/GTL	1955-present	HTFT CFB LTFT FB LTFT SBCR	Magnetite with 0.5% K ₂ O Precipitated Fe/SiO ₂ /K ₂ O/Cu (100:25:5:5) Precipitated Fe/SiO ₂ /K ₂ O/Cu (100:25:5:5)
Sasol Synfuels CTL	1980-present	HTFT FFB	Fused Fe (similar to Sasol I HTFT CFB catalyst)
PetroSA GTL	1992-present	HTFT CFB LTFT SBCR	Fused Fe (same as Sasol Synfuels) Co based catalyst
Shell Bintulu	1993-present	LTFT FB	Co/Zr/SiO ₂
Sasol Oryx GTL	2007-present	LTFT SBCR	Co/Pt/Al ₂ O ₃
Pearl GTL	2011-present	LTFT FB	Co/Zr/SiO ₂

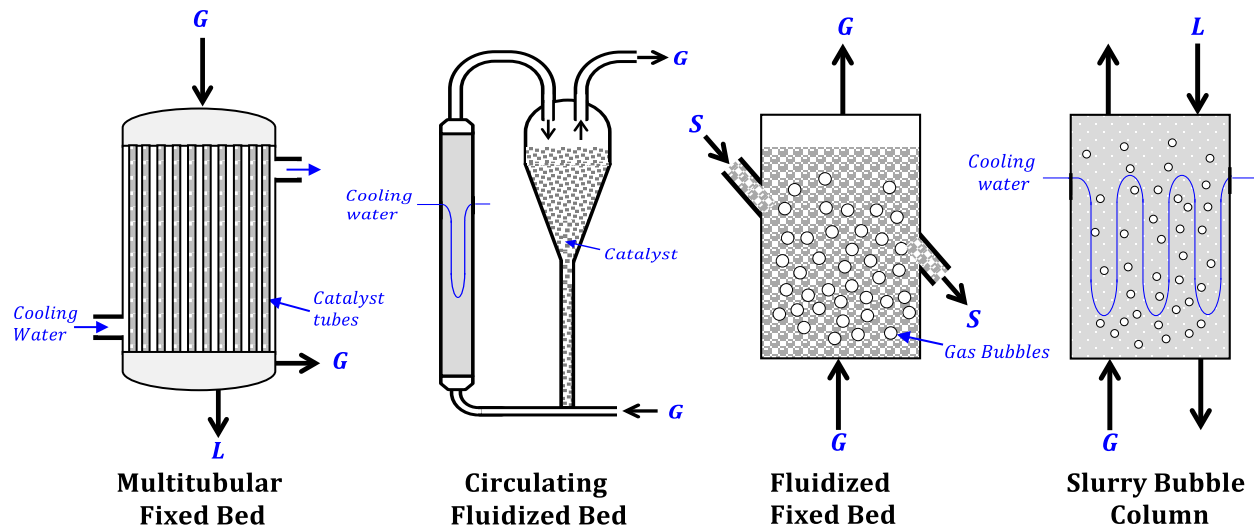


Figure 1-2: Fischer Tropsch Industrial Technologies

In multi-tubular FBRs, the syngas flows through small diameter tubes packed with catalyst at small voidage, resulting in a high pressure drop and an increased operating cost. These reactors have comparatively complex heat transfer characteristics and their maximum production capacity is limited by the amount of heat which can be removed. Hot spots would ultimately result in carbon deposits on the catalyst surfaces and serious plugging of the reactor tubes. These types of reactors, however, have been used to carry out LTFT by Germany during WWII and Sasol since 1950's using an iron catalyst, as well as by Shell GTL at the Bintulu (Malaysia) and more recently at the Pearl GTL (Qatar), using a Co-based catalyst [2, 8–12].

Another technology that was commercially applied for syncrude production was the Circulating Fluidized Bed introduced by Kellogg in 1955 and Sasol in 1980. The Sasol Circulating Fluidized Bed technology (Sasol Synthol reactor) had a 2,000-6,500 bbl/d plant capacity, and it was then substituted by an advanced Synthol reactor (1993) with an increased capacity (11,000-20,000 bbl/d). Sasol's Advanced Synthol reactor led to the decrease of the reactor size per required

capacity, catalyst consumption and maintenance requirements [13]. Slurry Bubble Column Reactors (SBCRs), on the other hand, allow for high mixing levels, reaction rates, and volumetric conversion rates as well as a more efficient heat removal. Compared with Multi-Tubular FBRs, SBCRs have lower pressure drop, offers easier catalyst removal operations and better heat control [6, 13, 14]. However, the high mechanical shear on the catalyst resulting in particles attrition and the lack of a reliable system for the fine particles separation from the liquid products, have delayed the commercial deployment of SBCRs until the 1990's.

Recently, novel reactor technologies have received increasing interest for F-T applications, such as honeycomb monolith reactors, micro-structured reactors and membrane reactors [15]. These reactors offer the advantage of process intensification, primarily due to their ability to utilize smaller carbonaceous sources and be deployed in remote and harsh locations, thus enabling monetizing a previously inaccessible energy market.

In monolith reactors, active catalyst layers are deposited on the channels walls allowing for low pressure drop and enhanced mass transfer. This design approach was studied by Bradford et al. [16] for a P/Pt-Co/ γ -Al₂O₃ catalyst in a 0.075 m³ tubular reactor with channels of 1.5 mm \times 1.5 mm \times 1.52 m . Under those circumstances, the monolith reactor was superior to a similar fixed-bed reactor in terms of productivity per catalyst unit mass. However, it was not superior in reactor productivity per unit volume when compared with multi-tubular FBRs and SBCRs. Similarly, Kapteijn et al. [17] tested a square monolith reactor using a cobalt-rhenium catalyst and the production of α -olefins by LTFT was successfully achieved, however, mass transfer limitations due to catalyst layer thickness were found.

On the other hand, catalytic membrane reactors offer the possibility of distribution of the feed reactants across the membrane, removal of the water production inside the reactor and the use

of encapsulated catalysts. Several cobalt and iron catalyst with various membrane supports have been tested for F-T synthesis in membrane reactors [18]. Rohde et al. [18] discussed key points in the membrane reactor design, namely, the possible variation of the H_2/CO ratio in the feed distribution across the membrane and its negative consequences in reactors selectivity, enhancement of catalyst active life, and the improvement of the F-T reaction rate by in-situ water removal. Also, the existence of a defined and controllable reaction zone (membrane) and benefits of the forced contact between reactants and catalyst particles when flowing through the membrane.

1.1 PROCESS INTENSIFICATION AND MINIATURIZATION

Process intensification, which refers to the technologies and strategies that enable significant reduction of the physical dimensions of a conventional unit operation, has been receiving considerable attention over the past two decades. The motivation of this approach stems from the fact that the main components of a given plant, such as reactors, heat exchangers, separators, etc., only contribute to about 20% of the overall capital cost, whereas, 80% of the cost is incurred by installation and commissioning, which includes pipe-work, structural support, civil engineering, etc. [7]. This means that major reductions in the equipment size, coupled preferably with a degree of telescoping of equipment function, such as reactor/heat exchanger unit, or combined distillation/condenser/re-boiler, could result in significant cost savings by eliminating the support structure, expensive foundations and long pipe runs.

Actually, process intensification has the potential to deliver major benefits to the petrochemical and chemical process industry by accelerating the response to market changes, simplifying scale-up and providing the basis for rapid development and deployment of new products [19]. Microchannel reactor (MCR) technology is an example of process intensification in chemical engineering as it (1) enhances the heat and mass transfer processes; (2) allows precise adjustment of the initial and boundary conditions as well as the residence or contact time for continuous chemical reactions; (3) allows linear scaleup; and (4) represents inherently safe plant concepts.

A general layout of a MCR is schematically depicted in Figure 1-3 [20, 21]. This type of reactor is characterized by a parallel array of vertical microchannels and cross-flow horizontal

cooling microchannels. The typical dimensions of the channels are between 0.1 and 5.0 mm. Such arrangement is expected to significantly enhance the processes by reducing the heat and mass transfer resistances [20, 21] and reducing the overall system volumes by 10 folds or more [22] .

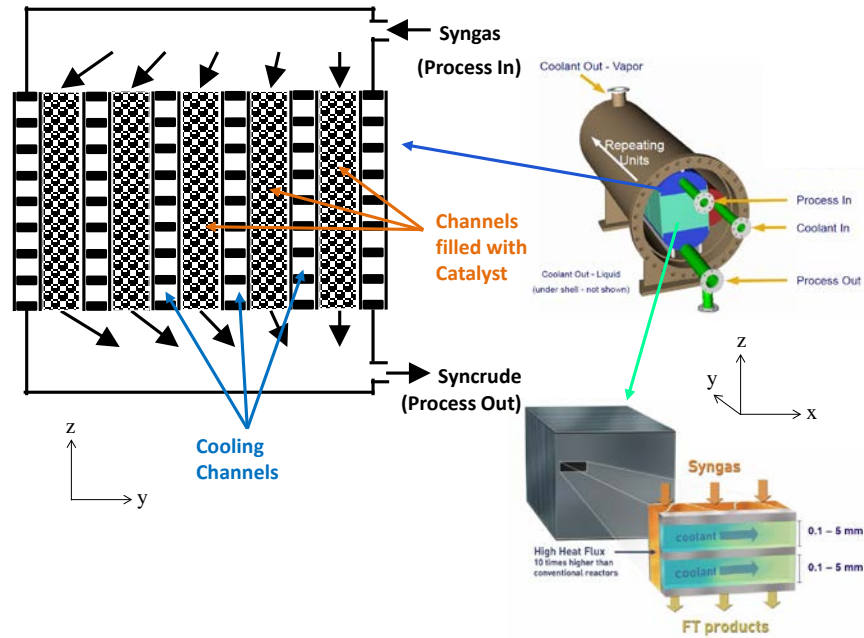


Figure 1-3: General Schematic of an MCR unit [23]

In general, the transport fluxes of mass, energy and momentum are dependent, not only on the mass diffusivity, thermal conductivity and viscosity, but also on the corresponding concentration, temperature, and velocity gradients. The decrease in the physical dimensions (miniaturization) of a unit operation leads to the enhancement of mixing and heat exchange, which increase the mass and heat transfer rates as well as the viscous losses [24, 25]. Moreover, with decreasing the physical dimensions, the amount of material in a system is reduced, and the surface

area per unit volume ratio could increase. For industrial- and laboratory-scale reactors, this ratio is generally below $100 \text{ m}^2/\text{m}^3$ and $1,000 \text{ m}^2/\text{m}^3$, respectively, however, for MCRs the ratio might reach $50,000 \text{ m}^2/\text{m}^3$ [26].

From a commercial perspective, a major advantage of MCRs is the ease of scale-up through modular assembly. Multiple units can be assembled in parallel or in series [20], maintaining a continuous flow operation. Moreover, MCR technology allows for the potential utilization of remote gas fields, especially in offshore locations, which were previously unfeasible to monetize. As such, this overcomes a major challenge facing GTL applications using the F-T synthesis, which lies in the fact that at least 50,000 barrel per day (bpd) production F-T plant is required in order to lower the capital cost per barrel of daily capacity to an acceptable level [7]. However, such large F-T plants would require about 50 MMSCF/d of the feed gas, or 5.4 trillion cubic feet of gas over a thirty year period, which limits their potential installation to only about 2% of the known gas fields outside of North America [27]. It should be noted that current commercial F-T plants produce between 34,000-140,000 bbl/d of liquid fuels, and require immense amount of feedstock. Furthermore, many other applications, such as emulsion processing, biofuels, hydro-processing and biogas conversion could also greatly benefit from the compact and modular conversion technology [22].

The miniaturized dimensions of these devices create a high surface to volume ratio allowing enhanced heat and mass transfer capacities and high productivity per unit volume. For the F-T synthesis, these features may offer a reduction in the methane formation and improving the products distribution. It also offers the possibility to have decentralized plants that may benefit offshore natural gas processing, biomass to liquids (BTL) technologies and waste to liquid technologies.

1.2 APPLICATION OF MCRs IN FISCHER-TROPSCH SYNTHESIS AND RELATED PROCESSES

MCRs have been investigated to carry out F-T synthesis [28–33] and other related processes, such as methanol steam reforming and methane steam reforming [34, 35]; selective oxidation processes and Catalytic partial oxidations [36–38]; and WGS reactions [39, 40] as shown in Table 1-2.

Other applications of MCRs, including partial oxidation of toluene [41]; synthesis of peptides [42]; hydrocarbons combustion [43, 44]; biomass pyrolysis [45]; conversion of cyclohexene [32, 46]; condensation of organic compounds [47, 48]; methanation reactions [49]; synthesis of formaldehyde [50]; nitration reactions [51, 52]; nucleophilic reactions [53]; photocatalytic processes [54], etc., can be found in the Appendix.

Table 1-2: Experimental investigations in F-T synthesis and other related processes using MCRs

Reference	Process Investigated	Reactor Dimensions
Aartun, et al., 2005 [37]	The partial oxidation of methane and the oxidative steam reforming of propane for the production of hydrogen or syngas were studied. The influence of the temperature distribution and the change in residence time were analyzed regarding their effect in conversion and products selectivity.	3 Fecralloy metallic reactors were used. Reactors dimension (H × W × L): 5.5 mm x 5.6 mm x 10 mm. The number of channels was 676 for two configurations and 572 for the third. Rectangular channels of 120 × 130 and 100 × 120 μm. Porosity varied from 0.22 to 0.34. Channels were impregnated with Rh in most of the cases.
Karim,et al., 2005 [35]	Methanol Steam Reforming reactions were performed in catalyst packed bed and wall coated micro reactors in order to compare the performance of both configurations.	Packed Bed Channels with ID (mm): 4.1, 1.75 and 1. Catalyst loading (mg): 100, 50 and 30. Catalyst particle diameter (μm): 100–250
Kolb et al., 2005 [39]	The water-gas-shift reaction at low temperature and high temperature conditions was tested in micro-channels using different bimetallic catalyst: Pt/CeO ₂ , Pt/Rh/CeO ₂ , Pt/Pd/CeO ₂ / and Pt/Ru (all in alumina base). The catalyst was coated to the channels surface. Catalyst performance was evaluated in order to determine the best catalyst composition for a higher CO conversion.	The reactor consisted in two micro panels attached together forming 14 reaction channels of 25 mm length, 500 μm width and 250 μm depth.
Walter et al., 2005 [36]	Three different types of reactors were evaluated using the catalytic selective oxidation of isoprene as a model reaction. The performance of a ceramic fixed bed reactor, metal micro-channel reactor and a ceramic micro-channel reactor was compared.	The metal reactor was forms by six aluminum plates of 40 mm × 40 mm × 0.5 mm each. The outer dimensions were 70 mm × 70 mm × 15 mm. Channels had an inner diameter of 280 μm and were 20 mm long. The ceramic micro-reactor had an outer dimensions of 26 mm × 70 mm × 8 mm, with 16 micro-channels of square cross section (500 μm × 500 μm).
Veser, 2005 [38]	Catalytic partial oxidation of methane to form synthetic gas was studied using two models of heat integrated micro-reactors. The configurations studied were counter current heat exchange reactor (CCHR) and reverse flow reactor (RFR). Syngas yields were measured and compared with a reactor without heat integration. Temperature profiles, reaction yields vs. inlet flow rate and catalyst deactivation times were also analyzed for both models.	The CCHR was formed by three concentric stainless steel tubes with an outer diameter of 25 mm and a length of 50 cm (Friedle & Veser, 1999). The RFR has a monolith structure with a 110 mm length.

Table 1-3: Experimental investigations in F-T synthesis and other related processes using MCRs (continued)

Reference	Process Investigated	Reactor Dimensions
Flögel et al., 2006 [42]	The synthesis of peptides was evaluated using a silicon microchannel technology. Its performance was compared with typical synthesis processes as solution phase and solid phase couplings.	Total reaction volume was 78.3 μL with a mixing zone of 9.5 μL and a Reaction loop of 68.8 μL .
Cao et al., 2009 [28]	Study of F-T synthesis inside a microchannel reactor system with intensified heat transfer capacity. The temperature profile over the catalyst bed was evaluated and compared to a conventional fixed bed FT reactor.	Packed bed Channels with packing dimension equal to 1.27 cm \times 0.0508 cm \times 1.778 cm. Catalyst surface area: 60 m^2/g and a pore volume of 0.14 cm^3/g . Particle diameter: 45 and 150 μm
Men et al., 2009 [44]	Micro-channels coated with different types of catalyst were used to study the complete combustion of propane. Pt, Pd and Rh based catalysts were used for the reactions. Reaction temperature was varied. The propane conversion was evaluated over time for the different reactions conditions.	The microchannels were formed by the union of two etched plates. The openings created by these plates measure 25 mm long, 500 μm wide and 250 μm deep.
Myrstad et al., 2009 [31]	A micro structured F-T reactor was used to study the productivity, selectivity, and pressure drop and temperature profile for F-T synthesis using a Co-Re/ Al_2O_3 catalyst bed. Results were compared to a laboratory scale fixed bed reactor operated at similar conditions.	2 cm^3 reactor with and 8 parallel catalyst sections of 400 μm of deep and 800 μm of height. d_p (μm): 53-75
Deshmukh et al., 2010 [29]	The scale up capacity of microchannel reactors for F-T synthesis was studied using single channel micro reactors and multiple channel microreactors. In total four microchannel reactors were tested. The operational capacity was compared in terms of CO conversion, selectivity to secondary products and product distribution. The operational conditions of the microreactors were varied in order to test the flexibility to pressure, temperature and feed composition change.	Dimensions are in (Depth x Width x Length) / Reactor 1: Single channel (1 mm \times 0.8 cm \times 7 cm) + packed bed of 3.8 cm long. / Reactor 2: Single channel with two gaps. 1 st gap (1 mm deep), 2 nd gap: (0.5 mm deep), width – 0.6 cm, packed bed length – 61.6 cm. / Reactor 3: Similar dimensions to reactor 2. One process channels and two cooling channels / Reactor 4: 276 process channels (1 mm \times 0.3 cm \times 19 cm) + packed bed length: 17.1 cm. Crossflow configuration with cooling channels.

Table 1-4: Experimental investigations in F-T synthesis and other related processes using MCRs (continued)

Reference	Process Investigated	Reactor Dimensions
Knochen et al., 2010 [33]	Catalyst performance, conversion and pressure drop during F-T synthesis using CoRe/Al ₂ O ₃ catalyst beds. Ergun constants for calculation of the pressure drop were determined by measurements in the absence of a reaction. A model was developed to characterize the reactor performance including mass and heat balance, pressure drops and reaction rate.	Capillary internal diameter: 1.753 mm Packed bed height: 1.0 m Packing porosity: 0.355 d_p (μm): 140-200
Knobloch et al., 2013 [30]	A micro scale fixed bed reactor with Co-Re/Al ₂ O ₃ catalyst bed was used to measure pressure drop and liquid holdup during a gas flow without reaction and during FT reactions. Ergun Pressure drop constants and liquid hold up were calculated.	Packed bed Channels particle diameter: (μm): 60-580 Bed porosity: 38.7-52.4 % Bed length: 0.1-1 m d: 1.75 mm
Piermantini and Pfeifer, 2015 [40]	The enhancement of the CO/H ₂ ratio of a biomass derived syngas was achieved through high temperature and pressure water gas shift reaction in a micro reactor. The reactor was tested with packed bed catalysts and with catalyst coated walls. A scale up model based on experimental and simulations results was presented.	Fixed-bed configuration: 2 foils (150 mm long, 25 mm wide) with 1029 channels each. Channels dimensions (800 μm wide, 400 μm long, 800 μm deep). Coated walls configuration: 14 foils (150 mm long, 25 mm wide) with 50 channels each. Channels dimensions 200 μm wide, 200 μm long, 100 μm deep).

Actually, commercial implementation of MCR for F-T was proposed by Velocys, Inc. and Compact GTL [55]. In a report made for the International Petroleum Technology Conference in Qatar [56], Velocys claimed that the use of a highly active cobalt catalyst (Velocys OMX catalyst) in MCRs were able to improve F-T product yield and was capable of maintaining consistence performance even after regeneration. This report also demonstrated that for a reactor operating at: 350 psig, 12,415 GHSV, H₂/CO syngas feed ratio of 2/1; temperatures between 198-202 °C, the CO conversions was 80-87 %, while the highest C₅₊ selectivity achieved was 88.53 %.

According to Velocys [57], The first small-scale GTL facility in the U.S. would be built in a joint venture with Ventech, Waste Management and NRG Energy. The plant will be located in Oklahoma and it is expected to begin operations by the end of this year (2016). The plant is projected to produce clean diesel fuel and chemicals from landfill and natural gas. Similarly, in an effort to reduce gas flaring from oil production in Kazakhstan, the CompactGTL company in a joint venture with the Republic of Kazakhstan plans to build a 3,000 bbl/d commercial GTL facility with their proprietary mini-channel reactor design along with a two-stage F-T process. The plant is projected to start commercial operations in 2018. This company has currently two demonstration small-scale GTL plants in Brazil (with Petrobras) and in the United Kingdom [58].

2.0 OBJECTIVE

Even though MCRs were proposed for commercial implementations and demonstration plans have already been built, adequate literature publications on the use of MCRs in F-T synthesis is scanty and to our knowledge many details concerning the hydrodynamics, mass transfer, heat transfer performance of MCRs cannot be found. Therefore, the overall objective of this research is to investigate the hydrodynamics, mass transfer and kinetics of the MCRs for Low-Temperature F-T (LTFT) synthesis in order to produce alkanes using a Co-based catalyst on silica support. In order to achieve this objective, the following tasks are performed:

1. Build a one dimensional (1-D) MCR model to evaluate the effects of catalyst shape and packing configuration on the reactor performance.
2. Build a Computational Fluid Dynamics (CFD) model of the MCR, which accounts for the pressure drop and F-T reaction kinetics, in order to provide fundamental understanding of the overall performance of the reactor considering different operating conditions.
3. Compare the performance between both models based on reactants conversion and pressure drop.
4. Propose a geometry for the MCR inlet and model the fluid distribution of the syngas to the microchannels.

3.0 RESEARCH APPROACH

3.1 CONFIGURATION OF THE MCR INVESTIGATED

The MCR used in this study consists of 2 parallel packed sections with 25 channels each. The individual channel dimensions are 10 mm× 2 mm× 150 mm. The inlet gas feed stream enters at the top of the channels and the products come out of the bottom. The reactor is cooled using a cross flow configuration cooling, where water enters at the side of the reactor and comes out at the opposite side.

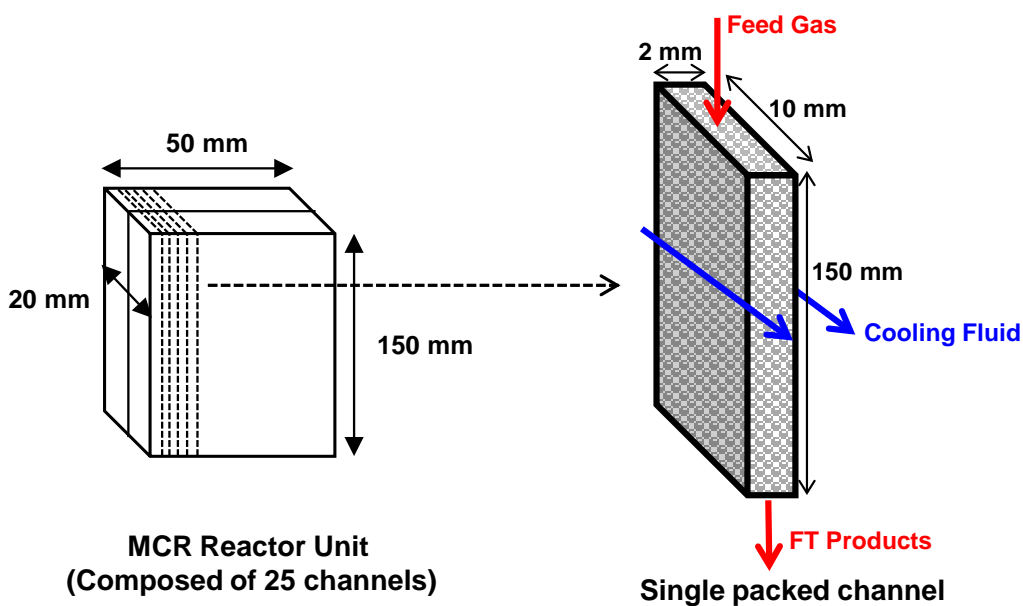


Figure 3-1: Dimensions of the MCR unit and the packed channel investigated in this study

The operating conditions used in this investigation are listed in Table 3-1. The kinetic rate expression by Keyser et al. [59] for a Co-based catalyst on silica support was used as shown in Equation (3-1).

Table 3-1: Microchannel Operating Conditions

Temperature	Pressure	Inlet Velocity	Inlet Gas (wt.%)	
K	bar	m/s	CO	H ₂
500	25	0.05	0.8742	0.1258

$$r_{FT} = k_{FT} \frac{P_{H_2} P_{CO}}{P_{CO} + P_{H_2O}} \quad (3-1)$$

In this study, six main reactions were considered, as shown in **Error! Reference source not found.** The CO in the feed was assumed to be equally distributed by mass among these six reactions.

Table 3-2: Reactions and products list

Product	Reaction	ΔH°_R (kJ/mol)
Methane	$CO + 3H_2 \rightarrow CH_4 + H_2O$	-248.700
Butane	$CO + 2.25H_2 \rightarrow 0.25C_4H_{10} + H_2O$	-206.748
Pentane	$CO + 2.20H_2 \rightarrow 0.20C_5H_{12} + H_2O$	-262.055
Decane	$CO + 2.10H_2 \rightarrow 0.10C_{10}H_{22} + H_2O$	-205.390
Tetradecane	$CO + 2.07H_2 \rightarrow 0.07C_{14}H_{30} + H_2O$	-204.104
Tetracosane	$CO + 2.04H_2 \rightarrow 0.04C_{24}H_{50} + H_2O$	-206.129

Subsequently, a 2- α probability distribution was investigated for the proposed hydrocarbon products, which is represented as follows [60]:

$$\ln(M_f) = \ln[A\alpha_1^{n-1} + B\alpha_2^{n-1}] \quad (3-2)$$

Where

$$B = A \left(\frac{\alpha_1}{\alpha_2} \right)^{\zeta-1} \quad (3-3)$$

$$A = \frac{1}{\frac{1}{1-\alpha_1} + \left(\frac{\alpha_1}{\alpha_2} \right)^{\zeta-1} \left[\frac{1}{1-\alpha_2} \right]} \quad (3-4)$$

For this 2- α probability model, ζ is the point at which the semi-logarithmic plot between the mass fractions and the carbon numbers starts to show a deviation from a linear behavior and is represented by the estimated carbon number at which this occurs. In our case, this point occurs at $n = 6$ according to the data plotted in Figure 3-2. This distribution suggests a chain probability growth for the low carbon numbers α_1 and a second one for the high carbon numbers α_2 . Following this model, the linear regression model is divided in two sections and the results give $\alpha_1 = 0.659$ (with $R^2 = 98.7\%$) and $\alpha_2 = 0.941$ (with $R^2 = 98.8\%$).

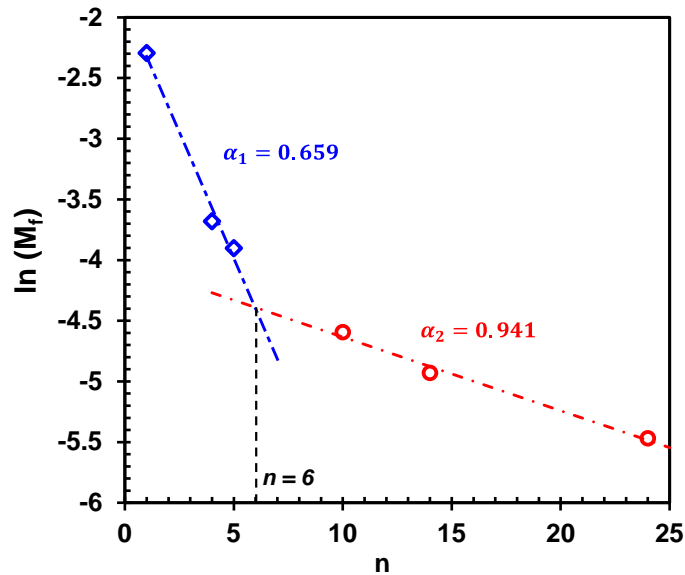


Figure 3-2: Double chain probability growth model

3.2 PRESSURE DROP PREDICTION

The pressured drop was represented by Ergun's generalized equation given in Equation (3-5). This equation includes two terms for laminar (viscous) and turbulent (inertial) pressure drops. The viscous and inertial coefficients, denoted as $K_{viscous}$ and $K_{inertial}$, respectively, were identified for six different pressure drop models taken from the literature, as shown in Table 3-3.

$$\frac{\Delta P}{L} = \underbrace{\frac{K_{viscous} \cdot \mu u}{d_p^2 \varepsilon_B^3}}_{\text{Viscous term}} + \underbrace{K_{inertial} \cdot \frac{\rho u^2}{2}}_{\text{Inertial term}} \quad (3-5)$$

Table 3-3: Pressure drop models

Reference	$K_{viscous}$	$K_{inertial}$
Ergun (1952) [61]	$\frac{150(1 - \varepsilon_B)^2}{d_p^2 \varepsilon_B^3}$	$\frac{3.5(1 - \varepsilon_B)}{d_p \varepsilon_B^3}$
Mehta & Hawley (1969) [62]	$\frac{150(1 - \varepsilon_B)^2}{d_p^2 \varepsilon_B^3} \left(1 + \frac{2d_p}{3d_h(1 - \varepsilon_B)}\right)^2$	$\frac{3.5(1 - \varepsilon_B)}{d_p \varepsilon_B^3} \left(1 + \frac{2d_p}{3d_h(1 - \varepsilon_B)}\right)$
Tallmadge et al. (1970) [63]	$\frac{150(1 - \varepsilon_B)^2}{d_p^2 \varepsilon_B^3}$	$\frac{8.4(1 - \varepsilon_B)}{d_p \varepsilon_B^3 \left(\frac{Re_p}{1 - \varepsilon_B}\right)^{1/6}}$
Liu et al. (1994) [64]	$\frac{150(1 - \varepsilon_B)^2}{d_p^2 \varepsilon_B^3} \left(1 + \frac{\pi d_p}{6d_h(1 - \varepsilon_B)}\right)^2$	$\frac{3.5(1 - \varepsilon_B)}{d_p \varepsilon_B^3} \left(1 - \frac{\pi^2 d_p}{24d_h} \left(1 - 0.5 \frac{d_p}{d_h}\right)\right)$
Eisfeld & Schnitzlein (2001) [65]	$\frac{K_1(1 - \varepsilon_B)^2}{d_p^2 (\varepsilon_B^3)} \left(1 + \frac{2/3}{\left(\frac{d_h}{d_p}\right)(1 - \varepsilon_B)}\right)^2$	$\frac{2(1 - \varepsilon_B)}{d_p \varepsilon^3} \left(\frac{1 + \frac{2}{3\left(\frac{d_h}{d_p}\right)(1 - \varepsilon_B)}}{\left(k_1 \left(\frac{d_p}{d_h}\right)^2 + k_2\right)^2}\right)$
	$K_1 = 154, k_1 = 1.15, k_2 = 0.87$ for spherical particles $K_1 = 190, k_1 = 2.0, k_2 = 0.83$ for cylindrical particles	
Harrison et al. 2013 [66]	$\frac{119.8(1 - \varepsilon_B)^2}{d_p^2 \varepsilon_B^3} \left(1 + \frac{\pi d_p}{6d_h(1 - \varepsilon_B)}\right)^2$	$\frac{9.26(1 - \varepsilon_B)}{d_p \varepsilon_B^3 \left(\frac{Re_p}{1 - \varepsilon_B}\right)^{1/6}} \left(1 - \frac{\pi^2 d_p}{24d_h} \left(1 - 0.5 \frac{d_p}{d_h}\right)\right)$

The pressure drop was calculated for different superficial gas velocities using the operating conditions given in Table 3-4 and the results are shown in Figure 3-3. As can be seen in this figure, the highest pressure drop was predicted using the correlation by Einfeld and Schnitzlein [65], and was therefore selected to represent the pressure drop in the MCR model.

Table 3-4: Data for Pressure Drop Models evaluation

Parameter	Units	
Temperature	K	500
Pressure	bar	30
Length (bed)	m	0.3048
Syngas Density (ρ) ($H_2:CO = 2$)	kg/m ³	7.6185
d_h/d_p	-	33.3
Dynamic Viscosity (μ)	Pa.s	2.4256×10^{-5}
Particle Diameter (d_p)	m	0.0001
Porosity (ϵ)	-	0.30
Superficial Velocity (V_s)	m/s	0.01-0.1
Hydraulic diameter (d_h)	m	0.0033
Sphericity (ϕ)	-	1.0000

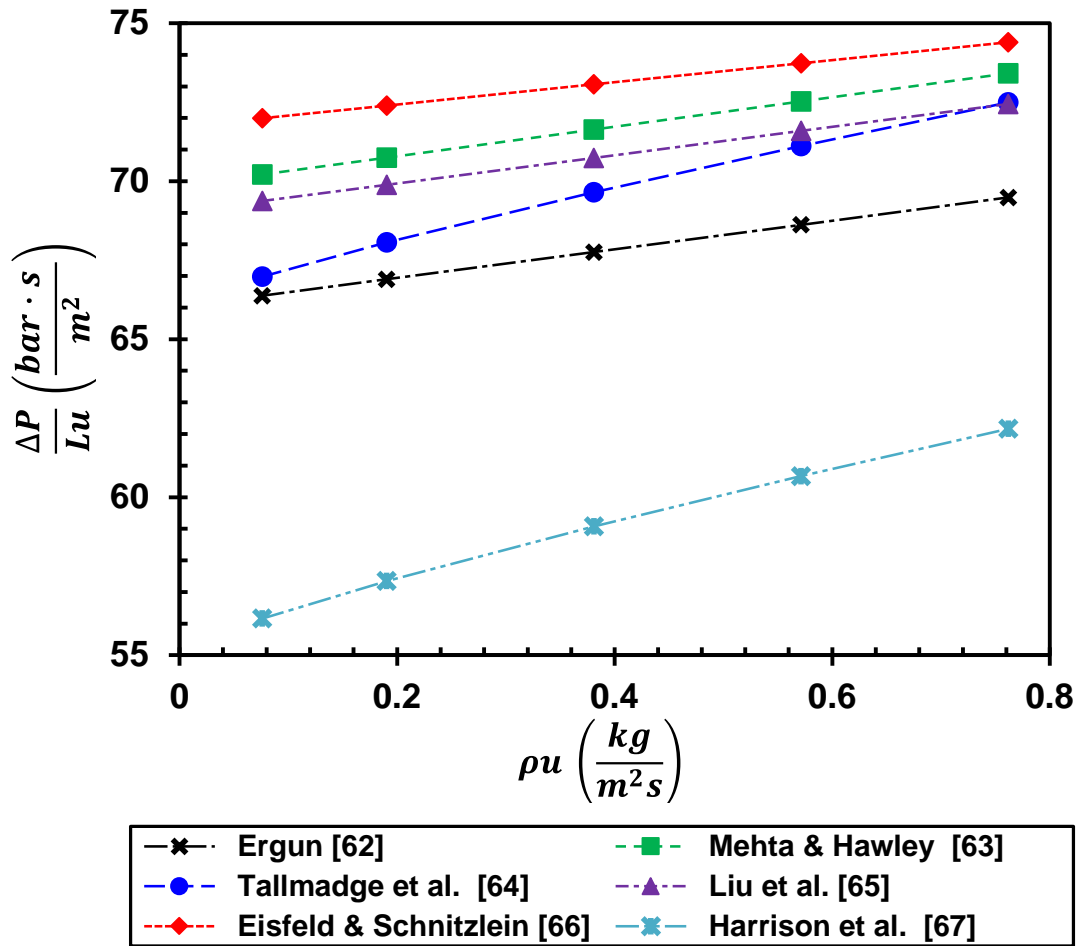


Figure 3-3: Pressure drop prediction using different models

3.3 MASS TRANSFER IN MCR

Figure 3-7 shows a schematic of the gas-liquid-solid interactions in the MCR. As can be seen in this figure, the gas reactant must first dissolve in the liquid-phase, travel through the gas-liquid film, liquid bulk and then the liquid-solid film on the catalyst particle to reach the active sites on catalyst surface or inside the pores for the reaction to take place.

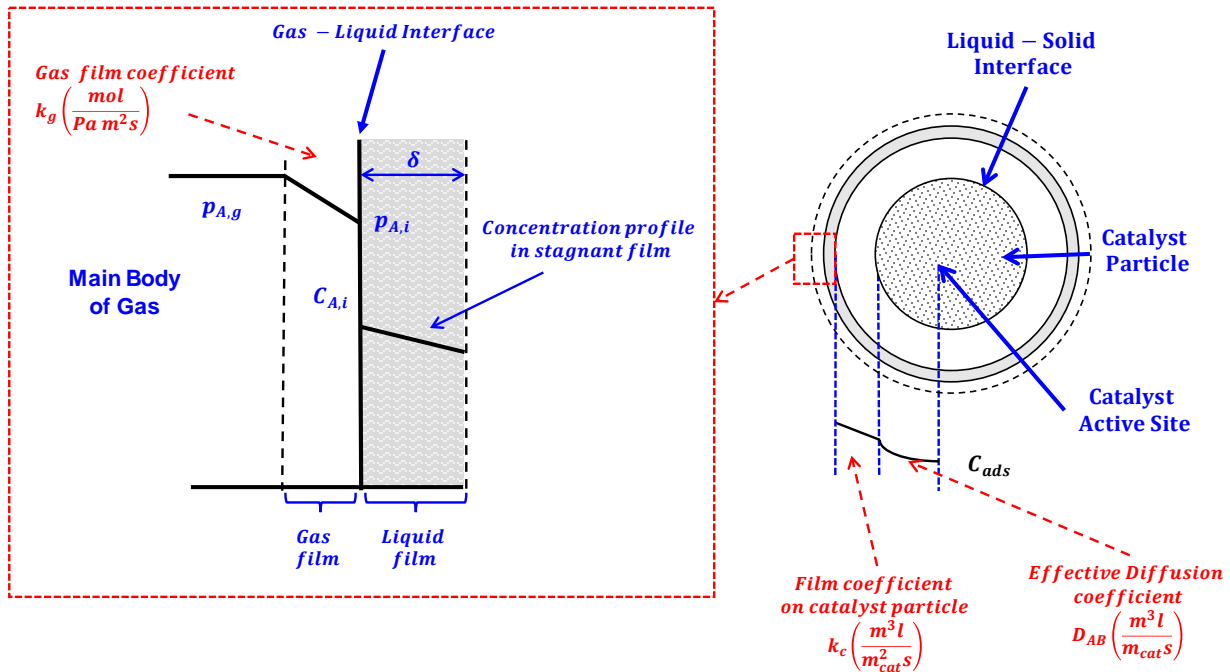


Figure 3-4: Schematic of a gas-liquid-solid interactions in the MCR

The gas solubility into the liquid-phase can be expressed by Henry's Law constant, H as:

$$H \left(\frac{\text{Pa m}^3}{\text{mol}} \right) = \frac{p_{A,i}}{C_{A,i}} \quad (3-6)$$

The effect of temperature on Henry's law constant is given in Equation (3-7) and depicted in Figure 3-5.

$$\ln(H_A) = \ln(H_{A,o}) + \frac{A}{T^2} + \frac{B}{T} \quad (3-7)$$

The values for $H_{A,o}$, A and B for H₂ and CO in alkanes were taken from Soriano et al. [67].

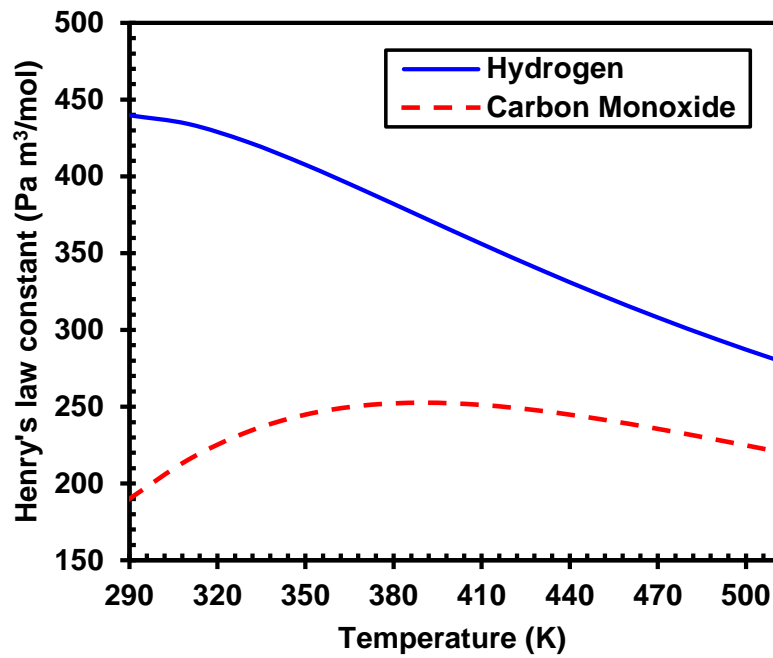


Figure 3-5: Henry's law constants for H₂ and CO

Assuming the two-film model is applicable, the mass transfer flux across a stagnant gas-film, gas-liquid interface and liquid-solid interfaces can be written as Equations (3-8), (3-9) and (3-10), respectively.

$$J_G = k_{A,g} a_i (P_{A,g} - P_{A,g}^*) \quad (3-8)$$

$$J_L = k_{A,l} a_i (C_{A,i} - C_{A,L}) \quad (3-9)$$

$$J_S = k_c a_{cat} (C_{A,L} - C_{ads}) \quad (3-10)$$

In these equations a_i and a_{cat} are defines by Equations (3-11) and (3-12), respectively.

$$\text{Gas Liquid Interfacial area:} \quad a_i = \frac{\text{Gas Liquid Interfacial area}}{\text{Volume of reactor}} \quad (3-11)$$

$$\text{Liquid Solid Interfacial area:} \quad a_{cat} = \frac{\text{External surface of particles}}{\text{Volume of reactor}} \quad (3-12)$$

$$a_{cat} = \frac{6\varepsilon_s}{d_p} \text{ (for Spherical particles)}$$

Where $\varepsilon_s = \text{solid loading}$

For a first order reaction of a species A, the flux at the surface equals the rate of species transport to the catalyst surface according to Equation (3-13).

$$r = k_{reaction} C_{A,s} = k_{mass-transfer} (C_{A,g} - C_{A,s}) \quad (3-13)$$

Solving for $C_{A,s}$

$$C_{A,s} = \frac{k_{mass-transfer} (C_{A,g})}{k_{reaction} + k_{mass-transfer}} \quad (3-14)$$

Substituting the value of $C_{A,s}$ into the left-hand-side of Equation (3-13) gives:

$$r = k_{reaction} \left(\frac{k_{mass-transfer} (C_{A,g})}{k_{reaction} + k_{mass-transfer}} \right) \quad (3-15)$$

Rearranging the above equation:

$$r = \frac{C_{A,g}}{\frac{1}{k_{reaction}} + \frac{1}{k_{mass-transfer}}} \quad (3-16)$$

Where:

$$\frac{1}{k_{mass-transfer}} = \frac{1}{k_{A,g}a_iH_A} + \frac{1}{k_{A,l}a_i} + \frac{1}{k_{Ac}a_c} \quad (3-17)$$

And:

$$\frac{1}{k_{reaction}} = \frac{1}{(k'_A a_{cat})\eta\varepsilon_s} \quad (3-18)$$

Where η is the effectiveness factor for the first order reaction of A with a rate constant = k'_A . Based on the resistances shown in Figure 3-7 and the assumption that concentrations do not change at the interfaces, the following overall rate equation is applicable.

$$-r_A = \frac{1}{V_r} \frac{dN_A}{dt} = \frac{C_{A,g}}{\frac{1}{k_{A,g}a_iH_A} + \frac{1}{k_{A,l}a_i} + \frac{1}{k_{Ac}a_c} + \frac{1}{(k'_A)\eta\varepsilon_s}} \quad (3-19)$$

Generally, $\left(\frac{1}{k_{A,g}a_i}\right)$ and $\left(\frac{1}{k_{Ac}a_c}\right)$ are negligible and accordingly the only remaining resistances are due to kinetics and gas-liquid film.

The reaction rate of Keyser et al. [59] is:

$$r_{FT} \left(\frac{mol}{g_{cat}S} \right) = k_{FT} \frac{P_{H_2}P_{CO}}{P_{CO} + bP_{H_2O}} \quad (3-20)$$

Assuming that the mass transfer through the liquid film cannot be ignored, the mass balance is represented as follows:

$$\frac{\partial u_{G,i}C_{G,i}}{\partial z} = k_L a_{GL} (C^* - C_{A,l}) + r_{FT} \quad (3-21)$$

The above equation can be rewritten as:

$$\frac{\frac{\partial u_{A,L} C_{i,L}}{\partial z}}{\frac{\text{mol}}{\text{m}^3 \text{s}}} = \underbrace{k_L}_{\frac{\text{m}}{\text{s}}} \underbrace{a_{GL}}_{\frac{1}{\text{m}}} \underbrace{(C^* - C_{A,L})}_{\frac{\text{mol}}{\text{m}^3}} + \eta \underbrace{r_{FT} \rho_{cat} \epsilon_B}_{\frac{\text{mol}}{\text{m}^3 \text{s}}} \quad (3-22)$$

Where ϵ_B is the bed porosity.

The equilibrium solubilities (C^*) were determined using Henry's law assuming that the gases will reach equilibrium solubility in the liquid film.

Since gas bubbles will not form in the MCR and the solid particles could be completely covered by a thin liquid film, there will be no bulk-liquid phase and accordingly the gas-liquid interfacial area could be represented by the effective wetted catalyst area. Therefore, the specific surface area of the gas-liquid interface was estimated according to McCabe and Smith [68] as:

$$a_{GL} = \frac{6(1 - \epsilon_B)}{d_{wett}} \quad (3-23)$$

Where, d_{wett} is a value, which could be greater than the actual outer diameter of the wetted catalyst particle.

The value of k_L , on the other hand, was estimated using the following relationship for packed-beds by Davis and Davis [69]. The k_L values were estimated to be in the order of 10^{-3} m/s at $T = 493$ K and $P = 25$ bar.

$$k_L = \frac{D_{AB}^{2/3} u_g^{0.5} \rho_l^{1/6}}{(0.5 d_{wett})^{0.5} \mu_l^{1/6}} \quad (3-24)$$

The diffusivities were also estimated using Equation (25) by Erkey et al. [70] to be in the order of 10^{-8} m²/s. Also, The values of the different parameters were taken for a paraffin mixture from Sehabiague [2].

$$D_{AB} = 1.1728 \times 10^{-16} \frac{T\sqrt{Mw_l}}{\mu_l v_i^{0.6}} \times 100\% \quad (3-25)$$

The CO conversion was calculated as follows:

$$X_{CO} = \frac{C_{CO,in} - C_{CO,out}}{C_{CO,in}} \times 100\% \quad (3-26)$$

Equations (3-20) through (3-25), coupled with Equation (3-7) for Henry's law constant were solved using Matlab R2014a under the following conditions: inlet superficial gas velocity = 0.5 m/s, bed porosity = 32%, particle diameter = 100 μm , wetted diameter (d_{wett}) = 150 μm and a catalyst density = 4,840 kg/m^3 . Figure 3-6 clearly that the effect of mass transfer on the CO conversion in the MCR used in this study can be safely neglected.

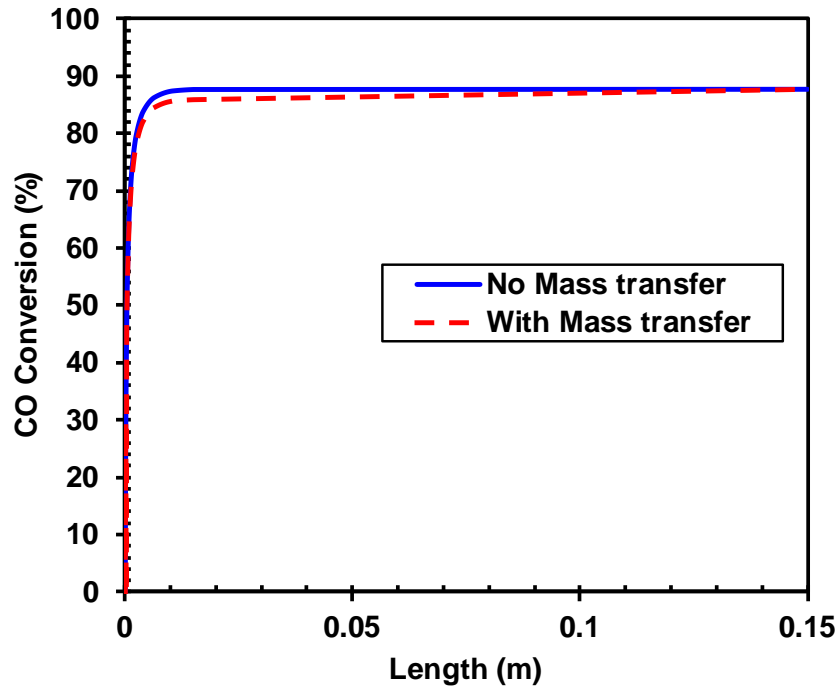


Figure 3-6: CO conversions with and without mass transfer

3.4 DEVELOPMENT OF A ONE-DIMENSIONAL MODEL FOR THE MCR

The preceding section indicated that the gas-liquid mass transfer in the MCR under the conditions used in this study can be safely neglected without compromising the accuracy of the CO conversion. Thus, a one-dimensional (1-D) model for only gas-phase reactions was developed for the MCR in Matlab R2014a. It consists of the following:

1. 9 material balance equations, as shown in Equations (3-27) to (3-35), for CO, H₂, H₂O, C₁, C₄, C₅, C₁₀, C₁₄ and C₂₄, respectively.

$$\frac{dF_{CO}}{dl} = r_{CO}A \quad (3-27)$$

$$\frac{dF_{H_2}}{dl} = r_{H_2}A \quad (3-28)$$

$$\frac{dF_{H_2O}}{dl} = r_{H_2O}A \quad (3-29)$$

$$\frac{dF_{CH_4}}{dl} = r_{CH_4}A \quad (3-30)$$

$$\frac{dF_{C_4H_{10}}}{dl} = r_{C_4H_{10}}A \quad (3-31)$$

$$\frac{dF_{C_5H_{12}}}{dl} = r_{C_5H_{12}}A \quad (3-32)$$

$$\frac{dF_{C_{10}H_{22}}}{dl} = r_{C_{10}H_{22}}A \quad (3-33)$$

$$\frac{dF_{C_{14}H_{30}}}{dl} = r_{C_{14}H_{30}}A \quad (3-34)$$

$$\frac{dF_{C_{24}H_{50}}}{dl} = r_{C_{24}H_{50}}A \quad (3-35)$$

Where, F_i is the molar flux and r_i is the rate of consumption/formation of the i^{th} species, and A is the cross-sectional area of the channel (20 mm²). The rate of consumption/formation of the species depends on the rate of F-T reaction rate (r_{FT}), stoichiometric coefficients (v_i), catalyst

effectiveness factor (β) and catalyst mass per unit reactor volume (m_{cat}). It can be expressed as is indicated in Equation (3-27) [33]: The stoichiometric coefficient for each component were taken to be -6, -13.63, 1, 0.25, 0.2, 0.1, 0.071, 0.042 for CO, H₂, C₁, C₄, C₅, C₁₀, C₁₄ and C₂₄, respectively, based on the reaction set shown above.

$$r_i = v_i \beta m_{cat} r_{FT} \quad (3-36)$$

2. The F-T reaction rate kinetics expression proposed by Keyser et al. [59] was incorporated into the model (Equation (3-1)) and the kinetic model was then rearranged, in terms of the molar fluxes of the species, as follows.

$$r_{FT} = \left(\frac{k_{FT} Z F_{CO} F_{H_2}}{F_{CO} + b F_{H_2O}} \right) \left(\frac{RT \rho_{cat}}{F_t} \right) \quad (3-37)$$

Two cobalt catalysts with different physical properties, as shown in **Table 3-5**, were used in the 1-D model. These properties were taken from Philippe et al. [71], based on a cobalt catalyst supported on silicon carbide (70/30 SiC-Co).

Table 3-5: Catalysts used in th 1-D model

Shape	Porosity (ϵ)	d_p (μm)	ρ_{cat} (kg/m^3)
Spherical -1	0.260	100	4,840
Spherical -2	0.320		
Spherical -3	0.476		
Cylindrical-1	0.375	100 (equivalent diameter)	950
Cylindrical-2	0.395		
Cylindrical-3	0.455		
Cylindrical-4	0.481		

The MCR model was considered to operate with a cobalt catalyst, which has negligible WGS reactions. Therefore, only the reaction rate for the F-T synthesis was used. k_{FT} was represented using a general Arrhenius-type expression with an activation energy $E_{FT} = 79.9 \pm 0.6 \frac{J}{mol}$ at 220 °C, as follows:

$$k_{FT} = 0.18597 \exp\left(-\frac{E_{FT}}{RT}\right) \quad (3-38)$$

3. The Peng-Robinson Equation-of-State (P-R EOS), Equation (3-39) and its expanded form, Equation (3-40), was used to obtain the compressibility factor (Z) of the gas mixture.

$$P = \frac{RT}{v - b} - \frac{a}{v^2 + 2bv - b^2} \quad (3-39)$$

$$Z^3 - (1 - B)Z^2 + (A - 3B^2 - 2B)Z - (AB - B^2 - B^3) = 0 \quad (3-40)$$

Where:

$$A = \frac{aP}{R^2T^2} \quad (3-41)$$

$$B = \frac{bP}{RT} \quad (3-42)$$

$$z = \frac{Pv}{RT} \quad (3-43)$$

$$a = \sum_i \sum_j y_i y_j a_{ij} \quad (3-44)$$

$$b = \sum_i y_i b_i \quad (3-45)$$

$$a_{ij} = (1 - \delta_{ij})\sqrt{a_i a_j} \quad (3-46)$$

$$a_i = 0.45724 \frac{R^2 T_c^2}{P_c^2} [1 + \kappa [1 - T_R^{0.5}]] \quad (3-47)$$

$$b_i = 0.0778 \frac{RT_c}{P_c} \quad (3-48)$$

$$\kappa = 0.37464 + 1.5422\omega - 0.26992\omega^2 \quad (3-49)$$

It should be noted that the binary interaction parameters used in the mixing rules (δ_{ij}) for the species involved were taken from ASPEN PLUS.

4. The pressure drop was calculated using the correlation by Einfeld and Schnitzlein [65], as shown in Equation (3-50).

$$\begin{aligned} \frac{dP}{dl} = & \frac{K_1(1 - \varepsilon_B)^2}{d_p^2(\varepsilon_B^3)} \left(1 + \frac{2/3}{\left(\frac{d_h}{d_p}\right)(1 - \varepsilon_B)} \right)^2 \cdot \mu u \\ & + \frac{2L(1 - \varepsilon_B)}{d_p \varepsilon^3} \left(\frac{1 + \frac{2}{3\left(\frac{d_h}{d_p}\right)(1 - \varepsilon_B)}}{\left(k_1 \left(\frac{d_p}{d_h}\right)^2 + k_2\right)^2} \right) \cdot \frac{\rho u^2}{2L} \end{aligned} \quad (3-50)$$

All equations were solved using MATLAB R2014a and the output results are the hydrocarbons molar flow rates, CO conversion, and pressure drop using a 150 mm length microchannel with the seven catalysts listed in **Table 3-5**. The boundary conditions were set to be the inlet molar flows and pressure.

3.5 DEVELOPMENT OF A CFD MODEL FOR THE MCR

The CFD model is based on a multi-Eulerian approach, which has been previously used in MCR modeling studies [72–75]. The effect of the porous bed was incorporated by overlaying a scalar pressure drop correlation within the porous region. The multiphase Eulerian approach with the porous media model has proven to be useful in modeling fluid flows in packed-beds; however, it suffers from the following drawbacks [76]:

1. ANSYS Fluent considers, by default, a superficial velocity formulation. For better results it is recommended to use a physical velocity resistance formulation, where the porosity is considered for the convection and diffusion terms in all the transport equations.
2. The heat capacity of the material in the porous zone should be entered as a constant value.
3. The effects in the turbulence field due to the porous medium are approximated.

The following model assumptions and parameters were made:

1. Laminar flow;
2. Constant packing fraction;
3. No-slip velocity conditions at the walls; and
4. Isothermal operation.

3.5.1 Inlet geometry mesh of the MCR

The geometry used in the CFD model is shown in Figure 3-7, which represents the inlet to the MCR. It has a 10 mm ID and the reactants pass through a 25 mm chamber before entering the packed-channels. The dark grey box represents the 50 process micro-channels with a length of 40 mm each. It should be noted that the channels were shortened to a length of 40 mm to reduce the

computational time required by ANSYS Fluent. The channels are arranged in two lines of 25 each and are separated by a 0.25 mm distance. This geometry is intended only to depict the flow distribution zone, i.e., the upper area of the reactor and the inlets to the channels. The horizontal cooling channels are not considered in this illustration.

Furthermore, the geometry was modified to investigate the effect of the presence of a flow distributor, where two layers of solid spheres with diameters between 0.5 mm and 2 mm were placed 5 mm above the micro-channels inlet in order to achieve a homogenous distribution of the gas flow, as shown in Figure 3-8.

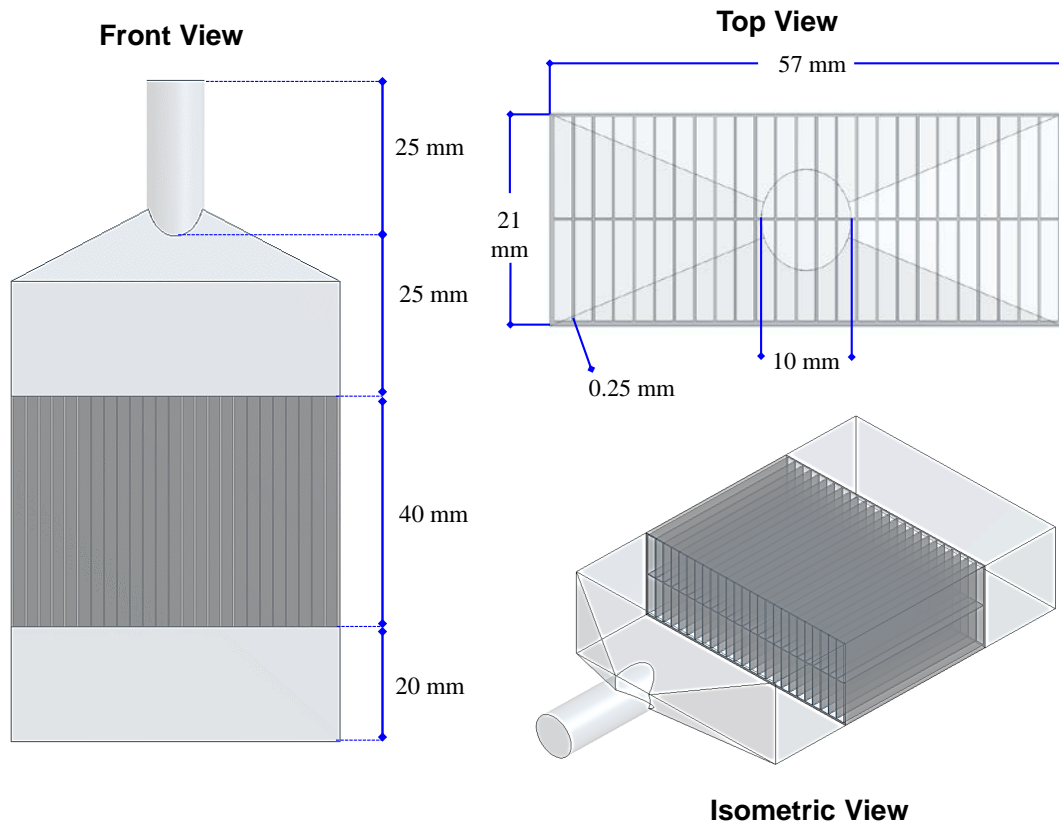


Figure 3-7: MCR geometry used in the CFD model

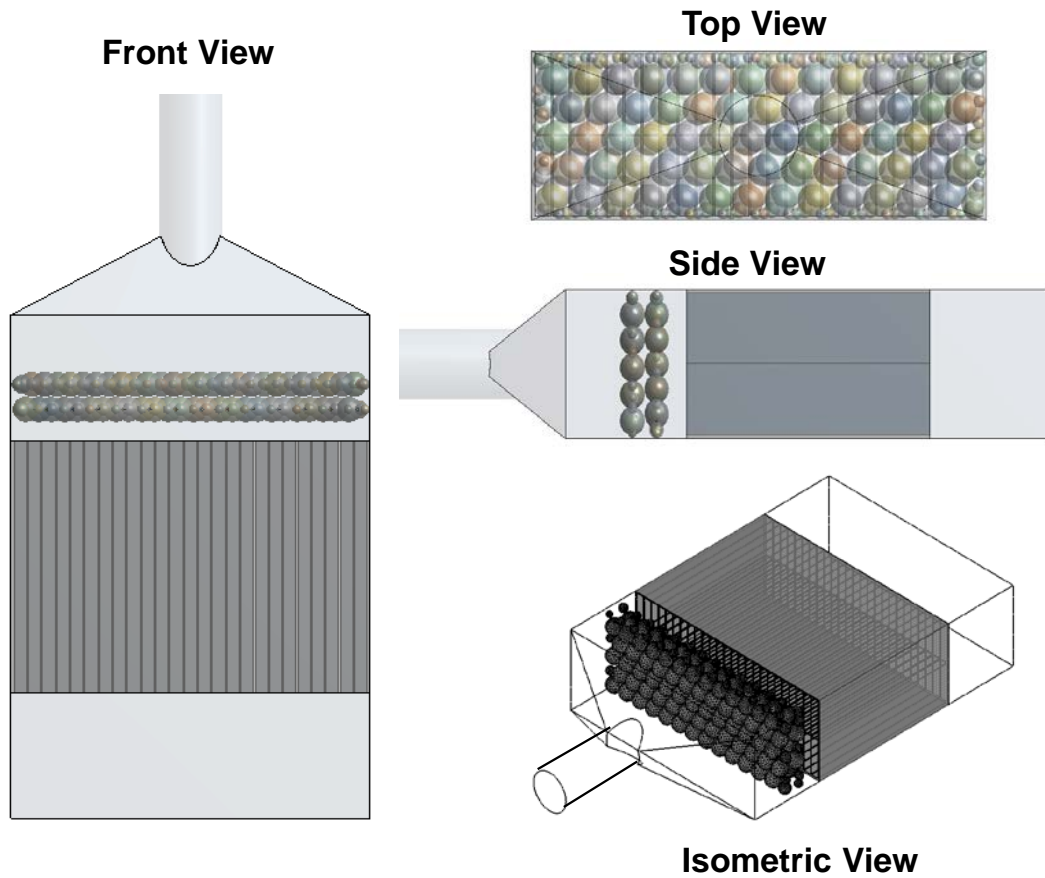


Figure 3-8: Reactors housing with flow distributor

3.5.2 Conservation Equations for Multiphase Flow

The mass and momentum conservation equations used in this CFD model are described in this section. For multiphase flow through the porous media, the volume fractions of each phase (α) are included in the conservation equations for mass, momentum and the energy equation [76].

3.5.2.1 Conservation of Mass.

$$\frac{\partial}{\partial t}(\varepsilon_B \alpha_q \rho_q) + \nabla \cdot (\varepsilon_B \alpha_q \rho_q \overline{u}_q) = \varepsilon_B \sum_{p=1}^n (m_{pq} + m_{qp}) \quad (3-51)$$

Where q denotes phase “ q ”, and p denotes phase “ p ”. Note that for the packed-bed system, the velocity of the solid phase is zero. Also, no mass transfer is considered between the solid and the gas/liquid phase. Therefore, the mass conservation equation is reduces to that of a single-phase flow:

$$\frac{\partial}{\partial t}(\varepsilon_B \alpha_q \rho_q) + \nabla \cdot (\varepsilon_B \alpha_q \rho_q \overline{u}_q) = 0 \quad (3-52)$$

3.5.2.2 Conservation of Momentum

The momentum conservation equation is represented as:

$$\begin{aligned} \frac{\partial}{\partial t}(\varepsilon_B \alpha_q \rho_q \overline{u}_q) + \nabla \cdot (\varepsilon_B \alpha_q \rho_q \overline{u}_q \overline{u}_q) & \quad (3-53) \\ & = -\varepsilon_B \alpha_p \nabla P + \nabla \cdot (\varepsilon_B \overline{\tau}_q) + \varepsilon_B \alpha_p \rho_p \vec{g} + \varepsilon_B \sum_{p=1}^n (\overline{R}_{pq}) \\ & - \alpha_q \left(\frac{\varepsilon_B^2 \mu}{K_q} \overline{u}_q + \frac{\varepsilon_B^3 C_{2q}}{2} \rho_q [\overline{u}_q] \overline{u}_q \right) \end{aligned}$$

In the left-hand-side of this equation, the first and second expressions represent the transient and convective terms, respectively. In the right-hand-side, the first term represents the pressure p exerted by the opposite phase, the second term represents the shear stress tensor $\overline{\tau}_q$ and the third term is the gravity \vec{g} expression, which accounts for the body forces. The next two terms

in the RHS describe the phase interaction forces where $\overrightarrow{R_{pq}}$ represents the interaction force between the phases, which depends on the friction, pressure and cohesion of the phases and on the exchange coefficient K_{pq} , as follows:

$$\overrightarrow{R_{pq}} = K_{pq}(\overrightarrow{v_q} - \overrightarrow{v_p}) \quad (3-54)$$

The exchange coefficient K_{pq} depends on the nature of the phases, fluid-solid or fluid-fluid or solid-solid. It should be mentioned that the simulations presented in this study only covers fluid-fluid and fluid-solid interactions.

For gas-liquid flows, K_{pq} is represented as follows:

$$K_{GL} = K_{LG} = \frac{\alpha_q \alpha_p \rho_p f}{\sigma_p} \quad (3-55)$$

Where f corresponds to the drag function which is calculated according to the Schiller and Naumann [77] drag model as:

$$C_{D,GL} = \begin{cases} \left(\frac{24}{Re_p}\right) (1 + 0.15 Re_p^{0.687}) & Re_p < 1000 \\ 0.44 & Re_p \geq 1000 \end{cases} \quad (3-56)$$

C_D is the drag coefficient, and Re is the Reynolds number calculated for the primary-phase (gas). σ_p represents the particulate relaxation time, which is a function of the density and diameter of the solid as well as the viscosity of the gas [78].

$$\sigma_p = \frac{\rho_p d_p^2}{18\mu_q} \quad (3-57)$$

For gas-solid or liquid-solid flows, K_{pq} is represented using the Gidaspow model [79] which is a result of the consolidation of the Wen and Yu [80] model and the Ergun's equation [61]:

$$K_{G/L-S} = 150 \frac{(1 - \alpha_q)^2 \mu_q}{\alpha_q d_p^2} + 1.75 \frac{\rho_q (1 - \alpha_q) |u - \bar{u}_q|}{d_p} \quad (3-58)$$

The last term in the momentum equation describes the flow resistance condition present in the porous medium due to the viscous and inertial forces.

3.5.3 Fischer-Tropsch Reaction Kinetics

When accounting for the chemical reactions, an additional species conservation equation has to be considered as follows:

$$\frac{\partial(\rho_q \varepsilon_B y_k^i)}{\partial t} + \nabla(\rho_q \varepsilon_B u_q y_q^i) = \nabla(\varepsilon_B \rho_q D_q^i \nabla y_q^i) + r_q^i - r_{qp}^{ij} \quad (3-59)$$

Where y_q^i represents the mass fraction of species i in phase q , whereas r_q^i and r_{qp}^{ij} represent the F-T reaction kinetics rate and the rate of chemical absorption, respectively. The kinetic rate expression Equation (3-37) by Keyser et al. [59] was used as mentioned in Section 3.4.

Based on the kinetic equations, a user defined function (UDF) was written and interpreted in the FLUENT interphase. In this function, the reaction rate had to be rearranged in terms of molar concentrations (kmol/m^3) as follows:

$$r_{FT} \left(\frac{\text{kmol}}{\text{m}^3 \text{s}} \right) = \left(\frac{k_{FT} C_{CO} C_{H_2}}{C_{CO} + b C_{H_2O}} \right) (RT \rho_{bulk}) \quad (3-60)$$

3.5.4 Thermo-physical Properties of the F-T Reactants and Products

The thermo-physical properties of each reaction component are listed in Table 3-6 at T = 500 K and P = 25 bar according to the simulation conditions.

Table 3-6: Reactants and products properties at T = 500 K (226.85 °C) and 25 bar [81, 82]

Formula	ρ	C_p	μ	σ	M_{wt}	T_c	P_c
	kg/m ³	J/kg·K	Pa·s	W/m·K	kg/kmol	K	bar
CO	16.68	1077	2.586×10 ⁻⁵	0.040	28.01	132.9	34.9
H ₂	1.20	14531	1.271×10 ⁻⁵	0.282	2.02	33.1	13.0
H ₂ O	12.38	3282	1.669×10 ⁻⁵	0.045	18.02	647.1	220.6
CH ₄	9.65	2940	1.716×10 ⁻⁵	0.069	16.04	190.6	46.0
C ₄ H ₁₀	40.48	2751	1.300×10 ⁻⁵	0.046	58.12	425.1	37.8
C ₅ H ₁₂	57.41	2895	1.340×10 ⁻⁵	0.041	72.15	468.8	33.6
C ₁₀ H ₂₂	559.82	3025	1.480×10 ⁻⁴	0.087	142.28	616.8	20.9
C ₁₄ H ₃₀	617.31	2842	2.430×10 ⁻⁴	0.104	198.39	691.0	14.4
C ₂₄ H ₅₀	670.38	2698	5.520×10 ⁻⁴	0.126	338.65	804.0	9.8

The properties for the heavier hydrocarbons (C₁₄ and C₂₄) were calculated using the Asymptotic Behavior Correlations (ABC) for F-T liquids developed by Marano and Holder [83]. The general ABC correlations has the following form for a specific carbon number:

$$Y = Y_{\infty,0} + \Delta Y_{\infty}(n - n_o) - \Delta Y_o \exp(-\beta(n \pm n_o)^{\gamma}) \quad (3-61)$$

- Where ΔY_{∞} and ΔY_o for V_L , $C_{pL/R}$ and λ_L are:

$$\Delta Y_{\infty} = A_{\infty} + B_{\infty}T + C_{\infty}T^2 + D_{\infty}T^3 \quad ; \quad Y_{\infty,0} \text{ for } \sigma_L \quad (3-62)$$

$$\Delta Y_o = A_o + B_oT + C_oT^2 + D_oT^3 \quad (3-63)$$

- For Ln (μ):

$$\Delta Y_{\infty} = A_{\infty} + \frac{B_{\infty}}{T} + C_{\infty} \ln(T) + D_{\infty} T^2 + \frac{E_{\infty}}{T^2} \quad (3-64)$$

$$\Delta Y_o = A_o + \frac{B_o}{T} + C_o \ln(T) + D_o T^2 + \frac{E_o}{T^2} \quad (3-65)$$

The coefficients in the above equations are given in Table 3-7.

Table 3-7: Temperature dependent ABC Parameter for properties of n-Paraffins [84]

	V_L (cm ³ /gmol)	C_{pL}/R -	$\ln(\mu)$ (Pa.s)		σ_L (W/m.K)
A_o	8592.3	- 58.0001	- 602.688	A_o	0.069096
B_o	- 85.7292	0.330453	77866.8	B_o	0.00173
C_o	0.280284	- 0.00059	198.006	C_o	0
D_o	- 0.000448451	3.24×10^{-8}	- 4.2×10^{-5}	D_o	0
E_o	0	0	- 2494770		
A_{∞}	12.7924	0.017812	0.02902		
B_{∞}	0.0150627	0.021419	- 241.023	$A_{\infty,o}$	0.212451
C_{∞}	- 1.30794×10^{-5}	- 3.4×10^{-5}	0.044096	$B_{\infty,o}$	- 4.10×10^{-5}
D_{∞}	1.59611×10^{-8}	2×10^{-8}	- 1.8×10^{-7}	$C_{\infty,o}$	0
E_{∞}	0	0	56561.7	$D_{\infty,o}$	0
β	5.519846	0.183717	2.476409	β	1.241494
γ	0.0690406	0.753795	0.011212	γ	0.235832
$Y_{\infty,o}$	0	0	57.8516		
n_o	- 1.388524	1.153418	- 2.29398	n_o	-1.20127

3.5.5 Pressure Drop Calculations

The pressure drop correlation by Einfeld and Schnitzlein [65] was used, as discussed in Section 3.3. The correlation is based on a bank of tests of over 2300 experimental data points and it is applicable to spherical, cylindrical, and granular particles with an aspect ratio (d_h/d_p) between 1.73-250 and particle Reynolds numbers between 0.07-17365.

3.5.6 Heat Transfer Calculations

The amount of heat released due to reactions was estimated based on the standard enthalpy of formation of the reactants and products, and the stoichiometric ratio in each chemical reaction. The total enthalpy of reaction is based on the number of moles of CO consumed for the formation of each product.

The heat contribution per reaction is the result of the heat of reaction per mole of CO times the consumed molar flow of CO in that reaction (F_{CO-i}). Finally, the overall heat released by the entire system will be the sum of all the specific reaction contributions.

$$Q = \Delta H_{RTOTAL} = \sum_{j=1}^N F_{CO-i} \Delta H_{R_i} \quad (3-66)$$

It should be pointed out that Q and ΔH_{RTOTAL} have negative signs indicating exothermic reaction where the heat is released from the channel to its surroundings. In order to maintain isothermal operation a proper cooling system capable of removing this heat is necessary. Due to the MCR configuration, the heat is removed using cross flow of saturated water. When the heat is transferred to the water, it will vaporize to produce low pressure steam. The amount of water required was determined using an energy balance as follows:

$$Q = \dot{m}_w h_{fg} \quad (3-67)$$

The heat transfer coefficient U for a crossflow type heat exchanger is defined by the total area of heat transfer A_s , the logarithmic mean temperature difference ΔT_{lm} , and the total heat transferred Q .

$$Q = UA_s F \Delta T_{lm} \quad (3-68)$$

Assuming the cooling water enters the reactor at 1 degree lower than that of the reaction temperature and is converted to steam at constant temperature, which is similar to the assumption by Arzamendi et al. [85]. Accordingly, the logarithmic mean temperature difference could be set to unity.

3.5.7 Mass Transfer Calculations

In this work, the mass transfer was incorporated into the mass conservation equations (Equation (3-48)) using the terms $(\dot{m}_{pq} + \dot{m}_{qp})$. In a typical gas- liquid-solid system, such as F-T, the gas-phase reactants have to diffuse from the gas bulk zone to the catalyst surface overcoming the gas-liquid interphase (between the gas bubble surface and the liquid bulk), the liquid bulk, and the liquid-solid interphase (between the liquid film and the catalyst particle). Additionally, since the reaction occurs inside the catalyst pores, the reactant must reach the inner catalyst active sites [86].

Provided that each interphase has its own mass transfer coefficient accounting for the resistant to the diffusion process and assuming that the liquid film is completely covering the solid surface of the catalyst, the reaction may be affected by k_{GL} (mass transfer coefficient for the gas-liquid interphase), and k_{LS} (mass transfer coefficient for the liquid-solid interphase) and their corresponding interfacial areas a_{GL} and a_{LS} [87]. If the solid phase is assumed to be covered only partially by the liquid phase, a third mass transfer resistance has to be considered between the gas-solid interphase k_{GS} and its corresponding interfacial area a_{GS} [88]. Additionally, the mass transfer in the liquid-phase may be affected by the mixing conditions in the reactor, and in the gas-phase by the reactants volatility [89].

When modeling the mass transfer phenomena in micro-structured reactors, Guettel et al. [90], Knochen et al. [33], Kreuzer et al. [88], and Lebens et al. [91], only considered the resistances occurring between the interphases. For F-T synthesis, the mass transfer in the bulk gas-phase can be neglected due to the high volatility of the F-T reactants, whereas, the mass transfer resistance in the bulk liquid-phase can also be neglected due to enhanced mixing [33, 88, 90, 91]. Subsequently, the dominant mass transfer resistance encountered by the gas will be in the liquid-solid film [86].

Under those circumstances, Knochen et al. [33] described the transport of the gas reactants through the liquid-solid interface in a micro reactor using the following equations:

$$k_{LS}a_{LS} = \frac{6D_{L,i}(1 - \varepsilon_B)}{d_p\delta_L} \quad (3-69)$$

$$\delta_L = \frac{\varepsilon_L d_p}{6(1 - \varepsilon_B)} \quad (3-70)$$

Where $D_{L,i}$ is the diffusion coefficient of the i^{th} species in the liquid, ε_B is the porosity of the packed-bed, d_p is the diameter of the catalytic particle, δ_L is the thickness of the liquid film and ε_L is the liquid holdup. In this model the liquid holdup was estimated experimentally, through the measurement of the pressure drop and its comparison with the calculated pressure drop in terms of the initial bed porosity.

In this study, the channels were considered to have a constant porosity of 0.375 with catalyst particles of 100 μm . The solid-phase was assumed to be covered by a thin film of liquid and the amount of liquid present in the reactor was obtained from the simulation results as the percentage of liquid products in the outlet stream.

Since the reactor is operating in a continuous flow, the amount of liquid present in the reactor was assumed to be constant through all the channels length. The diffusivity coefficients for the H₂ and CO were taken from [92] as 4.55x10⁻⁸ m/s² and 1.72x10⁻⁸ m/s², respectively.

The mass transfer coefficients must be obtained from the above equations in order to compare them to the pseudo-reaction rate coefficients and determine if the process is governed by the mass transfer rate or by the reaction rate [93]. In order to do this, it is necessary to have an expression for the gas-liquid interfacial area. Assuming that Fick's law may represent the diffusion of the gas species through the liquid film, the mass flux at steady state can be expressed as:

$$J_L = k_L a_L (C^* - C_L) \quad (3-71)$$

Where C^* is the concentration at the interphase, C_L is the concentration in the bulk-phase and k_L is the mass transfer coefficient through the gas-liquid interface, which is a function of the diffusion coefficient between the gas and the liquid and the thickness of the liquid film [86].

$$k_L = \frac{D_{AB}}{\delta} \quad (3-72)$$

Combining the prior definition for k_L with the correlation employed by Knochen et al [33] the interfacial area can be estimated as a function of the packing fraction of the bed ($1 - \varepsilon_B$) and the catalyst particle diameter d_p

$$a_{LS} = \frac{6(1 - \varepsilon_B)}{d_p} \quad (3-73)$$

Furthermore, the comparison between the pseudo-reaction rate coefficient and mass transfer coefficient is made under the assumption that the reactions occur at a pseudo-first order reaction where the reaction rate is proportional to the Hydrogen concentration.

$$r_{FT} = k'_{FT}[H_2] \quad (3-74)$$

3.5.8 Boundary Conditions, Solution Method and Meshing

In order to test the CFD model in predicting a single-phase (gas) flow, air at standard pressure and temperature conditions was fed to the MCR. Two inlet velocities (0.1 m/s and 0.5 m/s) were set in order to see their effect on the flow conditions at the channels inlet. The Reynolds numbers for the air in the inlet pipe for these velocities were 68.5 and 342.3.

A pressure-based solver (solves for momentum and pressure as the main variables) [105]; a phase-coupled simple solver (solves for velocity and pressure at the same time) [105]; and QUICK (Quadratic Upwind Interpolation for Convective Kinetics) interpolation method were employed. The FLUENT CFD solver discretizes the general transport equations to be solved numerically in a fixed number of control volumes (cells). All equations were solved iteratively and simultaneously for each control volume, looking for the value of a particular property at the center of each cell. The QUICK scheme fits a quadratic curve through the cell to find this value by interpolation [94].

The running time for each simulation was between 48-72 hours each in a work station with an Intel ® Core™ i7 CPU, 870 @ 2.93 GHz and 12 GB RAM. The determination of the model convergence was based in the monitored scaled property residuals and mass flux conservation report. A solution was considered converged when the velocity, momentum and species residuals

remained unaltered after several iterations and, when the mass balance report showed conservation between inlet and outlet flow. For the species balance the tolerance was set to 10^{-5} . Prior judging convergence of the solution a time step independent study was carried out by changing the time step of the solution model until the solution remained constant. Additionally, after finding a converged solution, the mesh size was varied to assure that the solution was independent of the grid configuration. Since the channel was considered to operate under isothermal conditions, the energy balance was not solved during this simulation.

The finer mesh, used to calculate the final results, was generated using a hex-dominant method (hexahedral mesh) with a minimum size of 3×10^{-4} m, resulting in 276624 nodes and 234696 elements.

4.0 RESULTS AND DISCUSSION

4.1 RESULTS OF THE ONE-DIMENSIONAL MCR MODEL

The objectives 1-D model for the MCR were to evaluate the possible effect of the different packing shapes and porosities on the CO conversion for F-T synthesis; and to compare the performance of the reactor with that of the CFD model in ANSYS Fluent.

For the first objective, the conversion of the CO was estimated as a function of the reactor length for each packing and the results are presented in Figure 4-1. Based on these plots and the numerical results for the CO molar conversion (calculated based on the molar flows) at the reactor outlet for the spherical catalysts particles with high density, the conversion did not change with the packing porosity.

Also, higher catalyst density yields a faster CO conversion rate as can be observed in Figure 4-1. The CO conversion value for the spherical catalysts was 87.81 %, whereas for the cylindrical (extrudate) catalysts, the values were almost the same (~ 87.80 %) for all porosities used.

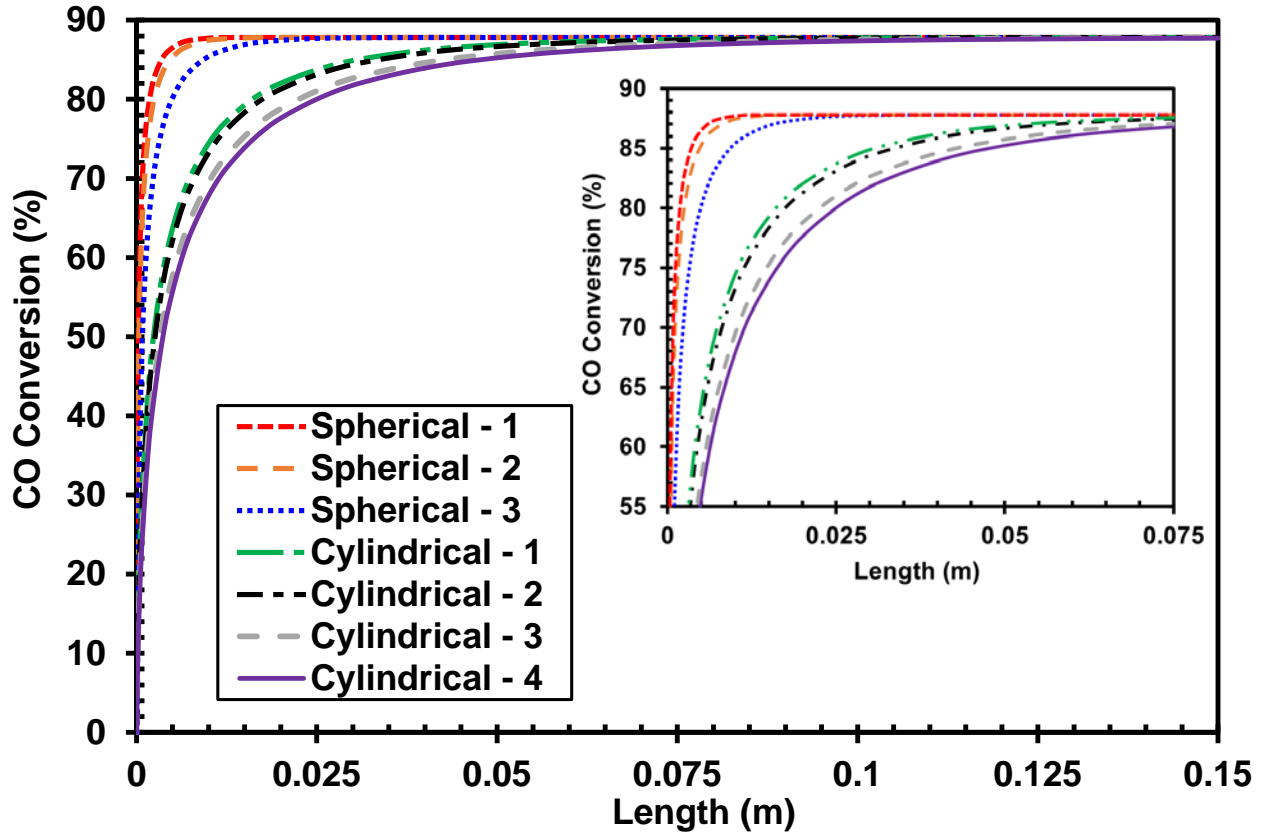


Figure 4-1: Effects of catalyst shape and porosity on the CO Conversion

The pressure drop corresponding to each packing was also calculated as a function of the channels axial length and the results are plotted in Figure 4-2. Unlike the CO conversion, the pressure drop (difference between the pressure at the inlet and that at the outlet of the channel) is greatly affected by the packing shape and porosity, as expected from the pressure drop model equation. The spherical particles with a porosity of 0.260 (Spherical – 1) exhibited the highest pressure drop of 0.92 bar. Since the model does not account for the shape effects of the particles, the pressure drop decreased with increasing porosity and subsequently, the lowest pressure drop was exhibited by the cylindrical particles with the highest porosity of 0.481 (Cylindrical – 4).

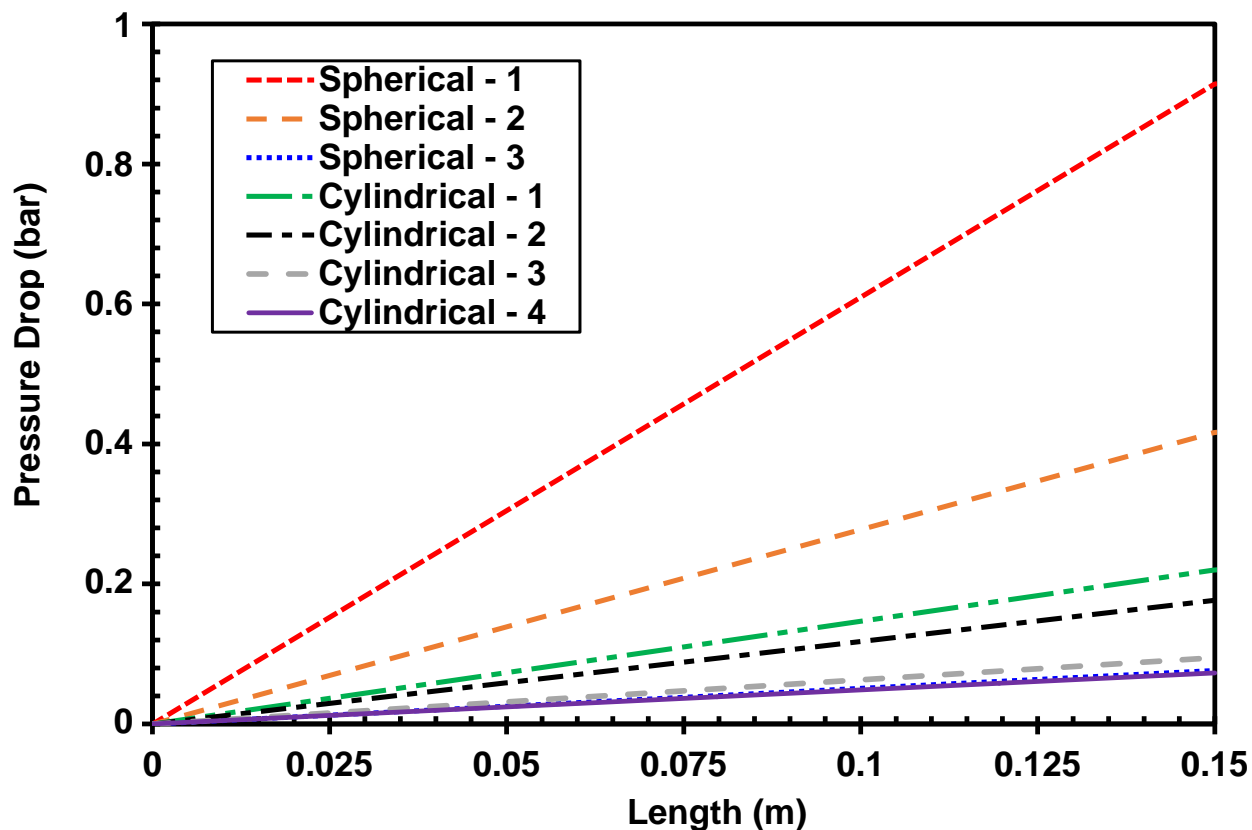


Figure 4-2: Effects of catalyst shape and porosity on the pressure drop

4.2 RESULTS OF THE CFD MCR MODEL SIMULATIONS

4.2.1 Velocity Profile

The boundary condition for the feed gas stream is a superficial inlet velocity of 0.05 m/s. The MCR is packed with extrudate particles with a porosity of 0.375 as given in Table 3-5. The actual inlet velocity, calculated as the ratio between the superficial velocity and packed bed porosity, is 0.133 m/s. Along the channel the average velocity decreases until it reaches a mean actual velocity at the outlet of 0.058 m/s (see Figure 4-3). The laminar flow profile is depicted in Figure 4-4 where

it can be seen that the mean actual velocity profile is at its maximum at the channels center, while it decreases towards zero in the vicinities of the channels walls due to the non-slip velocity condition.

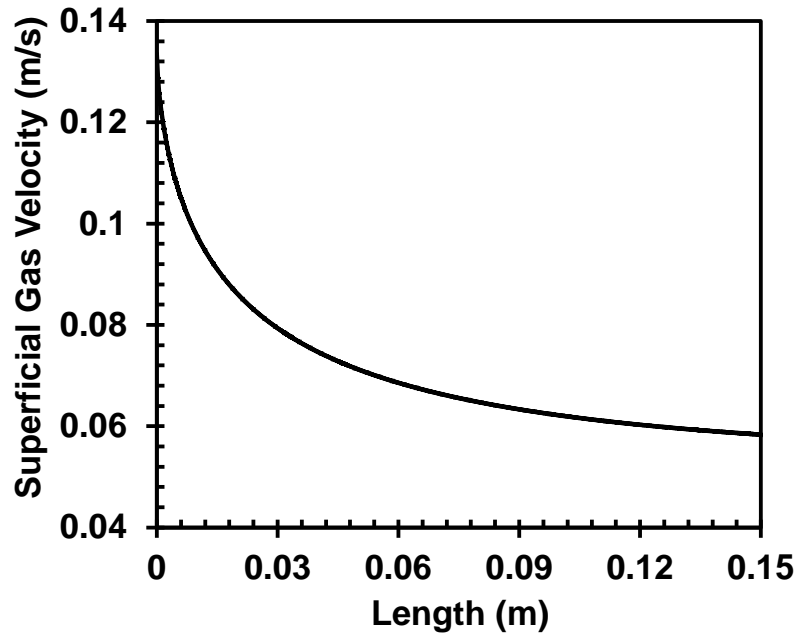


Figure 4-3: Mean velocity along channels length

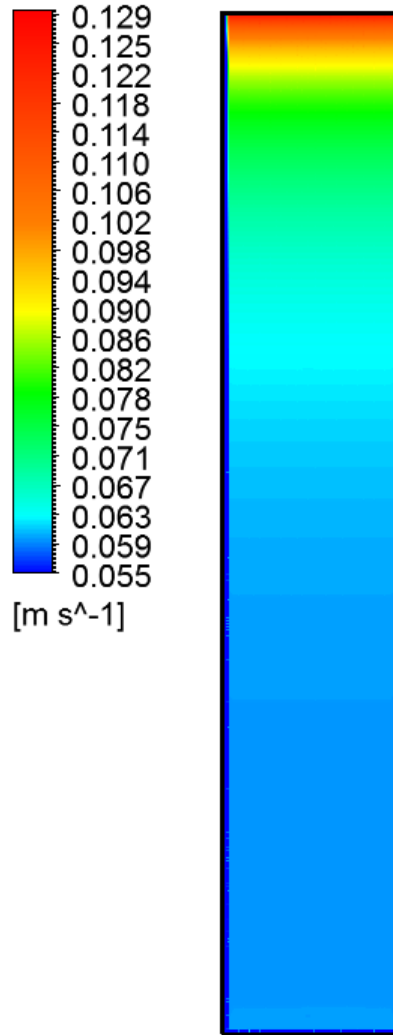


Figure 4-4: Velocity profiles along the channel length

4.2.2 Pressure Drop

When implementing the pressure drop in the CFD model, both viscous and inertial coefficients were entered into the FLUENT model. The pressure drop coefficients were calculated for a particle diameter of $100 \mu\text{m}$ and a porosity of 0.375. With these coefficients the overall pressure drop along the channel is 0.348 bars. The pressure shows a linear decrease along the channels

length similar to results reported in previous investigations for micro-channels [95, 96]. Figure 4-5 shows an example of the pressure drop contours along the channel of 0.15 m length. The pressure scale units are bar.

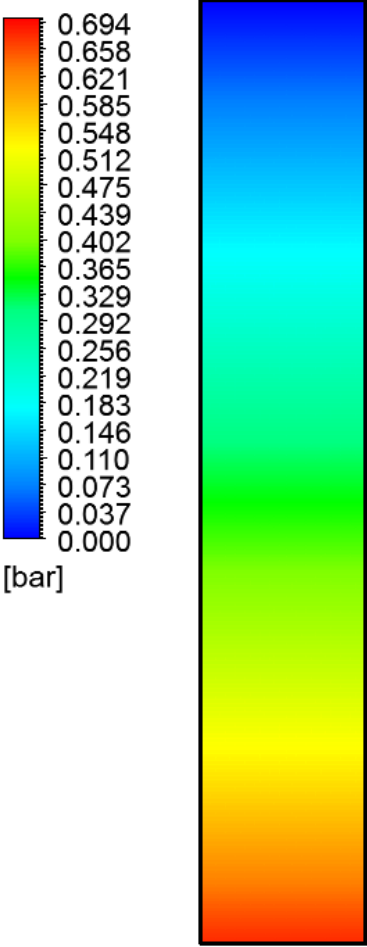


Figure 4-5: Pressure drop contours along the channel length

4.2.3 Conversion, Selectivity and Yield

The percentage CO conversion for the F-T reaction system was calculated in terms on the inlet and outlet molar flows of the CO according to the following equation:

$$X_{CO} = 1 - \frac{F_{CO-final}}{F_{CO-initial}} \times 100 \% \quad (4-1)$$

The syngas ($H_2/CO = 2/1$) inlet flow into a single channel had a density of 6.730 kg/m^3 and a mean molecular weight of 10.96 kg/kmol . The total inlet molar flow for the CO was $7.785 \times 10^{-8} \text{ kmol/s}$. The flow rate at the channels outlet was determined to be $1.369 \times 10^{-8} \text{ kmol/s}$. The CO conversion for the multiple reaction system was 82.41% . Figure 4-6 illustrates the consumption of the CO along the channel length with the decrease in the CO molar flow rate.

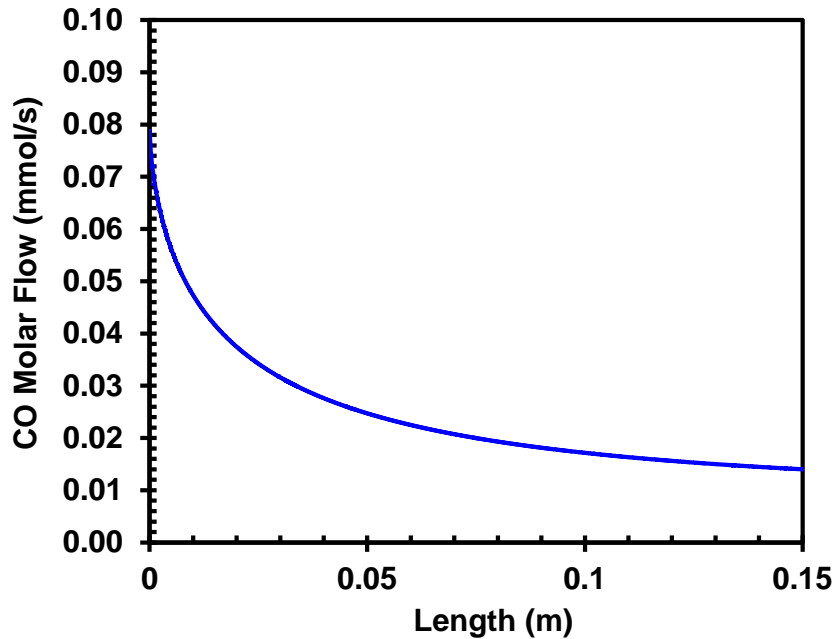


Figure 4-6: Change of CO molar flow with the channel length

In the F-T process, the desired products are typically C₅⁺ hydrocarbons, whereas methane production is an undesirable. The molar flow rates of the different species at the outlet of the channel are listed in Table 4-1. Subsequently, the calculated selectivities are 65.72 % for the C₅⁺ products and 16.42 % for the CH₄. The C₅⁺ yield was also determined to be 54.16%.

Table 4-1: Molar flows at the channel outlet

F-CO	0.0140	mmol/s
F-H₂	0.0101	mmol/s
F-H₂O	0.0648	mmol/s
F-C₁	0.0108	mmol/s
F-C₄	0.0027	mmol/s
F-C₅	0.0022	mmol/s
F-C₁₀	0.0011	mmol/s
F-C₁₄	0.0008	mmol/s
F-C₂₄	0.0004	mmol/s
F-total	0.1068	mmol/s

The C₅⁺ yield was calculated as follows [97]:

$$\gamma_{C_{5+}} = X_{CO}(Sel)_{C_{5+}} \quad (4-2)$$

The effectiveness of the F-T reactions is achieved when the conversion of the reactants is maximized to yield desirable liquid products [4]. Therefore, the scenario with higher reactant conversion is the target. The overall H₂ to CO usage ratio for the alkane reactions can be determined from the stoichiometry, which depends on the carbon number of the product, (2n + 1)/n. The desirable products of the F-T reactions are hydrocarbons with carbon number greater than 5 (gasolines/naphtha, diesel and molten wax). Thus, the selectivity of the F-T reactions is useful in describing the distribution of these products.

4.2.4 Products Distribution

The products distribution was estimated according to the products molar fractions at the outlet of the microchannel. The components with a lower carbon number showed a higher molar fraction than that of the heavier hydrocarbons as can be seen from the hydrocarbons molar flow rates presented in Figure 4-7.

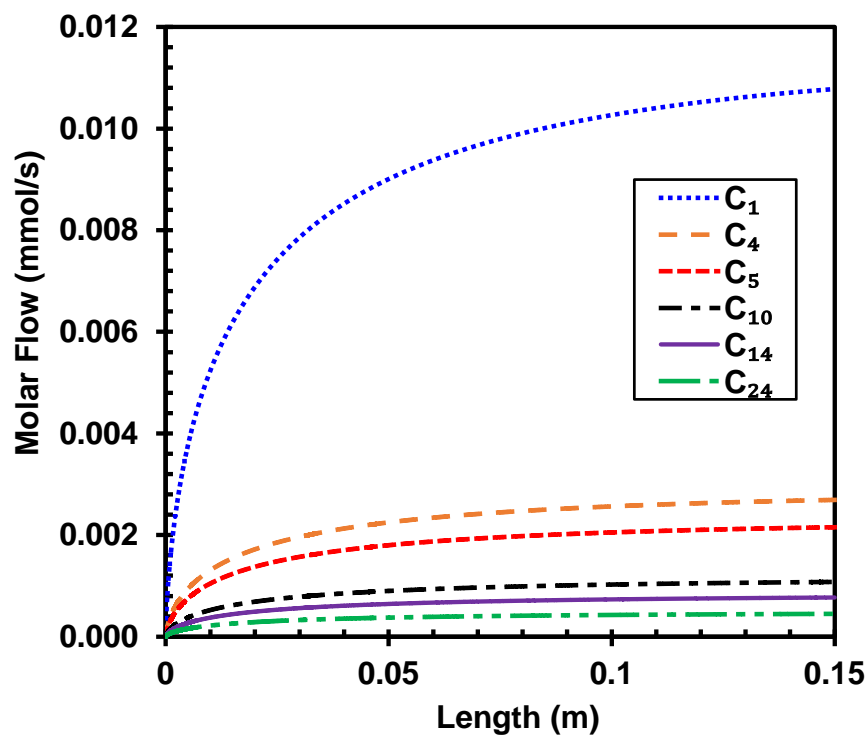


Figure 4-7: Change of the hydrocarbons molar flow rates with the channel length

4.2.5 Heat Transfer Calculations

The CO molar flow rate required for each reactions was calculated based on the reactions stoichiometry. Using the CO consumption and the individual heats of reaction, the heat released in Joules/second (J/s) was estimated as given in Table 4-2. The total heat released by one channel equals the sum of the heat released by all the reactions and totals -12.391 J/s. For the complete MCR model with 50 channels, the total estimated heat release will be - 605.415 J/s.

Table 4-2: CO molar flow requirement and individual heat release per reaction

	Mole flow rate of product (kmol/s)	Heat released per reaction (q) (J/s)
CH ₄	1.0534×10^{-8}	-2.619
C ₄ H ₁₀	1.0532×10^{-8}	-2.177
C ₅ H ₁₂	4.2131×10^{-9}	-1.104
C ₁₀ H ₂₂	1.0541×10^{-8}	-2.165
C ₁₄ H ₃₀	1.0541×10^{-8}	-2.151
C ₂₄ H ₅₀	1.0541×10^{-8}	-2.173
	Total Q	-12.391

The inlet pressure of the cooling fluid should be the same as the reactor operating pressure, which is 25 bar. Under this pressure, the water saturation occurs at 496.937 K with the enthalpy of vaporization $h_{fg} = 1,838.786$ kJ/kg [98]. For the required heat removal, the approximate amount of water needed to cool a single channel is 0.473 ml/min. Under these conditions, the heat transfer coefficient = 4,036.1 W/m²K. Actually this value is reasonable since it was reported by Wang et al. [99] that the heat transfer coefficient in microreactors can be as high as 10,000-35,000 W/m²K.

4.2.6 Mass Transfer Calculations

From the products molar flow rates at the outlet of the reactor, only 3 % is liquid hydrocarbons with carbon number from C₁₀ to C₂₄. If the reactor maintain this percentage of liquid during a continuous operation, the liquid would cover the entire catalyst particles with a film having a thickness of 80 nm.

For a bed porosity of 0.375, the interfacial area where the gas reactants diffuse is equivalent to 37,500 m⁻¹. Under these conditions and with the diffusion coefficients given in Section 3.5.7, the mass transfer coefficients for the H₂ (k_{LS-H2}) and the CO (k_{LS-CO}) are calculated to be 0.569 m/s and 0.215 m/s respectively.

As discussed in Section 3.5.7, comparing the mass transfer coefficient with the pseudo-kinetic reaction rate coefficient, it is possible to assess if the process is controlled by the mass transfer or by the reaction kinetics. **Figure 4-8** shows the pseudo-first order reaction rate as a function of the channel length. Using the results obtained for the reaction rate and the H₂ concentration calculated by the model, a pseudo-first order reaction rate coefficient at every point in the channel length was estimated as presented in **Figure 4-9**.

The reaction rate coefficient k'_{FT} has a maximum value of 4.02x10⁻⁵ m/s at the channel inlet and it decreases along the channel length as a consequence of the H₂ consumption. Even at its maximum point, the reaction rate coefficient is about four orders or magnitude smaller than the mass transfer coefficients calculated for both reactants. Hence, the process is considered to be limited by the kinetics and as such the mass transfer effects could be neglected.

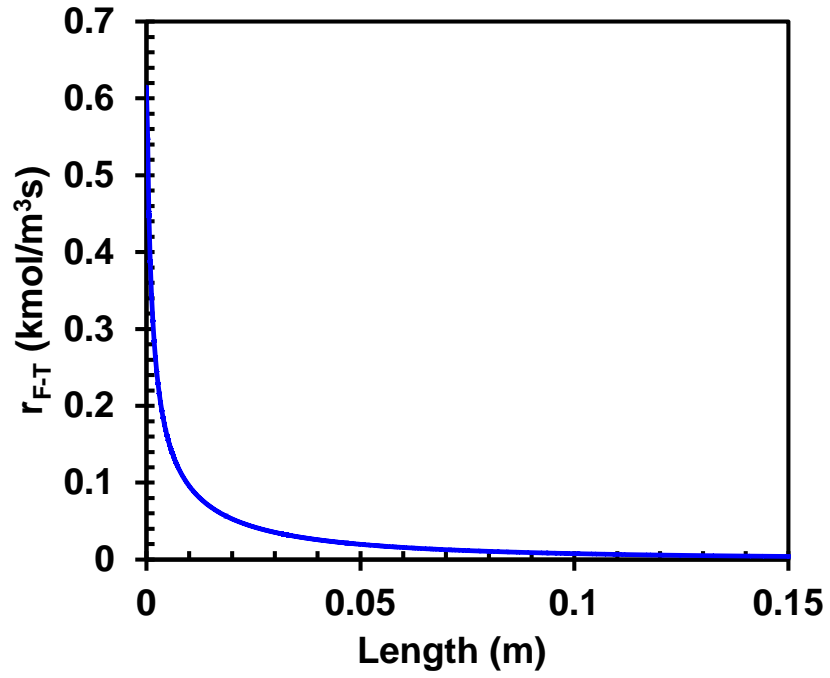


Figure 4-8: Change of the pseudo-first order reaction rate with the channel length

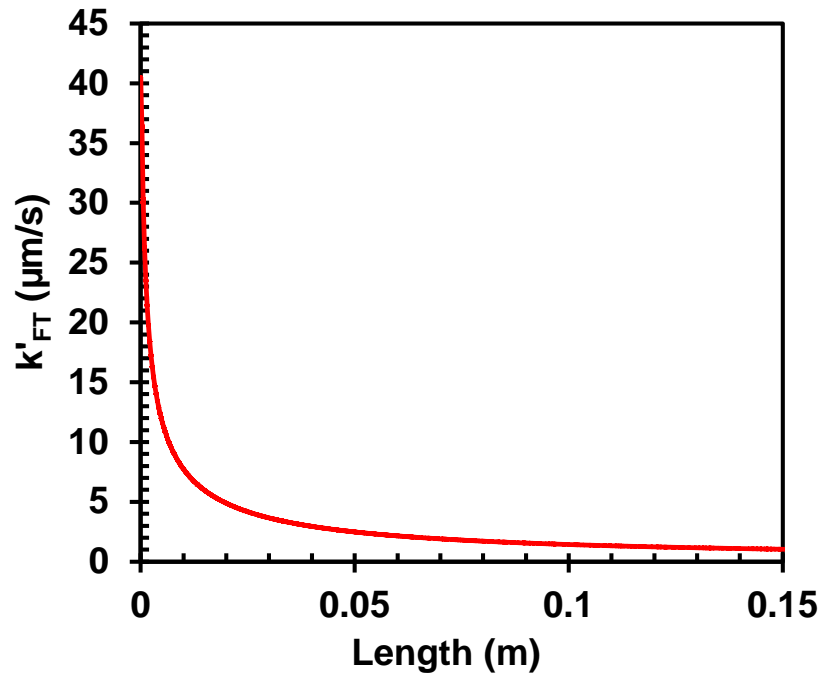


Figure 4-9: Change of the pseudo-first order reaction rate coefficient with the channel length

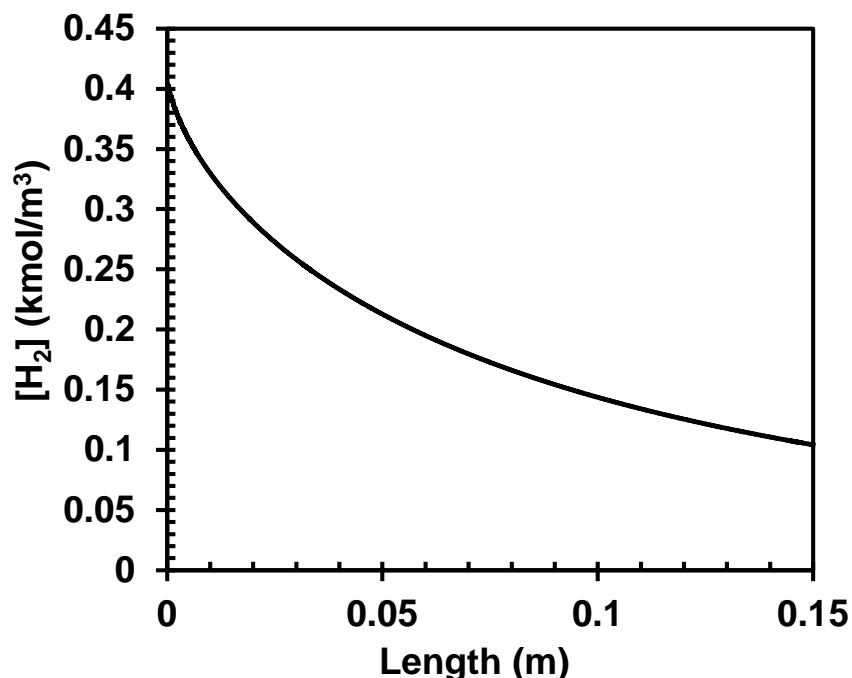


Figure 4-10: Change of H₂ concentration with the channel length

4.3 EFFECTS OF OPERATING CONDITIONS

The overall performance of the MCR for F-T synthesis is controlled by the operating conditions, including inlet gas composition, temperature, pressure, and inlet gas velocity. In order to evaluate the effects of these variables in the proposed MCR in ANSYS, the operating conditions were varied in several simulations and the reactor performance was evaluated based on CO conversion, C₅⁺ selectivity, C₅⁺ yield, maximum kinetic rate, and overall pressure drop. The heat transfer coefficient was also calculated for every case. The following table summarizes the operating condition used in the simulations conducted in this study.

Table 4-3: Simulation parameters considered for different operating conditions

Simulation Set	Case	Variable	Constant conditions
I- Synthesis gas composition	I-1	$H_2/CO = 2.0$	$T = 500 \text{ K}, P = 25 \text{ bar},$ $v_{\text{ginlet}} = 0.05 \text{ m/s}$
	I-2	$H_2/CO = 1.6$	
	I-3	$H_2/CO = 2.5$	
II- Pressure	II-1	$P = 25 \text{ bar}$	$T = 500 \text{ K}, H_2/CO = 2.0,$ $v_{\text{ginlet}} = 0.05 \text{ m/s}$
	II-2	$P = 15 \text{ bar}$	
	II-3	$P = 20 \text{ bar}$	
III- Temperature	III-1	$T = 500 \text{ K}$	$P = 25 \text{ bar}, H_2/CO = 2.0,$ $v_{\text{ginlet}} = 0.05 \text{ m/s}$
	III-2	$T = 483.15 \text{ K}$	
	III-3	$T = 523.15 \text{ K}$	
IV- Gas Inlet velocity	IV-1	$v_{\text{ginlet}} = 0.05 \text{ m/s}$	$P = 25 \text{ bar}, H_2/CO = 2.0,$ $T = 500 \text{ K}$
	IV-2	$v_{\text{ginlet}} = 0.01 \text{ m/s}$	
	IV-3	$v_{\text{ginlet}} = 0.03 \text{ m/s}$	
	IV-4	$v_{\text{ginlet}} = 0.1 \text{ m/s}$	

4.3.1 Effect of H_2/CO Feed Ratio on the MCR Performance

Figure 4-11 through Figure 4-13, illustrate the effect of H_2/CO feed ratio on the CO molar conversion, C_5^+ selectivity and C_5^+ products yield. As can be seen in these figures, increasing the H_2/CO ratio at the reactor inlet from 1.6 to 2.5, results in an increase of the CO conversion from 71.8 to 91.99 %. This behavior is in agreement with other investigations for F-T synthesis in MCRs [30, 31, 33, 55, 100, 101]. Similarly, the C_5^+ products yield increased with increasing H_2/CO ratio in the inlet gas as the yield was 45.55 % for the lowest H_2/CO (1.6) and 60.63 % for the highest value (2.5). On the other hand, the C_5^+ selectivity remained constant at 65.72 % at different H_2/CO ratios, which could be due to the fact that the chain probability growth values were fixed for the conditions investigated.

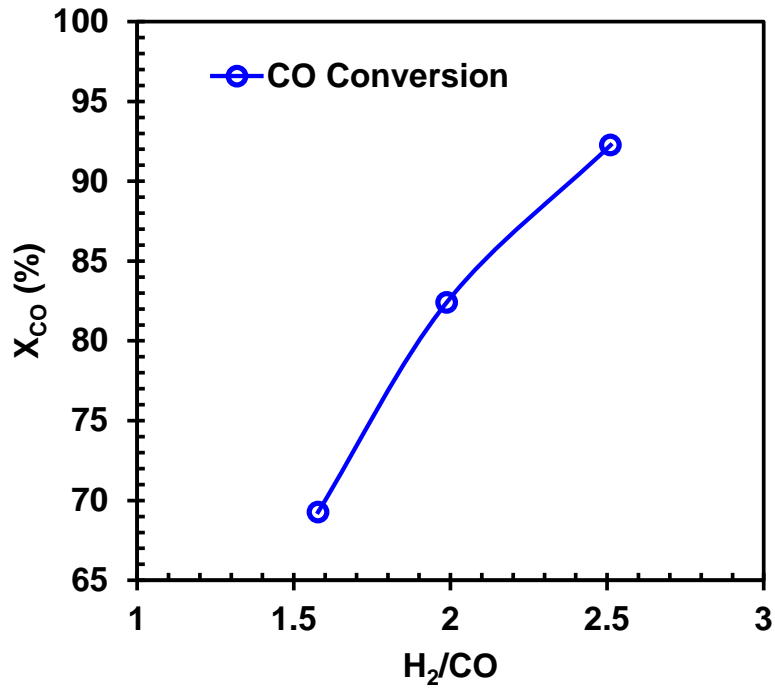


Figure 4-11: Effect of H₂/CO ratio on CO conversion

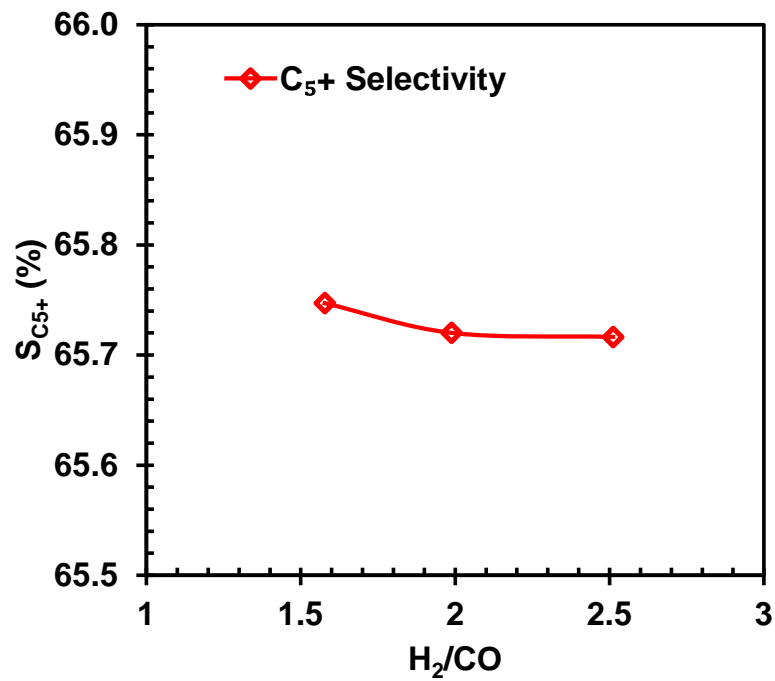


Figure 4-12: Effect of H₂/CO ratio on C₅₊ selectivity

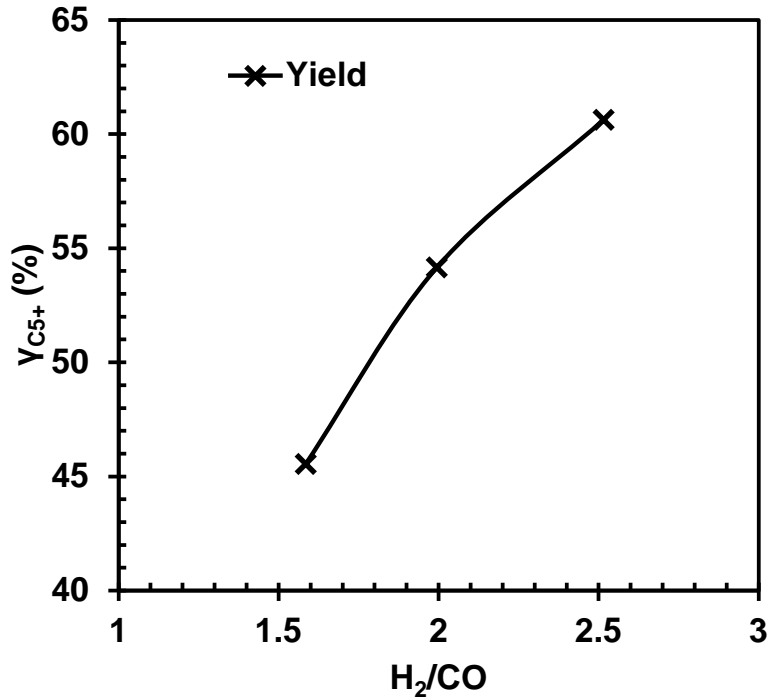


Figure 4-13: Effect of H₂/CO ratio on C₅₊ Yield

Figure 4-14 depicts the effects of H₂/CO ratio on the maximum kinetic rate and the overall pressure drop along the channel. As can be observed in this figure, increasing H₂/CO feed ratio slightly increases the maximum kinetic rate and the overall pressure drop. The increase of the kinetic reaction rate for the F-T reactions is proportional to the hydrogen partial pressure, whereas, the increase of pressure drop is due to increased formation of liquid products with increasing H₂ content in the feed. The effect of more or less liquid production cannot be seen for a fixed product distribution, however, the model accounts for the change of the H₂ feed content in terms of reaction rate and the effect of an increased hydrocarbons production, which results in a slight increase of the pressure drop.

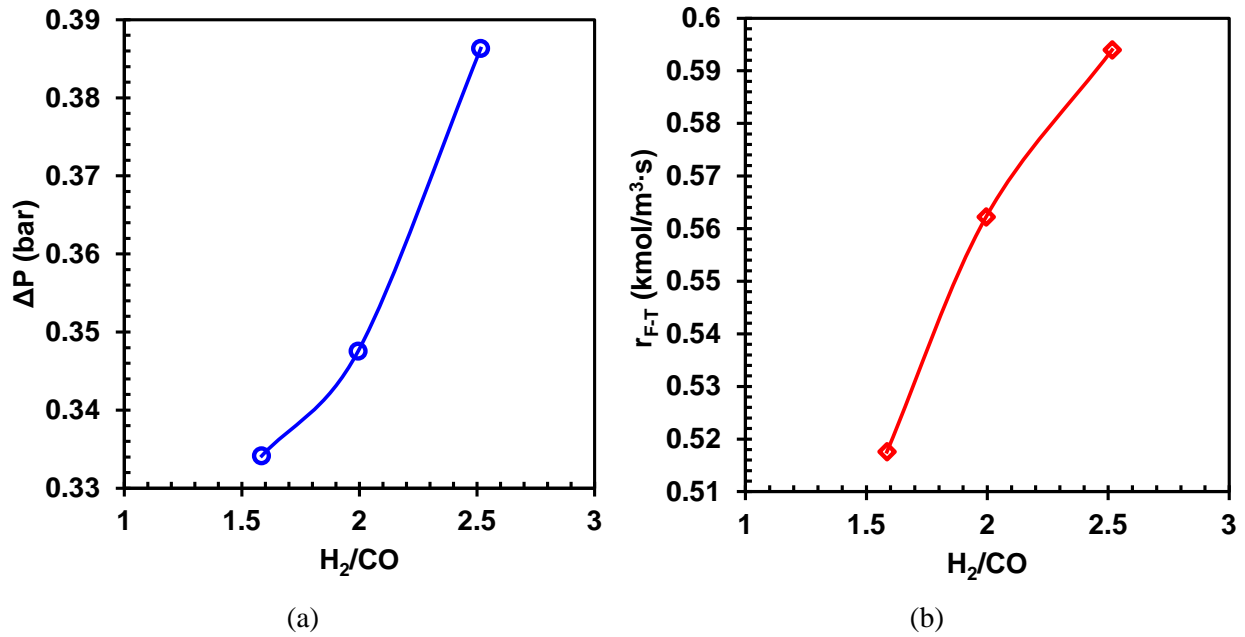


Figure 4-14: Effect of H₂/CO ratio on the (a) pressure drop and (b) maximum kinetic rate

The heat released in the microchannel depends on the molar flow of CO consumed and the individual heats of reactions. Since the H₂-rich gas leads to a higher CO conversion, it also affects the overall heat transfer coefficients as its calculated values ranged from 3,473.5 to 4,492.1 W/m²K. Table 4-4 summarizes the results obtained for this set of simulations.

Table 4-4: Effect of varying H₂/CO ratio on MCR performance

H ₂ /CO	X _{CO} (%)	S _{C5+} (%)	Y _{C5+} (%)	U (W/m ² K)	ΔP (bar)	r _{FT} (kmol/m ³ s)
1.60	69.28	65.75	45.55	3,473.5	0.334	0.518
2.00	82.41	65.72	54.16	4,036.1	0.348	0.562
2.50	92.26	65.72	60.63	4,492.1	0.386	0.594

4.3.2 Effect of pressure on the MCR performance

It was reported in multiple studies that increasing pressure promotes CO conversion [28, 31, 59]. This is expected for the F-T synthesis since the equilibrium reactions for the paraffins and olefins formation are favored with increasing pressure according to Le Chatelier's principle [102]. Also, the formation of the heavier hydrocarbons is expected to occur at higher pressures. Le Chatelier's principle states that if the equilibrium of a chemical reaction is altered by changing its temperature, pressure or concentration, the system will oppose the changing conditions while trying to reach a new equilibrium state.

Figure 4-15 through Figure 4-17 illustrate the effects of increasing pressure from 15 to 25 bar on the CO conversion, C_5^+ selectivity and C_{5+} products yield, respectively. As can be seen in these figures the pressure effect on CO conversion is negligible, which was not expected. It should be noted, however, that fixing the hydrocarbons chain length for the products to be formed during the F-T reactions appeared to limit the ability of the CFD model to predict the pressure effect.

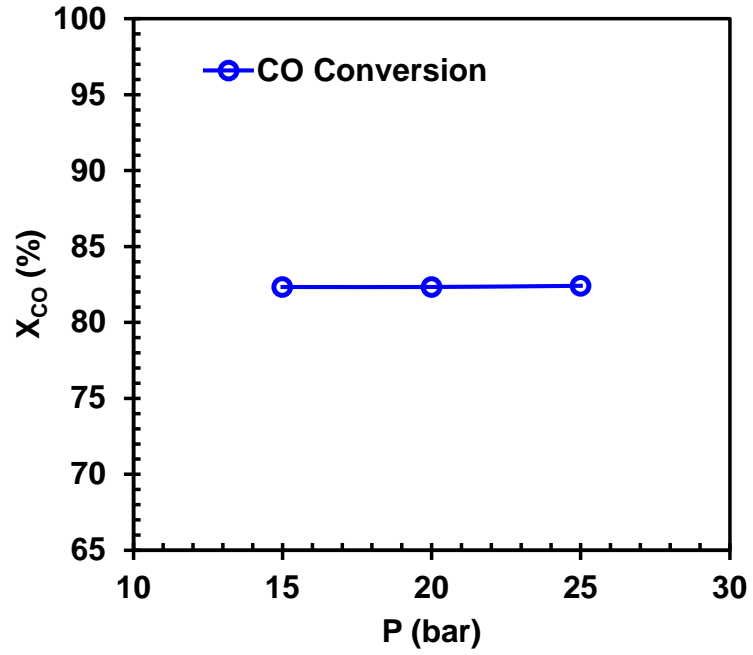


Figure 4-15: Effect of pressure on CO conversion

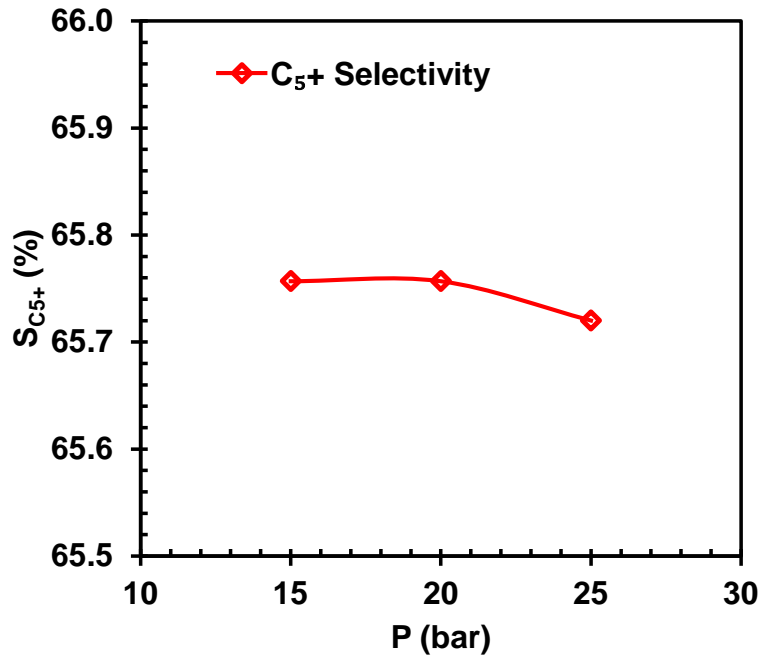


Figure 4-16: Effect of pressure on C₅⁺ selectivity

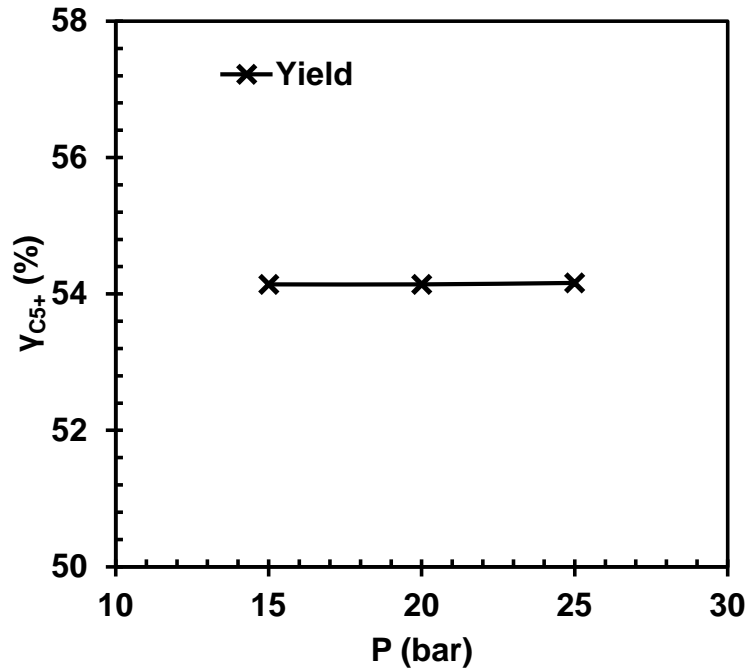


Figure 4-17: Effect of pressure on C_5^+ yield

Figure 4-18 (a) shows the maximum kinetic rate increases with the total pressure. This is expected because the kinetic reaction rate for the F-T synthesis is proportional to the partial pressure of the inlet gas. Increasing the pressure from 15 bar to 25 bar, led to increasing the maximum kinetic rate from 0.364 to 0.562 $\text{kmol/m}^3\text{s}$. In addition, Figure 4-18 (b) shows that the pressure drop along the channel remains between 0.345 and 0.365 bar with changing the total inlet pressure from 15 to 25 bar.

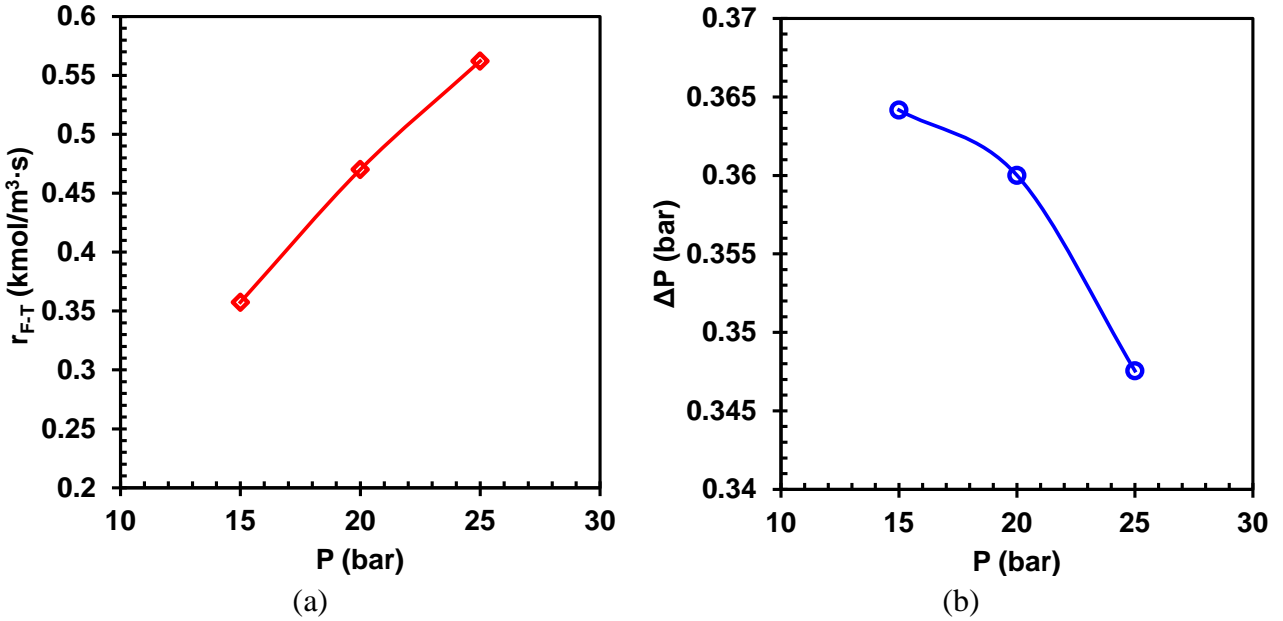


Figure 4-18: Effect of pressure on (a) the pressure drop and (b) the maximum kinetic rate

The increase of system pressure increases the synthesis gas density at the inlet of the channel and subsequently increases the mass flow rate at a fixed superficial inlet gas velocity of 0.05 m/s. As a consequence, despite having no effect on the conversion, the amount of CO consumed increases at high pressures. The CO molar flow rates also affect the heat released since it is expressed per mol/s of CO consumed. Accordingly, the heat transfer coefficient at lower pressure value is 2,492.1 W/m²K, while at higher pressure it is 4,036.1 W/m²K. Table 4-5 summarizes the results obtained for this set of simulations.

Table 4-5: Effect of pressure on MCR performance

P (bar)	X _{CO} (%)	S _{C5+} (%)	Y _{C5+} (%)	U (W/m ² K)	ΔP (bar)	r_{FT} (kmol/m ³ s)
15.00	82.33	65.76	54.14	2,492.1	0.364	0.357
20.00	82.33	65.76	54.14	3,423.9	0.360	0.470
25.00	82.41	65.72	54.16	4,036.1	0.348	0.562

4.3.3 Effect of temperature on the MCR performance

Various authors reported that increasing temperature in MCRs during F-T synthesis promotes CO conversion [31, 33, 59]. This behavior is also found in this study as shown in Figure 4-19 through Figure 4-21. When increasing the temperature from 483.15 to 523.15 K, the CO conversion increases from 74.58 % to 87.45 %. The C_5^+ selectivity varies slightly between 63.36 % and 66.09 %, whereas the yield increases from 49.29 % to 55.41%.

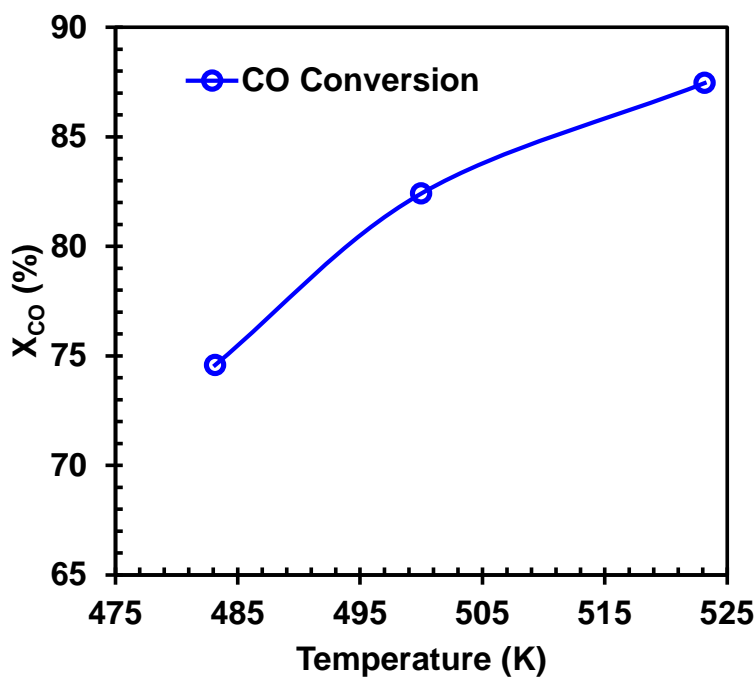


Figure 4-19: Effect of temperature on CO conversion

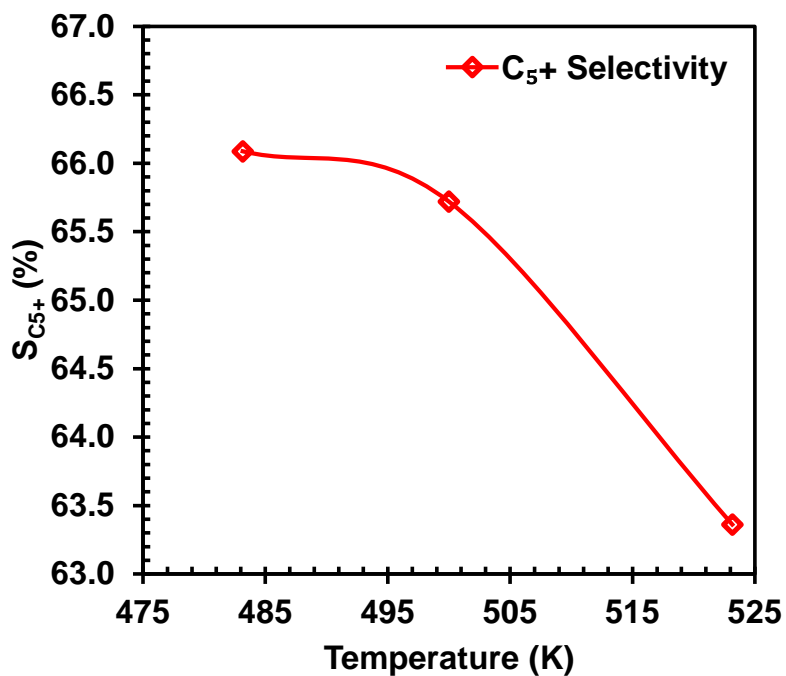


Figure 4-20: Effect of temperature on C₅⁺ selectivity

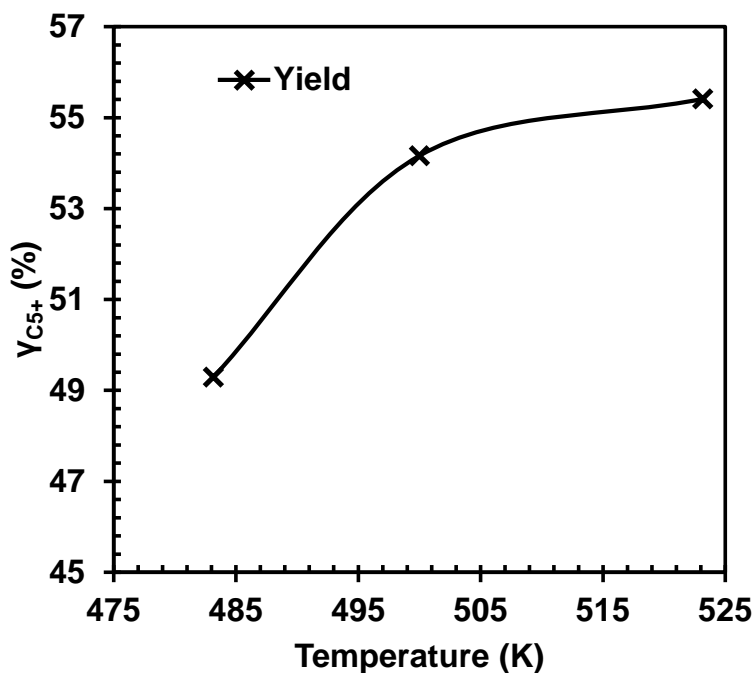


Figure 4-21: Effect of temperature on C₅⁺ yield

Since the reaction rate is a function of temperature, at higher temperatures, higher reaction rates are expected as shown in Figure 4-22 (a). The maximum reaction rates achieved inside the channel is $0.353 \text{ kmol/m}^3\text{s}$ at 483.15 K and $1.044 \text{ kmol/m}^3\text{s}$ at 523.15 K . Moreover, Figure 4-22 (b) shows that the pressure drop decreases with increasing temperature. This is due to the fact that higher temperatures favor the endothermic termination reactions in F-T synthesis, thus promoting the desorption of the surface species leading to the formation of shorter hydrocarbon chains [4]. Moreover, the pressure drop decreases with increasing temperature since it is proportional to the density. It should be remembered that the density of the reactants and products mixture decreases with increasing temperature.

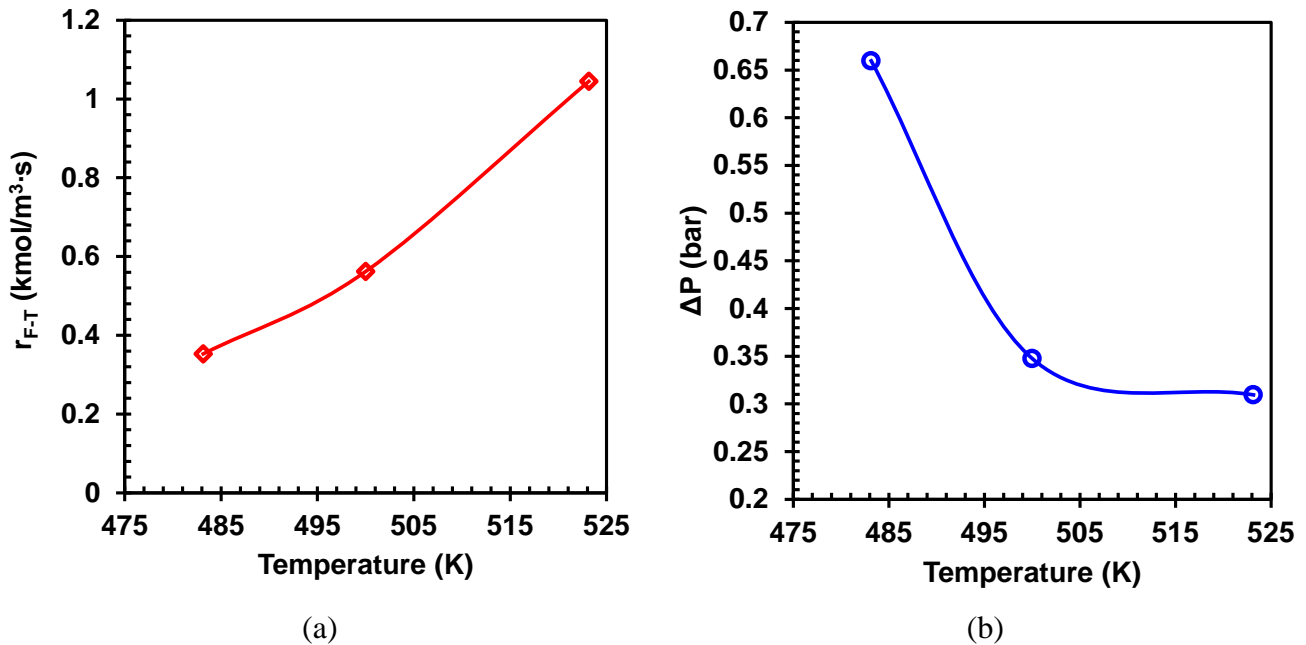


Figure 4-22: Effect of temperature on (a) the pressure drop and (b) the maximum kinetic rate

Similar to the simulations discussed above, the heat transfer coefficients increases with increasing temperature. Actually, the calculated heat transfer coefficient is 3,668.0 W/m²K for 483.15 and is 4,192.18 W/m²K for 523.15 K. Table 4-6 summarizes the results obtained for this set of simulations.

Table 4-6: Effect of temperature on MCR performance

T (K)	X_{CO} (%)	S_{C₅⁺} (%)	Y_{C₅⁺} (%)	U(w/m²K)	ΔP (bar)	r_{FT} (Kmol/m³s)
483.15	74.58	66.09	49.29	3,667.99	0.660	0.353
500.00	82.41	65.72	54.16	4,036.10	0.348	0.562
523.15	87.45	63.36	55.41	4,192.18	0.309	1.044

4.3.4 Effect of inlet gas velocity on reactor performance

Increasing the syngas inlet velocity decreases its residence time inside the channel and as a consequence, the short reaction time results in a decrease of CO conversion and the C₅⁺ products yield as shown in Figure 4-23 through Figure 4-25, respectively. In this set of simulations, the superficial gas velocity at the channel inlet was increased from 0.01 m/s to 0.1 m/s and consequently the CO conversion decreased from 86.98 % to 74.35% and the C₅⁺ products yield decreased from 58.68% to 48.26.

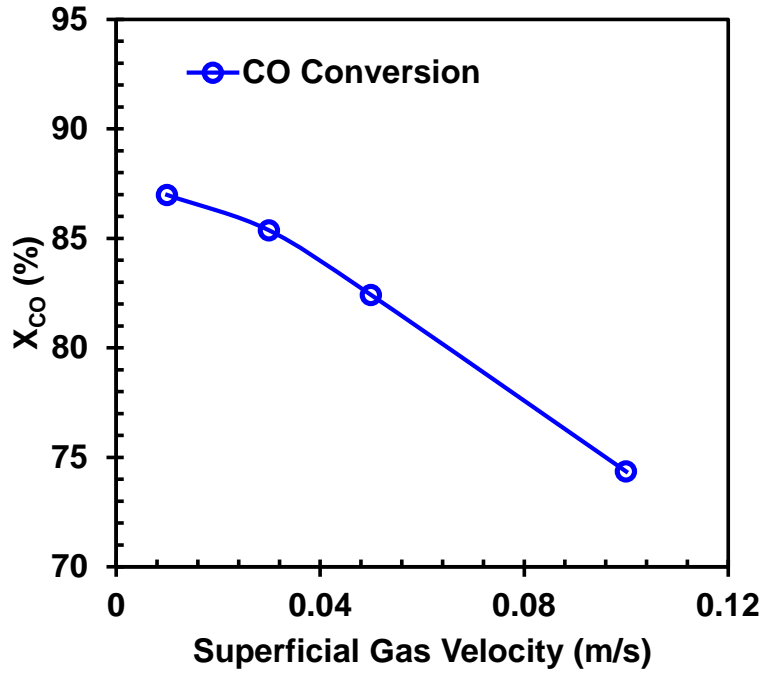


Figure 4-23: Effect of superficial inlet gas velocity on CO conversion

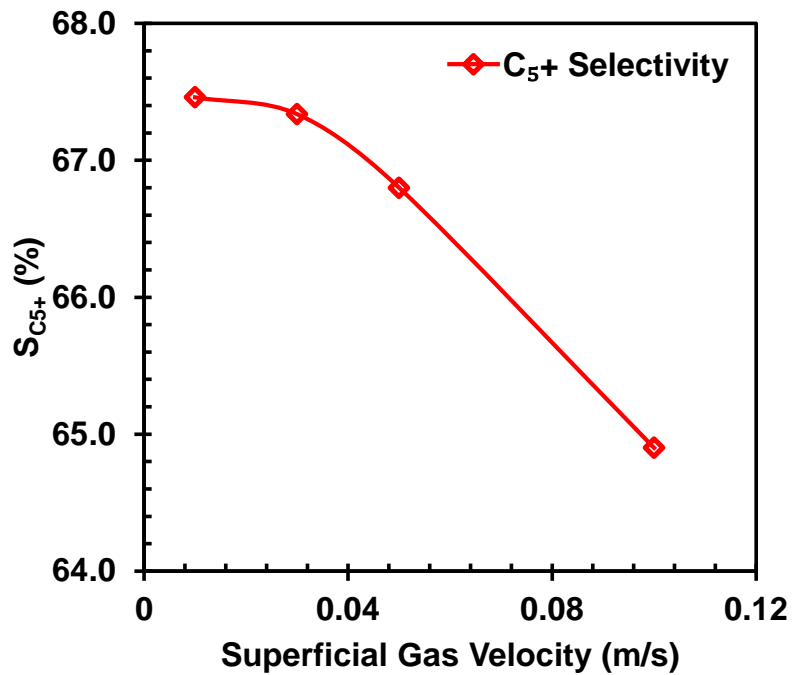


Figure 4-24: Effect of superficial inlet gas velocity on C₅⁺ selectivity

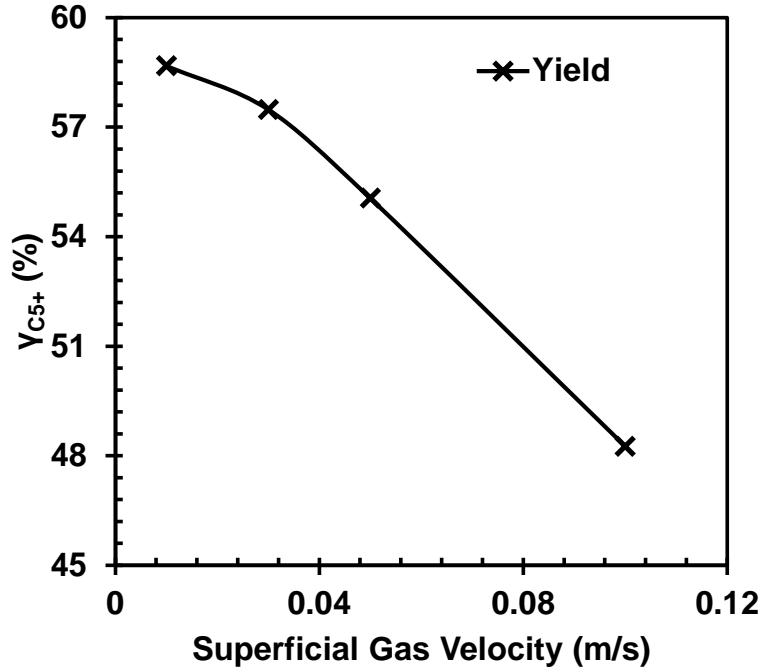


Figure 4-25: Effect of superficial inlet gas velocity on C_5^+ yield

The pressure drop appears to increase linearly with the superficial gas velocity as can be observed in Figure 4-26 (a). According to the pressure drop model, if the viscous and inertial terms of the equation are considered, the pressure drop increase should not be a linear function with the gas velocity. Thus, the behavior shown in Figure 4-26 (a) indicates that the contribution of the inertial forces to the pressure drop is negligible within this range of the inlet gas velocity used.

On the other hand, since the reaction rate is dependent on the amount of reactants flowing through the reactor, increasing the inlet gas velocity from 0.01 to 0.1 m/s led to the increase of the maximum kinetic rate from 0.196 kmol/m³s to 0.726 kmol/m³s as shown in Figure 4-26 (b).

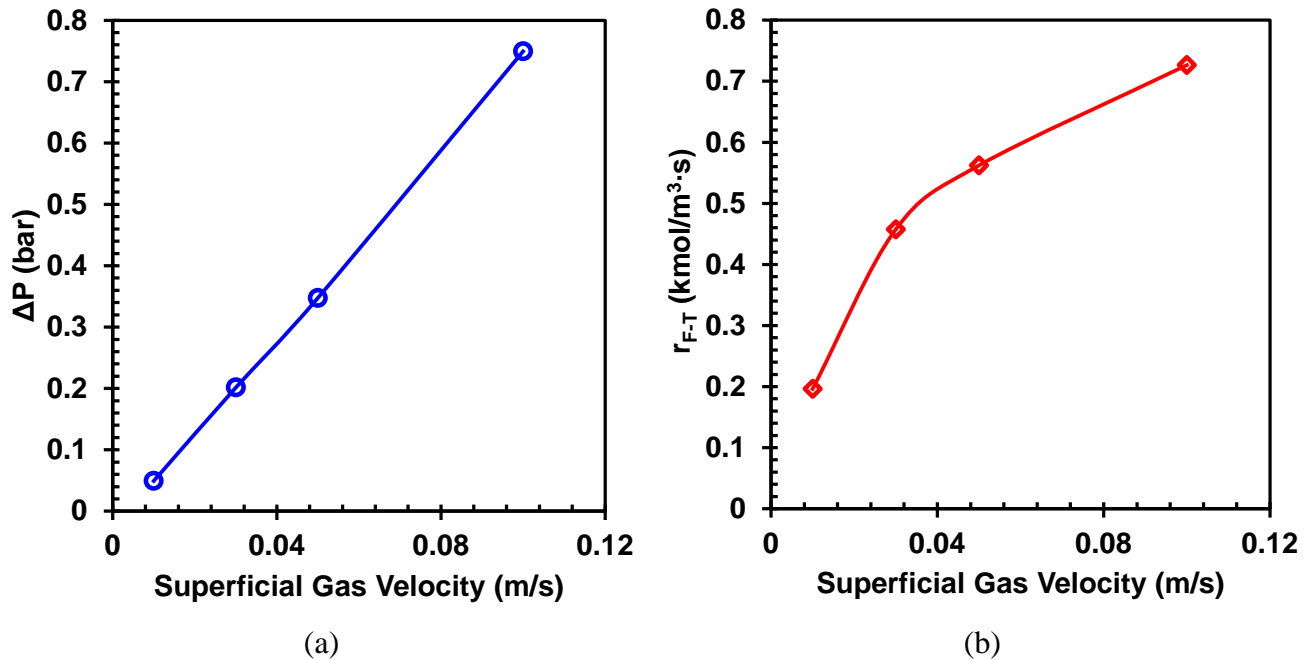


Figure 4-26: Effect of superficial inlet gas velocity on (a) the pressure drop and (b) the maximum kinetic rate

Even though the CO conversion decreases with increasing the inlet gas velocity, the amount of CO consumed was much higher at high superficial velocities due to the increased mass flow rates. In addition, the heat transfer coefficient appear to increase from 959.3 W/m²K to 7,512.6 W/m²K with increasing the inlet gas velocity from 0.01 to 0.1 m/s. Table 4-7 summarizes the results obtained for this set of simulations.

Table 4-7: Effect of superficial gas velocity on the MCR performance

V_s (m/s)	X_{CO} (%)	S_{C5+} (%)	Y_{C5+} (%)	U (W/m ² K)	ΔP (bar)	$r_{F,T}$ (kmol/m ³ s)
0.01	86.99	67.46	58.68	959.29	0.049	0.196
0.03	85.36	67.34	57.48	2480.77	0.201	0.457
0.05	82.41	66.80	55.05	4,036.10	0.348	0.562
0.10	75.22	64.90	48.26	7,512.58	0.749	0.726

4.4 FLOW DISTRIBUTION SIMULATION

The purpose of the flow distribution simulations was to better understand the gas distribution profile at the inlet of the MCR considering a single feed line for the reactants, and also to study the effect of the variation of this feed rate on the distribution of the gas flow at the inlet of the reactor. In this analysis, two flow simulations were evaluated: (1) considering a free pathway for the gas flow with fluid inlet velocities of 0.1 m/s and 0.5 m/s; and (2) considering a fluid flow distributor at the reactors inlet and a feed rate of 0.5 m/s. The convergence criteria for the simulations were: (1) the steady behavior of the continuity equations, (2) the velocity and turbulence parameter residuals, and (3) the conservation of mass and momentum equations. The simulations were performed in two different meshes in order to insure that the results are independence of the mesh configuration.

In the first simulation, the flow distribution profile showed (i) high velocity values at the center of the reactor, including the inlet zone of the channels located in this area, (ii) the formation of vortices at the sides of this high velocity area, and (iii) lower velocity values closer to the reactor's lateral walls. This behavior is illustrated in Figure 4-27 and Figure 4-28, which present the velocity contour and velocity vector profiles at the gas inlet velocities of 0.1 m/s and 0.5 m/s, respectively. As can be seen in these figures, increasing the inlet gas velocity did not have a significant effect on enhancing the flow distribution between the reactor channels, and a similar flow profile, marked by increased velocity at the center and strong recirculation vortices above the channel inlets, is exhibited.

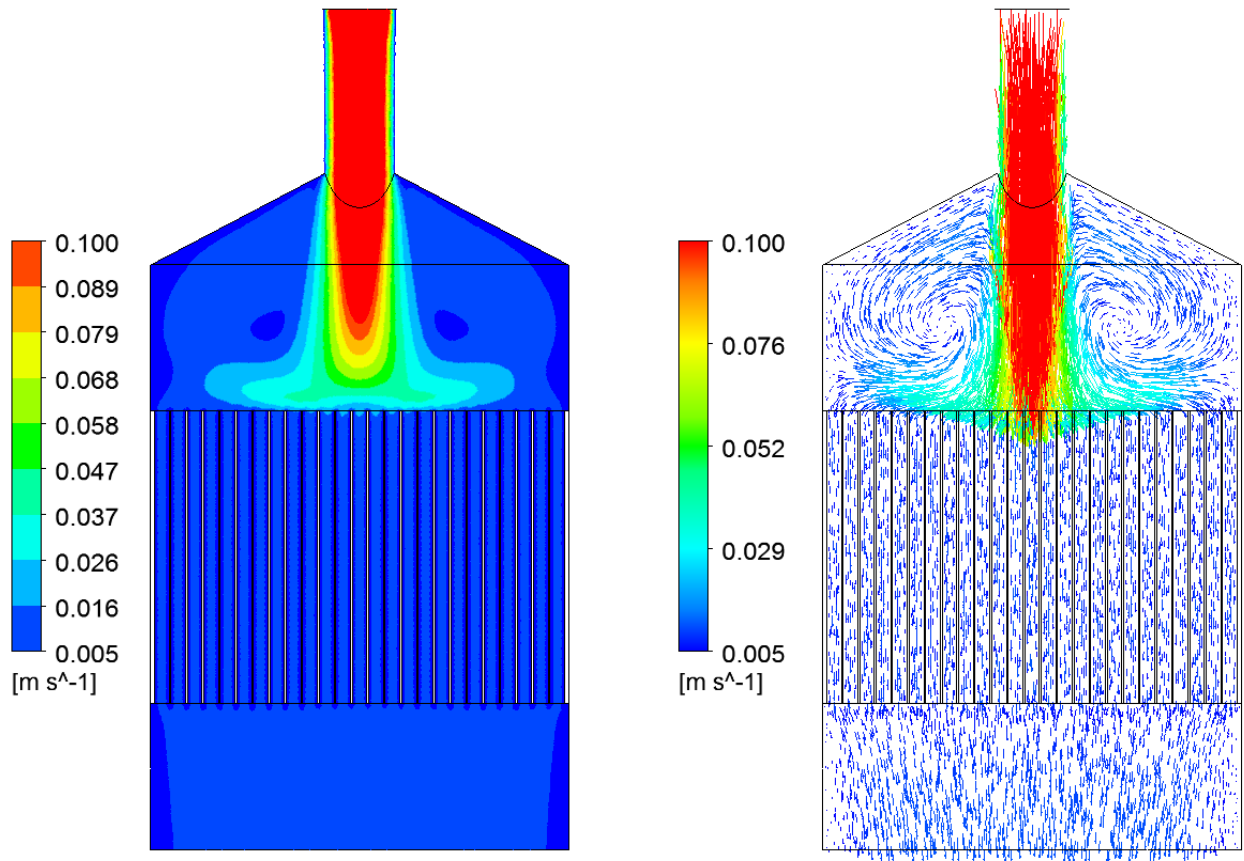


Figure 4-27: Velocity contour and vector profiles of the flow distribution with ($V_{\text{inlet}} = 0.1 \text{ m/s}$)

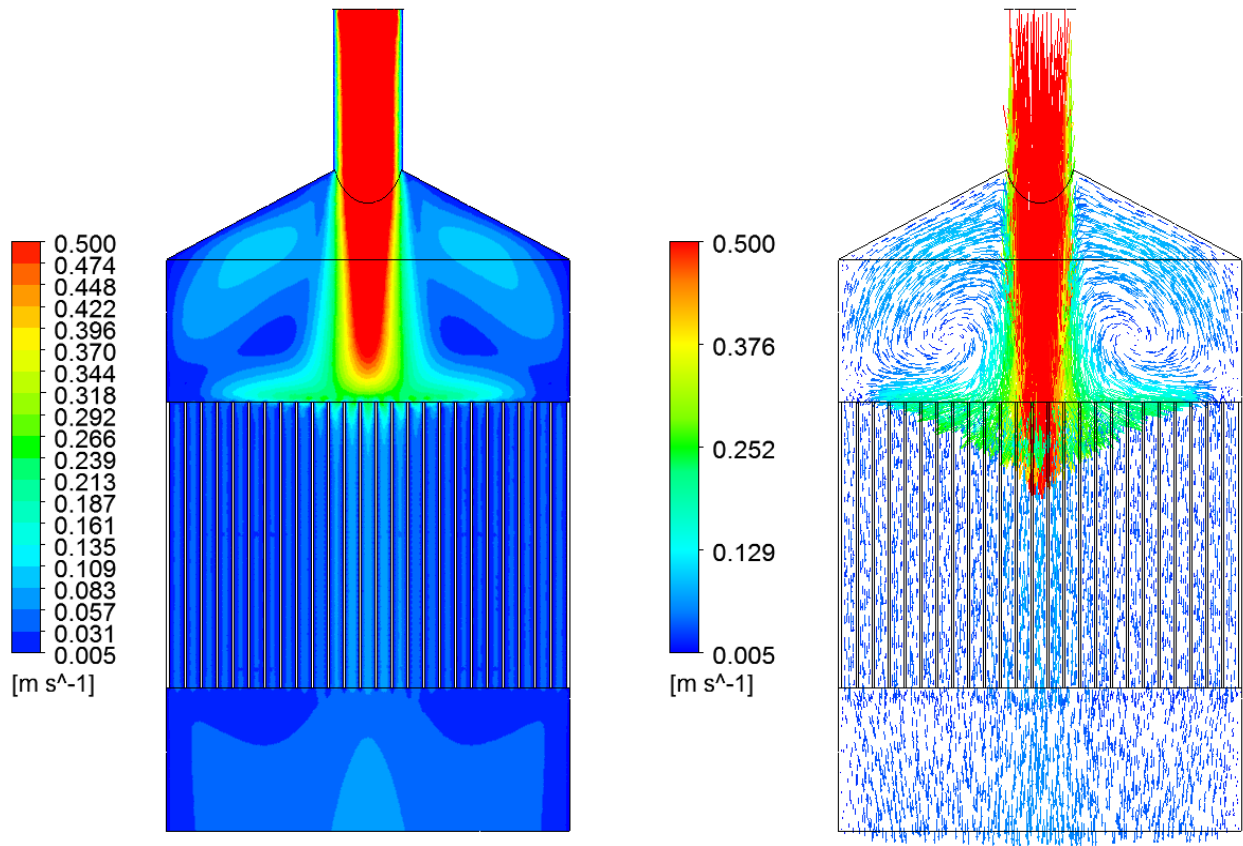


Figure 4-28: Velocity contour and vector profiles of the flow distribution with ($V_{\text{inlet}} = 0.5 \text{ m/s}$)

Moreover, Figure 4-29 shows the velocity contours at the channels inlet and as can be seen, the outer channels have velocities close to 0.008 m/s , while the center channels have velocities close to 0.02 m/s , when the gas is 0.1 m/s . Similarly, the velocities at the entrance of the channels varies from 0.025 m/s at the outer channels and 0.25 m/s at the center channels, when the gas is fed at 0.5 m/s .

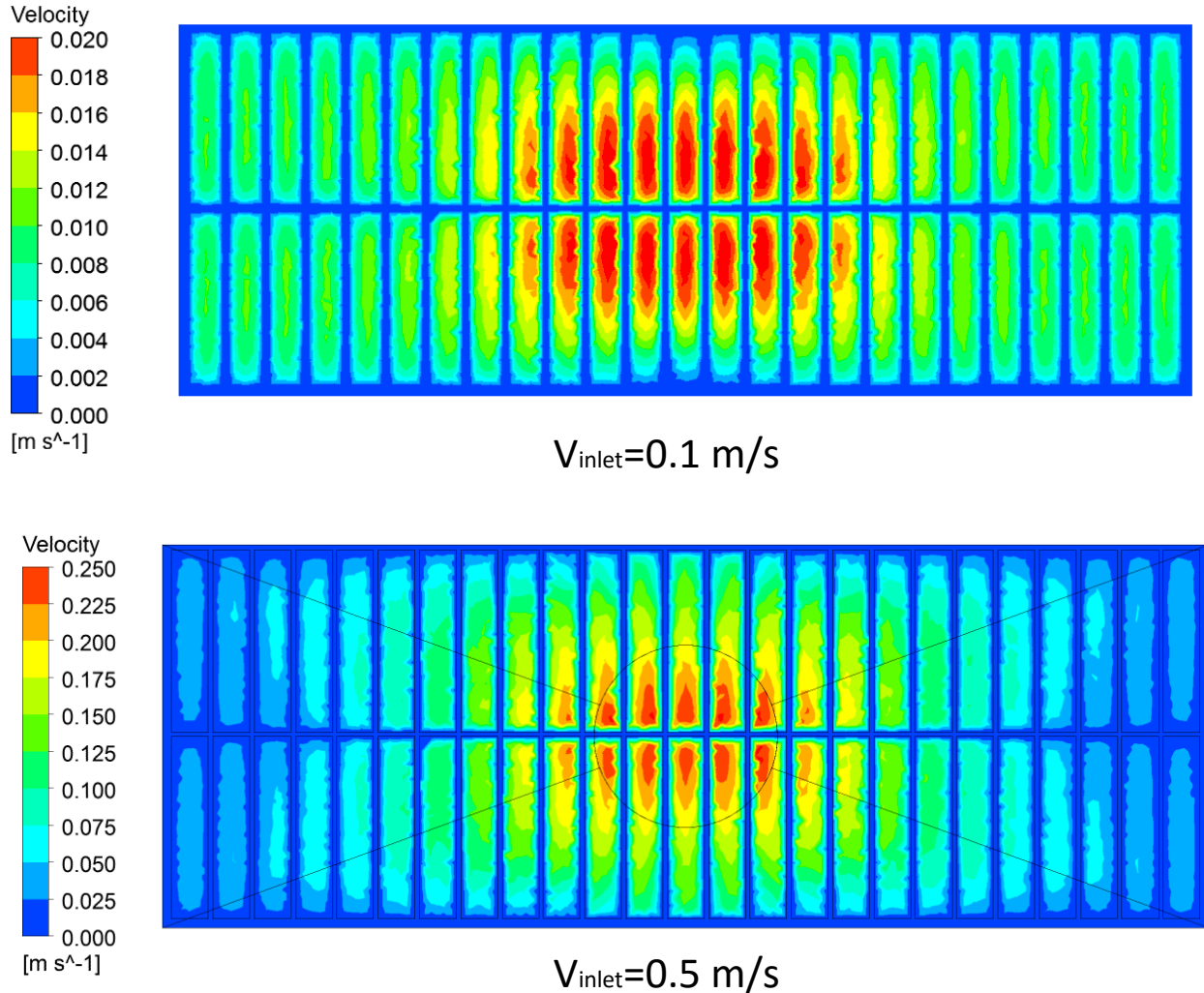


Figure 4-29: Velocity contours at the micro channel's inlet

For the reactor to have an overall homogenous conversion per channel, the reactants flow needs to be equally distributed at the channels inlets. A more homogenous flow distribution is achieved when incorporating a set of solid spheres, which act as a flow distributor for the gas feed. Figure 4-30 depicts the velocity profiles at the MCR entrance with the flow distributor and as can be observed the velocity contours show that the spheres distribute the gas flow, eliminating the high velocities at the center channels and leading to a homogeneous velocity profile. Thus, in contrast to the previous case where the gas had a free pathway to flow, when using a flow

distributor, all microchannels present similar inlet velocities independently of their position in the MCR. In addition, Figure 4-31 shows that when the gas is fed at 0.5 m/s, the average velocity at the channels inlet is 0.033 m/s. Due to the nature of the flow distributor (solid spheres) and the rectangular geometry of the reactor, however, the space between the reactor walls and the spheres allows for higher velocities in some of the outer parts of the channels.

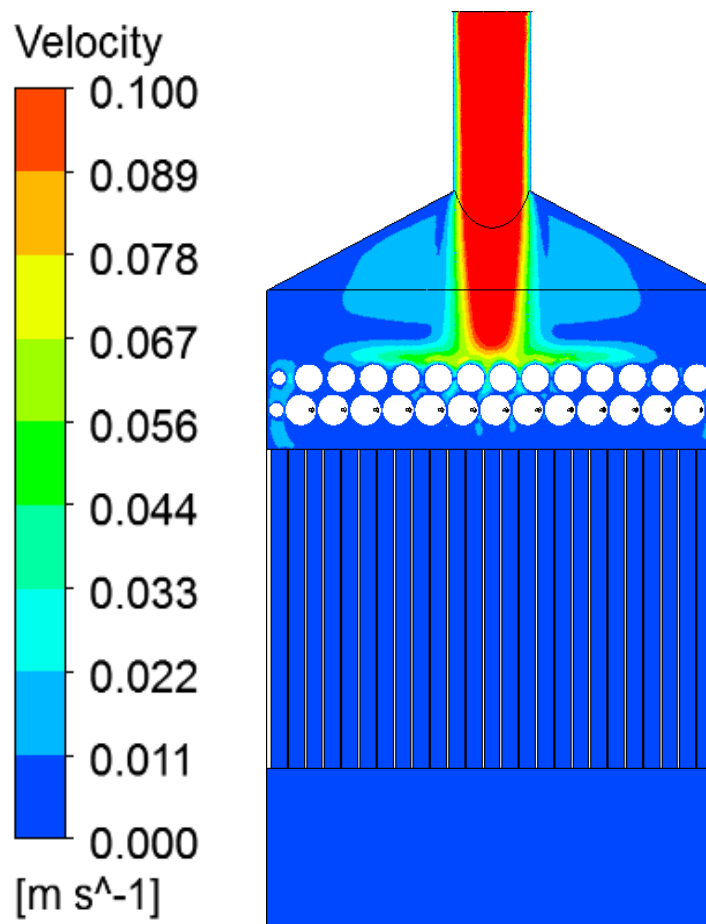


Figure 4-30: Velocity contours with flow distributor ($V_{\text{inlet}}=0.5$ m/s)
(With spheres as flow distributor)

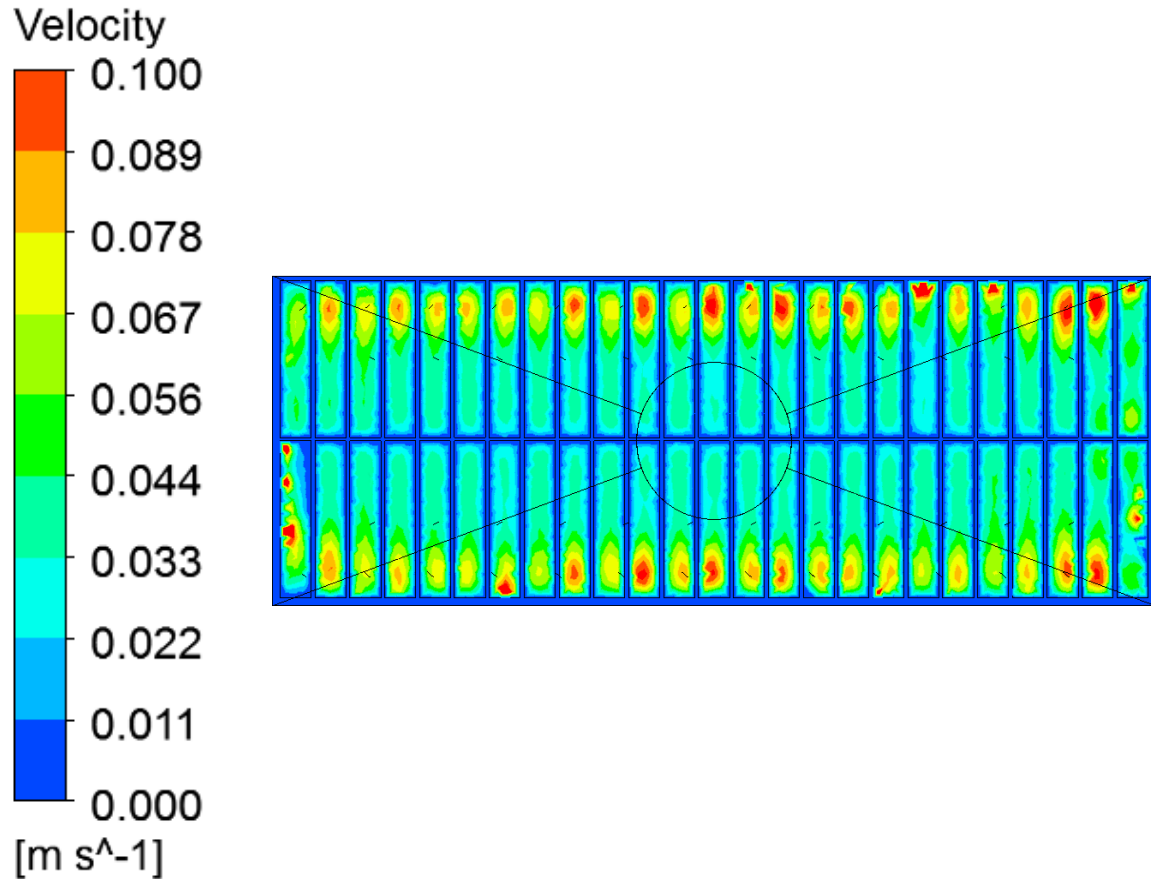


Figure 4-31: Velocity contours at the MCR inlet
(With spheres as flow distributor)

4.5 COMPARISON BETWEEN THE 1-D AND CFD MCR MODELS

The catalyst selected for the CFD model was extrudate particles with bed porosity = 0.375%. The performances of the 1-D MCR model are compared with those obtained using the CFD MCR model in terms of reactants and products molar flow rates, CO conversion and pressure drop as illustrated in Figure 4-32 through Figure 4-34.

Figure 4-32 compares the molar flow rates predicted by both the 1-D and CFD models for H₂, CO and H₂O, as can be seen in this figure the 1-D model systematically predicted steeper flow rate profiles when compared to those of the CFD model, however, both models converge to the same value at the outlet. Similar behaviours can be observed in Figures 4-32 and 4-33 for C1 and the other hydrocarbon products. This difference is primarily due to the numerical methods employed to discretize and solve each of these models, where the 1-D model employs a fourth order Runge Kutta method, while the CFD model uses an upwind quadratic interpolation method.

For CO conversion, both models have the same syngas feed (0.074 mmol-CO/s + 0.149 mmol-H₂/s), but the outlet CO flow rates differ, where the CO conversion is 87.1 % for the 1-D model and 82.4 % for the CFD model.

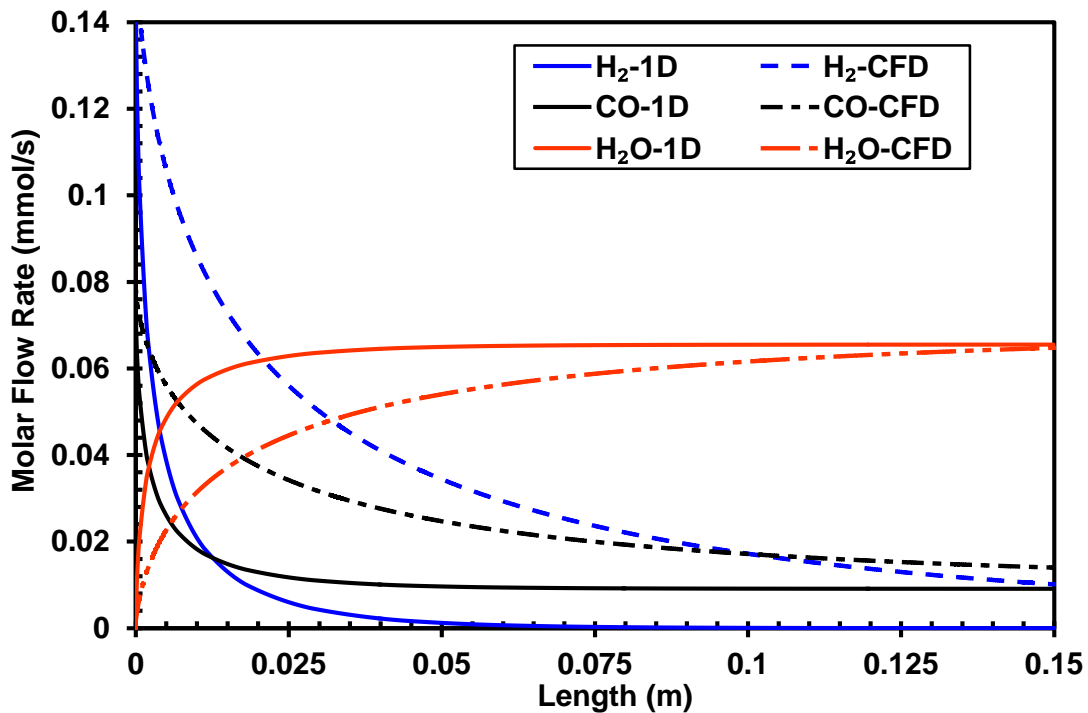


Figure 4-32: Comparison between the flow rates of H₂, CO and H₂O using the 1-D and CFD MCR models

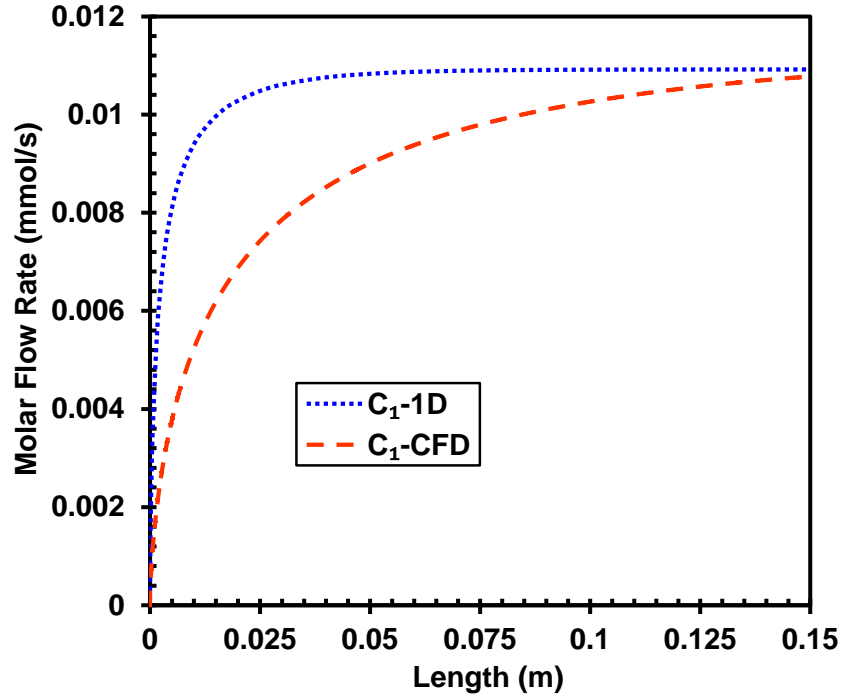


Figure 4-33: Comparison between the C₁ products flow rates using the 1-D and CFD MCR models

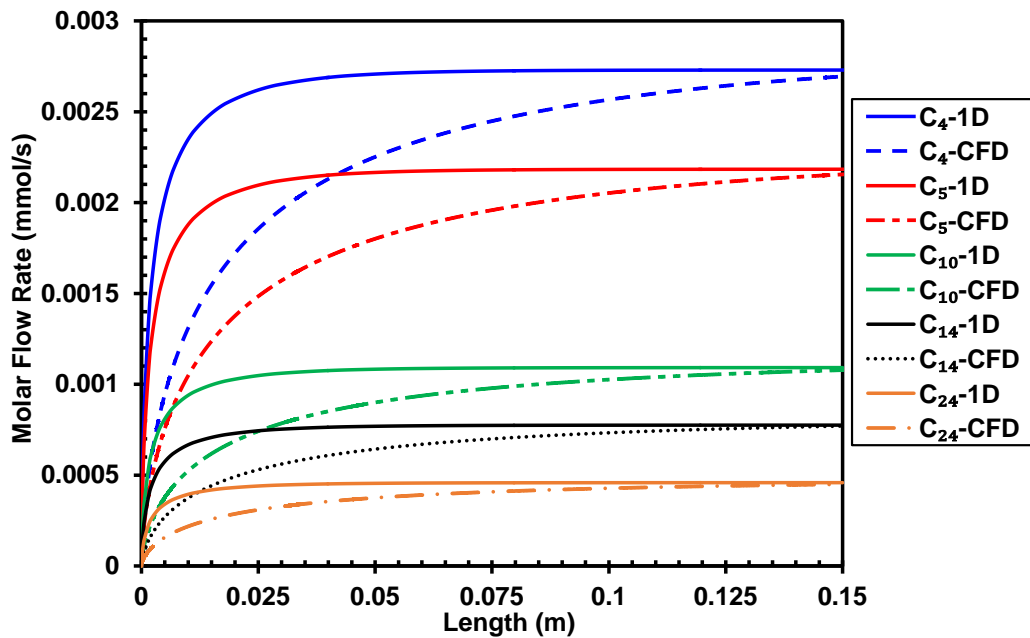


Figure 4-34: Comparison between the hydrocarbon products flow rates between 1-D and CFD MCR models

Figure 4-35 shows the pressure predictions along the channel by both the 1-D and CFD models; and as can be seen the 1-D model systematically predicts higher pressure along the channel than the CFD model. This is primarily due to the difference in representing the pressure drop between the two models. In the 1-D model, the pressure drop is represented using the Ergun-type pressure drop correlation, where the pressure drop is a function of the mean velocity along the channel, whereas, in the CFD model, the pressure drop accounts for the velocity at each point in the reactor when solving the momentum balance equations.

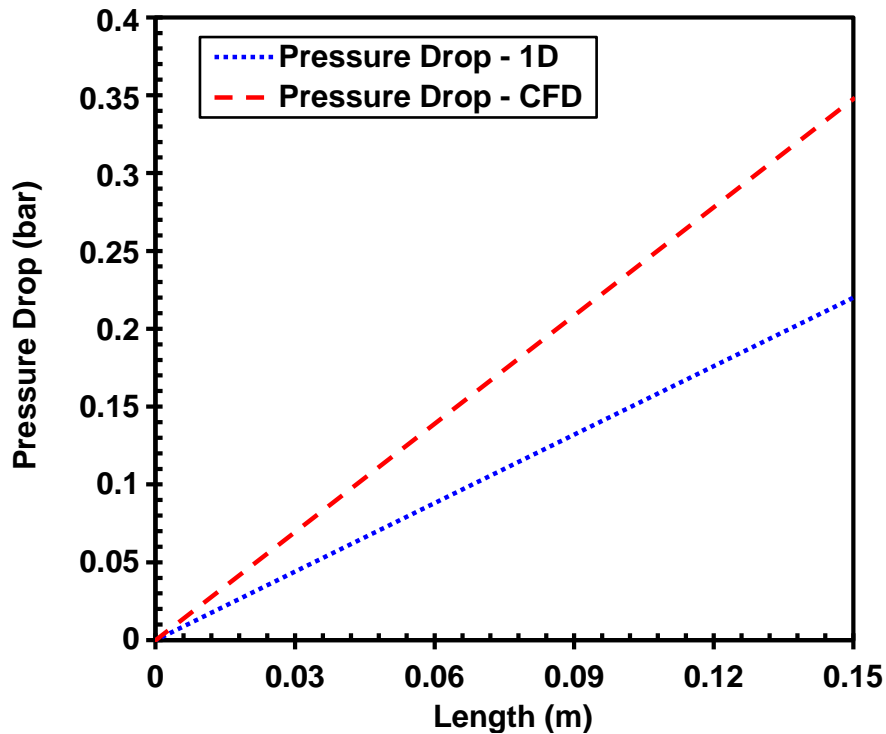


Figure 4-35: Comparison between the pressure drop using the 1-D and CFD MCR models

5.0 CONCLUSIONS

In this study, the performance and the flow distributions of a MCR were investigated using one-dimensional (1-D) as well as Computational Fluid Dynamics (CFD) models. A MCR consisting of 50 channels, each with dimensions of 10 mm × 2 mm × 150 mm packed with 100-micron cobalt catalyst particles, operating under the low temperature F-T synthesis conditions (500 K and 25 bar) to produce mainly alkanes, was used to study the reactor performance. Both models accounted for the F-T reaction kinetics, syngas flow rate, CO and H₂ conversions, C₅₊ selectivity and products yield, pressure drop, heat transfer, and system pressure and temperature. The flow distributions, on the other hand, were investigated using another CFD model with air at 298 K and 1.01325 bar. A 50-channel MCR, each with dimensions of 10 mm × 2 mm × 40 mm and inlet zone of 25 mm length provided with a pipe of 10 mm diameter and 25 mm length, was used in this investigation.

The modeling results led to the following conclusions:

1. The 1-D model systematically predicted steeper hydrocarbon flow rate profiles when compared with those of the CFD model, however, both models converge to the same values at the channel outlet. This difference was primarily due to the numerical methods employed to discretize and solve each of these models. The 1-D model used a fourth order Runge Kutta method, whereas, the CFD model used an upwind quadratic interpolation method.

2. For one channel (10 mm × 2 mm × 150 mm) of the MCR, both the 1-D and CFD models indicated that increasing the H₂/CO ratio of the syngas feed, increased the CO conversion, C₅+ products yield, pressure drop, F-T reaction rate and the heat transfer requirements.
3. Increasing the inlet syngas velocity to the channel decreased the CO conversion and linearly increased the pressure drop. Also, increasing temperature, increased the F-T reaction rate, CO conversion and the C₅+ products yield, and decreased the C₅+ selectivity as well as the pressure drop.
4. Under the operating conditions investigated, the F-T process in the MCR used was found to be kinetically-controlled.
5. The CFD model used to investigate the flow distribution at the MCR inlet showed that in the absence of gas distributor, a strong flow distribution imbalance existed among the channels, with the central ones having significantly higher velocities than those of the lateral ones. Increasing the inlet gas velocity did not have any significant effect on the flow distribution and a similar flow profile, marked with increased velocity at the center and strong recirculation vortices above the channels inlet, was found.
6. The use of a flow distributor, made of two rows of glass spheres with diameters between 0.5 mm and 2 mm placed 5 mm above the microchannels inlet, resulted in homogenous flow profile and better gas distribution among the channels and eliminated the strong gas recirculation.

APPENDIX

OTHER EXPERIMENTAL INVESTIGATIONS USING MCR

Table A-5-1 Other Experimental investigations using MCRs

Reference	Process Studied	Reactor Dimensions
Antes et al., 2003 [51]	Analysis of the products from the nitration reaction of toluene in micro reactors was performed. Micro-reaction process was coupled with high performance liquid chromatography analysis, and online infrared analysis. The selectivity and performance of the micro-reactors was evaluated in terms of the production of mono-nitrotoluenes.	9 Silicon micro channels of 250 μm width.
Gorges et al., 2004 [54]	Kinetics and mass transfer parameters were studied for the 4-chlorophenol undergoing decomposition via a photocatalytic process in a microchannel reactor. The catalyst used was TiO_2 which was deposited in the channels surface by anodic deposition.	The body of the reactor was made out of ceramic. It had 14 process channels that were coated by a Titanium layer and later by the photocatalytic film of TiO_2 .
Tonkovich et al., 2004 [103]	The commercial application of micro reaction technology for hydrogen production is tested. Methane conversion and combustion performance is evaluated, as well as CO selectivity and temperature profiles.	The reactor is divided in three sections for the reactants-product stream and two sections for the fuel stream.

Table A-5-2 Other Experimental investigations using MCRs (continued)

Reference	Process Investigated	Reactor Dimensions
Cao & Gavriilidis, 2005 [50]	The catalytic dehydrogenation of methanol in the presence of high oxygen concentrations was studied in a micro structured reactor. The performance of the reactor was studied under different temperature, reactants concentration and residence times.	Silicon glass micro-reactor with channels of 600 μm wide and a varying reaction zone between 20-200 mm long.
Yeung et al., 2005 [47]	Condensation reaction between benzaldehyde and ethyl cyanoacetate was studied using two micro-reactors configuration, a packed bed membrane reactor and a catalytic membrane reactor.	Varied channels width: 150, 300 and 900 μm . Catalyst coating and membrane thickness: 6-30 μm .
Ge et al., 2005 [41]	Use of microreactor to study the effect of temperature and space velocity on the gas phase partial oxidation of toluene over V/Ti catalyst beds.	Square packed bed channels with cross-sectional area: 1 mm^2 . Catalyst particles with: d_p (μm): 300-600
Görke et al., 2005 [49]	Methanation reaction in the presence of oxygen for selective removal of CO from a gas mixture was evaluated using micro reaction technology. Micro-channels were coated with RU silica based and alumina based catalyst. The performance of the different catalyst was studied for different reaction temperatures, residence time and inlet gas composition.	17 slots of 600 μm width and 150 μm height engraved in 27 stainless steel foils formed the process reaction channels. Each foil was 20 mm wide x 789 mm long. Channel volume was 3222 mm^3 and the coated catalyst surface was 27167 mm^2 .
Walter et al., 2005 [36]	Three different types of reactors were evaluated using the catalytic selective oxidation of isoprene as a model reaction. The performance of a ceramic fixed bed reactor, metal micro-channel reactor and a ceramic micro-channel reactor was compared.	The metal reactor was forms by six aluminum plates of 40 mm \times 40 mm \times 0.5 mm each. The outer dimensions were 70 mm \times 70 mm \times 15 mm. Channels had an inner diameter of 280 μm and were 20 mm long. The ceramic micro-reactor had an outer dimension of 26 mm \times 70 mm \times 8 mm, with 16 micro-channels of square cross section (500 μm \times 500 μm).
Wiles et al., 2005 [48]	Micro-reaction technology was tested for a series of organic reactions with Enolates. The chemical mechanisms investigated were: acylation, aldol alkylation, Michael addition and Knoevenagel condensation. The performance results were compared to conventional Batch process in order to establish potential advantages of micro devices for synthetic organic reactions.	Two types of reactors were use depending on the type of flow. For electroosmotic driven flow the reactors volume was: f 2.5 cm \times 2.5 cm \times 2.0 cm. While for pressure driven flow the reactors volume was: 2.5 cm \times 2.5 cm \times 0.6 cm. For both cases the channels cross sectional length was between 10–500 μm .

Table A-5-3 Other Experimental investigations using MCRs (continued)

Reference	Process Investigated	Reactor Dimensions
Zhao et al., 2005 [32]	Three different processes were investigated using microchannel reactors: Cyclohexene conversion to benzene and cyclohexane; Fischer Tropsch synthesis to produce heavy alkanes and, preferential oxidation of CO in hydrogen fuel cells. The performance of platinum and silica catalyst was evaluated over different reactions conditions comparing two types of catalyst preparations and coatings.	Reactors outer dimension was 3.1 x 1.6 cm. Reaction area dimension was: 1.3 cm x 1.2 cm. Channels dimension: 5-50 μm width and 100 μm length. The channels had a
Flögel et al., 2006 [42]	The synthesis of peptides was evaluated using a silicon microchannel technology. Its performance was compared with typical synthesis processes as solution phase and solid phase couplings.	Total reaction volume was 78.3 μL with a mixing zone of 9.5 μL and a Reaction loop of 68.8 μL .
Fan et al.,2007 [43]	Microscale combustion of methane was evaluated using cylindrical microchannel. The combustion and flame stability was investigated varying the channels width, fuel and oxidants mixture composition and inlet velocity.	The channel was formed by two circular quartz plates 50 mm long. Channel width was varied between 0.5 to 3.0 mm.
Halder et al.,2007 [52]	An experimental study of the nitration of toluene in microchannel structures was carried out. The influence of the reaction temperature, acid concentration, and residence time in the production of nitrotoluenes was evaluated.	Stainless steel reactor with an inner diameter of 775 μm . Channels were packed with catalyst up to a packing length of 6.0 cm. The total length of the reactor was 8.0 cm. Catalyst particle diameter was between 75- 150 μm .
Horii et al.,2007 [53]	A microfluidic device was tested in order to improve the selectivity of a model anodic substitution reaction. The system studied was the anodic oxidation of N-pyrrolidine with allyltrimethylsilane. The reactor was operated in a parallel laminar flow mode and the conversion of the pyrrolidine and the yield of the desired product were calculated.	The body of the reactor was formed by the union of a platinum plate (3 cm wide x 3 cm long) and a glass plate with the same length and a width of 2.6 cm. The open channel was 1 cm wide, 10 μm deep and 6 cm long.
Williams and Mayor, 2010 [45]	Fast pyrolysis of wood was studied employing a new micro-reactor design to improve temperature control and product yield. The design, experimental results and reactors performance were validated against existing pyrolysis data from fluidized bed reactors.	Semi continuous micro-reactor with a processing capacity of 50-70 mg of solid biomass.

BIBLIOGRAPHY

1. Sabatier, P. and Senderens, J. . “Direct Hydrogenation of Oxides of Carbon in Presence of Various Finely Divided Metals” *Compt. rend.* 134, (1902): 689–691.
2. Sehabiague, L. “Modeling, Scaleup and Optimization of Slurry Bubble Column Reactors for Fischer-Tropsch Synthesis” (2012)
3. TU Munchen. “Fischer Tropsch Synthesis” (2013)
4. Steynberg, A., & Dry, M. “Fischer-Tropsch Technology” (2004)
5. Schulz, H. “Short History and Present Trends of Fischer – Tropsch Synthesis” 186, (1999): 3–12.
6. Maitlis, P. M., Klerk, A. de, and Ebrary, I. “Greener Fischer-Tropsch Processes for Fuels and Feedstocks” (2013):
7. Zennaro, R. “Fischer–Tropsch Process Economics” *Greener Fischer-Tropsch Processes for Fuels and Feedstocks* (2013): 149–169.
8. Klerk, A. de. “Fischer-Tropsch Refining” (2012)
9. Dry, M. E. “The Fischer–Tropsch Process: 1950–2000 ” *Catalysis Today* 71 , no. 3 (2002): 227–241. doi:10.1016/S0920-5861(01)00453-9
10. Steynberg, A. P., Espinoza, R. L., Jager, B., and Vosloo, A. C. “High Temperature Fischer–Tropsch Synthesis in Commercial Practice” *Applied Catalysis A, General* 186, no. 1 (1999): 41–54. doi:10.1016/S0926-860X(99)00163-5
11. Chedid, R., Kobrosly, M., and Ghajar, R. “The Potential of Gas-to-Liquid Technology in the Energy Market: The Case of Qatar ” *Energy Policy* 35 , no. 10 (2007): 4799–4811. doi:10.1016/j.enpol.2007.03.017
12. Loosdrecht, J. van de, Botes, F. G., Ciobica, I. M., Ferreira, A., Gibson, P., Moodley, D. J., Saib, A. M., Visagie, J. L., Weststrate, C. J., and Niemantsverdriet (Hans), J. W. “7.20 - Fischer–Tropsch Synthesis: Catalysts and Chemistry A2 - Poepelmeier, Jan Reedijk Kenneth BT - Comprehensive Inorganic Chemistry II (Second Edition)” (2013): 525–557. doi:http://dx.doi.org/10.1016/B978-0-08-097774-4.00729-4
13. Jager, B. “Fischer-Tropsch Reactors” *AICHE Meeting* (2003)

14. Sasol Technology R&D. “Coal to Liquids at Sasol” *Kentucky Energy Security Summit* (2007)
15. Guettel, R., Kunz, U., and Turek, T. “Reactors for Fischer-Tropsch Synthesis” *Chemical Engineering and Technology* 31, no. 5 (2008): 746–754.
16. Bradford, M. C. J., Te, M., and Pollack, A. “Monolith Loop Catalytic Membrane Reactor for Fischer–Tropsch Synthesis” *Applied Catalysis A: General* 283, no. 1–2 (2005): 39–46. doi:http://dx.doi.org/10.1016/j.apcata.2004.12.032
17. Kapteijn, F., Deugd, R. M. de, and Moulijn, J. A. “Fischer–Tropsch Synthesis Using Monolithic Catalysts” *Catalysis Today* 105, no. 3–4 (2005): 350–356. doi:http://dx.doi.org/10.1016/j.cattod.2005.06.063
18. Rohde, M. P., Unruh, D., and Schaub, G. “Membrane Application in Fischer–Tropsch Synthesis reactors—Overview of Concepts” *Catalysis Today* 106, no. 1–4 (2005): 143–148. doi:http://dx.doi.org/10.1016/j.cattod.2005.07.124
19. Oroskar, A. R., Bussche, K. M., and Abdo, S. F. “Microreaction Technology: Proceedings of the Fifth International Conference on Microreaction Technology” (2001): 153–163. doi:10.1007/978-3-642-56763-6_17
20. Tonkovich, A. L., Mazanec, T., Jarosch, K., Fitzgerald, S., Yang, B., Taha, R., Kilanowski, D., Lerou, J., Mcdaniel, J., and Dritz, T. “Improved Fischer-Tropsch Economics Enabled by Microchannel Technology” *White Paper generated by Velocys* (2011): 1–7.
21. Tonkovich, A., Mazanec, T., Jarosch, K., Fitzgerald, S., Yang, B., Taha, R., Kilanowski, D., Lerou, J., McDaniel, J., and Dritz, T. “Improved Fischer-Tropsch Economics Enabled by Microchannel Technology” *Plain City, OH: Velocys Technology* (2008)
22. Jarosch, T., Tonkovich, Y., and Perry, T. “Microchannel Reactors for Intensifying Gas-to-Liquid Technology” *American Chemical Society* (2005)
23. Morsi, B. I. and Basha, O. “Indirect Coal Liquefaction” (2014)
24. Kolb, G. and Hessel, V. “Micro-Structured Reactors for Gas Phase Reactions” *Chemical Engineering Journal* 98, no. 1-2 (2004): 1–38. doi:10.1016/j.cej.2003.10.005
25. Bird, R. B., Stewart, W. E., and Lightfoot, E. N. “Transport Phenomena ” 2nd , (2002)
26. Ehrfeld, W., Hessel, V., and Löwe, H. “Microreactors: New Technology for Modern Chemistry ” 1st , (2000)
27. Tomlinson, H. L., Agee, K., and Roth, E. G. “Movable Gas-to-Liquid System and Process” (2006)
28. Cao, C., Hu, J., Li, S., Wilcox, W., and Wang, Y. “Intensified Fischer–Tropsch Synthesis Process with Microchannel Catalytic Reactors” *Catalysis Today* 140, no. 3-4 (2009): 149–156. doi:10.1016/j.cattod.2008.10.016

29. Deshmukh, S. R., Tonkovich, A. L. Y., Jarosch, K. T., Schrader, L., Fitzgerald, S. P., Kilanowski, D. R., Lerou, J. J., and Mazanec, T. J. “Scale-Up of Microchannel Reactors For Fischer - Tropsch Synthesis” (2010): 10883–10888.
30. Knobloch, C., Güttel, R., and Turek, T. “Holdup and Pressure Drop in Micro Packed-Bed Reactors for Fischer-Tropsch Synthesis” *Chemie Ingenieur Technik* 85, no. 4 (2013): 455–460. doi:10.1002/cite.201200202
31. Myrstad, R., Eri, S., Pfeifer, P., Rytter, E., and Holmen, A. “Fischer–Tropsch Synthesis in a Microstructured Reactor” *Catalysis Today* 147, (2009): S301–S304. doi:10.1016/j.cattod.2009.07.011
32. Zhao, S., Nagineni, V. S., Liang, Y., Hu, J., Aithal, K. R., Seetala, N. V, Fang, J., Siriwardane, U., Besser, R. S., Varahramyan, K., Palmer, J., Nassar, R., and Kuila, D. “At Louisiana Tech University Studies on Conversion of Cyclohexene and Syngas to Alkanes” (2005):
33. Knochen, J., Güttel, R., Knobloch, C., and Turek, T. “Fischer–Tropsch Synthesis in Milli-Structured Fixed-Bed Reactors: Experimental Study and Scale-up Considerations” *Chemical Engineering and Processing: Process Intensification* 49, no. 9 (2010): 958–964. doi:10.1016/j.cep.2010.04.013
34. Tonkovich, A. L., Qiu, D., Schmidt, M. B., Perry, S. T., Fitzgerald, S. P., Hesse, D. J., Gano, N. P., Long, R. Q., Rogers, W. A., Arora, R., and Yuschak, T. D. “Integrated Combustion Reactors and Methods of Conducting Simultaneous Endothermic and Exothermic Reactions” (2004)
35. Karim, A., Bravo, J., Gorm, D., Conant, T., and Datye, A. “Comparison of Wall-Coated and Packed-Bed Reactors for Steam Reforming of Methanol” *Catalysis Today* 110, no. 1-2 (2005): 86–91. doi:10.1016/j.cattod.2005.09.010
36. Walter, S., Malmberg, S., Schmidt, B., and Liauw, M. a. “Comparison of Microchannel and Fixed Bed Reactors for Selective Oxidation Reactions” *Chemical Engineering Research and Design* 83, no. 8 (2005): 1019–1029. doi:10.1205/cherd.04066
37. Aartun, I., Venvik, H. J., Holmen, A., Pfeifer, P., Görke, O., and Schubert, K. “Temperature Profiles and Residence Time Effects during Catalytic Partial Oxidation and Oxidative Steam Reforming of Propane in Metallic Microchannel Reactors” *Catalysis Today* 110, no. 1-2 (2005): 98–107. doi:10.1016/j.cattod.2005.09.001
38. Vesper, G. “Process Intensification through Heat-Integration for High-Temperature Catalysis” (2005): 145–161.
39. Kolb, G., Pennemann, H., and Zapf, R. “Water-Gas Shift Reaction in Micro-channels—Results from Catalyst Screening and Optimisation” *Catalysis Today* 110, no. 1-2 (2005): 121–131. doi:10.1016/j.cattod.2005.09.012

40. Piermartini, P. and Pfeifer, P. “Microreactor Approaches for Liquid Fuel Production from Bioderived Syngas –5 M³ /h Prototype Development for HTHP Water Gas Shift” *Industrial & Engineering Chemistry Research* 54, no. 16 (2015): 4561–4571. doi:10.1021/ie402491c
41. Ge, H., Chen, G., Yuan, Q., and Li, H. “Gas Phase Catalytic Partial Oxidation of Toluene in a Microchannel Reactor” *Catalysis Today* 110, no. 1-2 (2005): 171–178. doi:10.1016/j.cattod.2005.09.006
42. Flögel, O., Codée, J. D. C., Seebach, D., and Seeberger, P. H. “Microreactor Synthesis of Beta-Peptides.” *Angewandte Chemie (International ed. in English)* 45, no. 42 (2006): 7000–3. doi:10.1002/anie.200602167
43. Fan, a, Minaev, S., Kumar, S., Liu, W., and Maruta, K. “Regime Diagrams and Characteristics of Flame Patterns in Radial Microchannels with Temperature Gradients” *Combustion and Flame* 153, no. 3 (2008): 479–489. doi:10.1016/j.combustflame.2007.10.015
44. Men, Y., Kolb, G., Zapf, R., Pennemann, H., and Hessel, V. “Total Combustion of Propane in a Catalytic Microchannel Combustor” *Chemical Engineering Research and Design* 87, no. 1 (2009): 91–96. doi:10.1016/j.cherd.2008.07.010
45. Williams, A. and Mayor, J. R. “A Microreactor System for the Analysis of the Fast Pyrolysis of Biomass” *Journal of Thermal Science and Engineering Applications* 2, no. 3 (2010): 031010. doi:10.1115/1.4003147
46. Losey, M. W., Schmidt, M. A., and Jensen, K. F. “Of Mass Transfer and Reactions” (2001): 2555–2562.
47. Yeung, K. L., Zhang, X., Lau, W. N., and Martin-Aranda, R. “Experiments and Modeling of Membrane Microreactors” *Catalysis Today* 110, no. 1-2 (2005): 26–37. doi:10.1016/j.cattod.2005.09.020
48. Wiles, C., Watts, P., Haswell, S. J., and Pombo-Villar, E. “The Preparation and Reaction of Enolates within Micro Reactors” *Tetrahedron* 61, no. 45 (2005): 10757–10773. doi:http://dx.doi.org/10.1016/j.tet.2005.08.076
49. Görke, O., Pfeifer, P., and Schubert, K. “Highly Selective Methanation by the Use of a Microchannel Reactor” *Catalysis Today* 110, no. 1-2 (2005): 132–139. doi:10.1016/j.cattod.2005.09.009
50. Cao, E. and Gavriilidis, A. “Oxidative Dehydrogenation of Methanol in a Microstructured Reactor” *Catalysis Today* 110, no. 1-2 (2005): 154–163. doi:10.1016/j.cattod.2005.09.005
51. Antes, J., Boskovic, D., Krause, H., Loebbecke, S., Lutz, N., Tuercke, T., and Schweikert, W. “ANALYSIS AND IMPROVEMENT OF STRONG EXOTHERMIC” 81, no. August (2003)

52. Halder, R., Lawal, A., and Damavarapu, R. "Nitration of Toluene in a Microreactor" *Catalysis Today* 125, no. 1-2 (2007): 74–80. doi:10.1016/j.cattod.2007.04.002
53. Horii, D., Toshio, F., and Mahito, A. "A New Approach to Anodic Substitutions Reaction Using Parallel Laminar Flow in a Micro Flow Reactor" *Journal of the American Chemical Society* (2007): 11692–11693.
54. Gorges, R., Meyer, S., and Kreisel, G. "Photocatalysis in Microreactors" *Journal of Photochemistry and Photobiology A: Chemistry* 167, no. 2–3 (2004): 95–99. doi:http://dx.doi.org/10.1016/j.jphotochem.2004.04.004
55. Todić, B., Ordonsky, V. V., Nikačević, N. M., Khodakov, A. Y., and Bukur, D. B. "Opportunities for Intensification of Fischer–Tropsch Synthesis through Reduced Formation of Methane over Cobalt Catalysts in Microreactors" *Catal. Sci. Technol.* 5, no. 3 (2015): 1400–1411. doi:10.1039/C4CY01547A
56. Robota, H. J., Richard, L., Deshmukh, S., and Leviness, S. "Fischer-Tropsch Synthesis in a Microchannel Reactor: The Influence of Co / SiO₂ Catalyst Structure on FTS Performance Presentation Outline" no. January (2014)
57. Velocys. "ENVIA Energy GLT Plant Project Progress" *News release* (2016)
58. CompactGTL. "CompactGTL" (2016)
59. Keyser, M. J., Everson, R. C., and Espinoza, R. L. "Fischer–Tropsch Kinetic Studies with Cobalt–Manganese Oxide Catalysts" *Industrial & Engineering Chemistry Research* 39, no. 1 (2000): 48–54. doi:10.1021/ie990236f, Available at <http://pubs.acs.org/doi/abs/10.1021/ie990236f>
60. Donnelly, T. J., Yates, I. C., and Satterfield, C. N. "Analysis and Prediction of Product Distributions of the Fischer-Tropsch Synthesis" no. 1 (1988): 734–739.
61. Ergun, S. "Fluid Flow through Packed Columns" *Chem. Eng. Prog.* 48, (1952): 89–94.
62. Mehta, D. and Hawley, M. C. "Wall Effect in Packed Columns" *Industrial & Engineering Chemistry Process Design and Development* 8, no. 2 (1969): 280–282. doi:10.1021/i260030a021
63. Tallmadge, J. "Packed Bed Pressure Drop - an Extension to Higher Reynolds Numbers" *AIChE Journal* 16, (1970): 1092–1093.
64. Liu, S., Afacan, A., and Masliyah, J. "Steady Incompressible Laminar Flow in Porous Media" *Chem. Eng. Sci.* 49, (1994): 3565–3586.
65. Eisefeld, B. and Schnitzlein, K. "The Influence of Confining Walls on the Pressure Drop in Packed Beds" 56, (2001): 4321–4329.

66. Harrison, L. D., Brunner, K. M., and Hecker, W. C. "A Combined Packed-Bed Friction Factor Equation : Extension to Higher Reynolds Number with Wall Effects" 59, no. 3 (2013): 703–706. doi:10.1002/aic
67. Soriano, J. "Mass Transfer Characteristics in an Agitated Slurry Reactor Operating under Fischer-Tropsch Conditions" (2005)
68. McCabe, W. L., Smith, J. C., and Harriott, P. "Unit Operations of Chemical Engineering" 5, (1993)
69. Davis, M. E. and Davis, R. J. "Fundamentals of Chemical Reaction Engineering" (2012)
70. Erkey, C., Rodden, J. B., and Akgerman, A. "A Correlation for Predicting Diffusion Coefficients in Alkanes" *The Canadian Journal of Chemical Engineering* 68, no. 4 (1990): 661–665.
71. Philippe, R., Lacroix, M., Dreibine, L., Pham-Huu, C., Edouard, D., Savin, S., Luck, F., and Schweich, D. "Effect of Structure and Thermal Properties of a Fischer–Tropsch Catalyst in a Fixed Bed" *Catalysis Today* 147, (2009): S305–S312. doi:10.1016/j.cattod.2009.07.058
72. Kalteh, M., Abbassi, A., Saffar-Avval, M., and Harting, J. "Eulerian–Eulerian Two-Phase Numerical Simulation of Nanofluid Laminar Forced Convection in a Microchannel" *International Journal of Heat and Fluid Flow* 32, no. 1 (2011): 107–116. doi:http://dx.doi.org/10.1016/j.ijheatfluidflow.2010.08.001
73. Jiang, Y., Khadilkar, M. R., and Dudukovic, M. P. "CFD of Multiphase Flow in Packed-Bed Reactors : I . K -Fluid Modeling Issues" 48, no. 4 (2002)
74. Troshko, A. A. and Zdravistch, F. "CFD Modeling of Slurry Bubble Column Reactors for Fisher–Tropsch Synthesis" *Chemical Engineering Science* 64, no. 5 (2009): 892–903. doi:http://dx.doi.org/10.1016/j.ces.2008.10.022
75. Krishna, R., Baten, J. M. van, Urseanu, M. I., and Ellenberger, J. "Design and Scale up of a Bubble Column Slurry Reactor for Fischer–Tropsch Synthesis" *Chemical Engineering Science* 56, no. 2 (2001): 537–545. doi:http://dx.doi.org/10.1016/S0009-2509(00)00258-X
76. ANSYS Inc. "ANSYS FLUENT Theory Guide" 15.0, (2013)
77. Schiller, L. and Naumann, Z. "A Drag Coefficient Correlation" *Ver. Deutsch. Ing.* (1935): 77–318.
78. Hinds, W. . "Aerosol Technology: Properties, Behavior, and Measurement of Airborne Particles" (1982)
79. Gidaspow, D., Bezburuah, R., and Ding, J. "Hydrodynamics of Circulating Fluidized Beds" *Fluidization VII, Proceedings of the 7th Engineering Foundation Conference on Fluidization* (1992): 75–82.

80. Wen, C. Y. and Yu, Y. H. "Mechanics of Fluidization" *Chem.Eng.Prog.Symp.Series* 62, (1966): 100–111.
81. U.S. Design Institute for Physical Property Data and Engineers, A. I. of C. "DIPPR 801" (2011)
82. Linstrom, P.J and Mallard, W. G. "NIST Chemistry WebBook, NIST Standard Reference Database Number 69" *National Institute of Standards and Technology, Gaithersburg MD, 20899* (2016):
83. Marano, J. J. and Holder, G. D. "Prediction of Bulk Properties of Fischer - Tropsch Derived Liquids" (1997): 2409–2420.
84. Marano, J. J. and Holder, G. D. "General Equation for Correlating the Thermophysical Properties of Behavior Correlations for PVT Properties" (1997): 1895–1907.
85. Arzamendi, G., Diéguez, P. M., Montes, M., Odriozola, J. A., Sousa-Aguiar, E. F., and Gandía, L. M. "Computational Fluid Dynamics Study of Heat Transfer in a Microchannel Reactor for Low-Temperature Fischer-Tropsch Synthesis" *Chemical Engineering Journal* 160, no. 3 (2010): 915–922. doi:10.1016/j.cej.2009.12.028
86. Basha, O. M., Sehabiague, L., Abdel-Wahab, A., and Morsi, B. I. "Fischer-Tropsch Synthesis in Slurry Bubble Column Reactors: Experimental Investigations and Modeling - A Review" *International Journal of Chemical Reactor Engineering* 13, no. 3 (2015): 201–288. doi:10.1515/ijcre-2014-0146
87. Guettel, R. and Turek, T. "Assessment of Micro-Structured Fixed-Bed Reactors for Highly Exothermic Gas-Phase Reactions" *Chemical Engineering Science* 65, no. 5 (2010): 1644–1654. doi:10.1016/j.ces.2009.11.002
88. Kreutzer, M. T., Du, P., Heiszwolf, J. J., Kapteijn, F., and Moulijn, J. A. "Mass Transfer Characteristics of Three-Phase Monolith Reactors" 56, (2001): 6015–6023.
89. Morsi, B. I. and Basha, O. M. "Mass Transfer in Multiphase Systems" (2015): 1–30.
90. Guettel, R. and Turek, T. "Comparison of Different Reactor Types for Low Temperature Fischer-Tropsch Synthesis: A Simulation Study" *Chemical Engineering Science* 64, no. 5 (2009): 955–964. doi:10.1016/j.ces.2008.10.059
91. Lebens, P. J. M., Heiszwolf, J. J., Kapteijn, F., Sie, S. T., and Moulijn, J. A. "Gas-liquid Mass Transfer in an Internally Finned Monolith Operated Countercurrently in the Film Flow Regime" *Chemical Engineering Science* 54, no. 21 (1999): 5119–5125. doi:http://dx.doi.org/10.1016/S0009-2509(99)00265-1
92. Maretto, C. and Krishna, R. "Modelling of a Bubble Column Slurry Reactor for Fischer ± Tropsch Synthesis" 52, (1999): 279–289.
93. Fogler, H. S. "Elements of Chemical Reaction Engineering" 4th, (2006)

94. Bakker, A. "Lecture 5- Solution Methods. Applied Computational Fluid Dynamics" (2002):
95. Ratchananusorn, W. "Flow Phenomena, Heat and Mass Transfer in Microchannel Reactors." (2007)
96. Bhoi, S. "Study of Microchannel Reactor Using Cfd Analysis" (2012)
97. Velocys, I. "Fischer -Tropsch (FT)" (2016)
98. Incropera, F. P. "Fundamentals of Heat and Mass Transfer" 6th, (2007)
99. Wang, Y., Chin, Y. H., Rozmiarek, R. T., Johnson, B. R., Gao, Y., Watson, J., Tonkovich, a. Y. L., and Wiel, D. P. Vander. "Highly Active and Stable Rh/MgOAl₂O₃ Catalysts for Methane Steam Reforming" *Catalysis Today* 98, no. 4 (2004): 575–581. doi:10.1016/j.cattod.2004.09.011
100. Cao, C., Wang, Y., Jones, S. B., Hu, J., Li, X. S., Elliott, D. C., and Stevens, D. J. "Microchannel Catalytic Processes for Converting Biomass-Derived Syngas to Transportation Fuels" (2005): 273–284.
101. Robota, H. J., Richard, L., Deshmukh, S., Leonarduzzi, D., and Roberts, D. "High Activity and Selective Fischer- Tropsch Catalysts for Use in a Microchannel Reactor" no. June (2014)
102. Choudhury, H. A. and Moholkar, V. S. "An Optimization Study of Fischer–Tropsch Synthesis Using Commercial Cobalt Catalyst" *International Journal of Scientific Engineering and Technology* 2, no. 1 (2013): 31–39.
103. Tonkovich, a. Y., Perry, S., Wang, Y., Qiu, D., LaPlante, T., and Rogers, W. a. "Microchannel Process Technology for Compact Methane Steam Reforming" *Chemical Engineering Science* 59, no. 22-23 (2004): 4819–4824. doi:10.1016/j.ces.2004.07.098